

DEVELOPMENT AND CHARACTERIZATION OF WATER-SOLUBLE, PHOTO-  
LUMINESCENT GOLD NANOPARTICLES FOR BIO-IMAGING

by

Chang-won Lee

A dissertation submitted to the faculty of  
The University of Utah  
in partial fulfillment of the requirements for the degree of

Doctor of Philosophy

Department of Bioengineering

The University of Utah

August 2010

Copyright © Chang-won Lee 2010

All Rights Reserved

## STATEMENT OF DISSERTATION APPROVAL

The dissertation of Chang-won Lee  
has been approved by the following supervisory committee members:

Agnes Ostafin, Chair 4/21/2010  
Date Approved

Russell Stewart, Member 4/21/2010  
Date Approved

Ashutosh Tiwari, Member 4/21/2010  
Date Approved

Vladimir Hlady, Member 4/21/2010  
Date Approved

John Veranth, Member 4/21/2010  
Date Approved

and by Richard Rabbitt, Chair of  
the Department of Bioengineering

and by Charles A. Wight, Dean of The Graduate School.

## ABSTRACT

In this dissertation, we explored the synthesis of water-soluble and photoluminescence behavior near infrared emitting (610 nm) gold nanoparticles terminated by mercaptoalkanoic acid and possessing UV range (200~350 nm) excitation. Different effects were monitored as a function of reaction condition including different gold and ligand concentrations, types of ligands, solvents and pH. It is understood that Gold-thiol complexes were formed and developed into nanoparticle-supported complexes. Analyses of the excitation spectra suggests the origin of the photoluminescence to be transitions from the triplet energy state of LMMCT with the electrons transferred from excited orbitals of Au/Au(I) sites of the gold surface. It is also the reason for the enhanced photostability compared with those produced as free molecules via other synthesis methods. The pH dependency of the emission intensity and excitation spectra alteration of the gold nanoparticles was also explored. The emission intensity of the gold nanoparticle showed linear dependency on the pH change in the weak acidic to basic region above the pH 6 with a small peak appearance at pH 4. This trend was accompanied by a distinctive excitation peak wavelength change from 280-290 nm to 250-260 nm at pH 6.. A brush configuration change of the surface ligands was proposed to explain the pH dependency. In the charged and extended form of the carboxylic acid ligands, the accessibility of water to the gold nanoparticles surface is greater than in the uncharged collapsed form. Thus, in the collapsed form, the local hydrophobicity at the gold surface is higher and the

CT excitation spectrum shifts to the blue. Its biocompatibility, as suggested by the cytotoxicity test and reactive oxygen species (ROS) generation test, provides broader opportunities for this product to be utilized in biological systems.

## TABLE OF CONTENTS

ABSTRACT.....	iii
LIST OF TABLES.....	vii
LIST OF FIGURES.....	viii
Chapter	
1. INTRODUCTION.....	1
1.1 Dissertation outline.....	1
1.2 Current status of imaging agents.....	2
1.3 Luminescent gold nanoparticles.....	10
1.4 Outline and flow chart of the dissertation.....	17
1.5 Abstracts of each chapter.....	23
1.6 Conclusions.....	25
2. SYNTHESIS, ANALYSIS AND PROPERTY OF MERCAPTOALKANOIC ACID STABILIZED GOLD NANOPARTICLES.....	27
2.1 Abstract.....	27
2.2 Introduction.....	28
2.3 Materials and methods.....	30
2.4 Result and discussion.....	39
2.5 Conclusions.....	72
3. PH DEPENDENT EMISSION PROPERTIES OF MERCAPTOOCTANOIC ACID TERMINATED GOLD NANOPARTICLES .....	75
3.1 Abstract.....	75
3.2 Introduction.....	76
3.3 Materials and methods .....	78
3.4 Results.....	81
3.5 Discussion.....	90
3.6 Conclusion.....	98

4. EFFECT OF NANOPARTICLES ON THE MEASUREMENT OF REACTIVE OXYGEN SPECIES BY THE AMPLEX RED ASSAY.....	100
4.1 Abstract.....	100
4.2 Introduction.....	101
4.3 Materials and methods.....	104
4.4 Results and discussion.....	106
4.5 Conclusion.....	122
5. CONCLUSION.....	125
LITERATURE CITED.....	130

## LIST OF TABLES

<u>Table</u>	<u>Page</u>
1.1. Comparison of bio-imaging techniques.....	2
1.2. Fluorescent amino acids used in bioluminescence application.....	4
1.3. Types of luminescent gold species reported in the literature.....	12
1.4. Summary of pros and cons of the two types of luminescent gold nanoparticles	17
2.1. Calculated and experimental HOMO-LUMO gap energies.....	42
2.2. List of energies and wavelengths of persistent or strong lines in neutral Au and single ionized Au.....	46
2.3. Effect of chain length on photoluminescence and particle size.....	51
2.4. Hydrophobicity comparison of the MHA to MPA hybrid gold nanoparticles...	58
3.1. Surface coverage by mercaptooctanoic acid.....	90
3.2. Excitation and emission maximum, and energy shift for gold-MOA materials as function of solvent polarity.....	97
4.1. Physical properties of nanoparticles used in this study.....	107
4.2. $k_1$ and $k_3$ values for each nanoparticle.....	115
4.3. Rate constants for iron oxide catalyzed hydrogen peroxide decomposition....	115

## LIST OF FIGURES

<u>Figure</u>	<u>Page</u>
1.1. Schematic diagram of fluorescent process.....	6
1.2. Schematic illustration of the light emission from quantum dot.....	8
1.3. Systematic flow chart of the dissertation.....	18
2.1. Characterizations of gold nanoparticle.....	40
2.2. ATR-FT-IR spectra.....	42
2.3 Gaussian3 simulated orbital isosurfaces of Mercaptooctanoic acid.....	44
2.4 Gold nanoparticle excitation spectrum and proposed energy diagram.....	47
2.5. Photostability of luminescent gold materials.....	48
2.6. Photobleaching property of gold nanoparticle solution.....	49
2.7. TEM pictures of different ligand stabilized gold nanoparticles.....	50
2.8. Excitation and emission spectra of GNP with different ligand.....	52
2.9. Cartoon illustrating hypothetical cutaway configuration of gold-ligand complexes and gold atoms at the surface of gold nanoparticles.....	54
2.10. Scheme describing one of the possible effects of the longer chain on the size of the gold nanoparticles.....	55
2.11. NaCl induced aggregation of the gold nanoparticles.....	57
2.12. NaCl induced aggregation of hybrid gold nanoparticles.....	58
2.13. Spectra and analysis on timed gold nanoparticle synthesis.....	60
2.14. TEM pictures of the gold nanoparticles synthesized in different solvent ratio of EtOH to water.....	63

...

2.15. TEM pictures of the gold nanoparticles synthesized with different thiol to gold ratio.....	64
2.16. Particle size analysis.....	66
2.17. The size of the gold nanoparticles and its relation with the emission intensity.....	67
2.18. Excitation spectrum energy maximum and its relation to the relative quantum yield.....	67
2.19. Temperature dependence of the fluorescence emission intensity.....	69
2.20. Beas-2B cell viability versus dose of gold nanoparticles.....	72
2.21. The fluorescence microscopic image.....	74
3.1. Transmission electron microscope image of fluorescent gold nanoparticles.....	81
3.2. Red-emitting gold nanoparticle solutions on the UV transilluminator.....	82
3.3. Gold nanoparticle optical spectra at different pH.....	83
3.4. Reversibility of fluorescence intensity as a function of pH.....	84
3.5. Normalized emission intensity at different pH.....	85
3.6. DLS size and zeta potential.....	86
3.7. Controlled aggregation of the gold nanoparticle and its fluorescence.....	87
3.8. Excitation spectra shift in the presence of salt.....	88
3.9. Brush configuration.....	91
3.10. Molecular orbital.....	92
3.11. Proposed energy transfer diagram.....	93
3.12. The Lippert-Mataga plot.....	96
4.1. Chemistry scheme of Amplex Red conversion to resorufin.....	101
4.2. Resorufin fluorescence emission intensity.....	108
4.3. Detection of H <sub>2</sub> O <sub>2</sub> .....	109
4.4. Ratio of resorufin fluorescence signal intensity measured in the presence of nanoparticles divided by resorufin signal intensity detected in buffer.....	110

4.5. The measurement of the resorufin formation after the mixing with H <sub>2</sub> O <sub>2</sub> .....	114
4.6. Computer simulation on resorufin concentration profile with assumptions....	118
4.7. Computer simulation of the concentration profile is shown over time.....	119
4.8. The effect of gold nanoparticle presence in Amplex Red assay.....	123

## CHAPTER 1

### INTRODUCTION

#### 1.1. Dissertation outline

This dissertation involves 1) the evaluation of the formation of emissive gold-ligand complexes, 2) their relation to the formation of water-soluble, photoluminescent gold nanoparticles, 3) an analysis of the emission process and its dependence on pH, 4) preliminary cell viability using immortalized pulmonary cell line, BEAS-2B and 5) the role of this material in the formation of reactive oxygen species (ROS) generation using Amplex Red with comparison to the effect on this measurement by the presence of the oxide nanoparticles.

The described evaluation of emissive gold-ligand complexes is a required foundation to enable the development of the diagnostic agents based on gold nanoparticles. These agents combine capabilities for imaging with targeted delivery to specific sites, for example, to evaluate the consequences and causes of diseases such as cancer, to study the mechanisms of new drugs, or to follow the events of DNA and protein synthesis. However, the development of multifunctional materials which can fulfill the need remains challenging because of the difficulty in developing nanomaterials which possess several properties simultaneously such as water-solubility, bio-compatibility, photostability, durability, quantum efficiency and processability.

## 1.2. Current status of imaging agents

### 1.2.1. Comparison of bio-imaging techniques

Photo-luminescence is a phenomenon in which the molecular absorption of a photon triggers the emission of another photon with a longer wavelength[1]. It has been widely utilized for imaging purposes and has been utilized to pin-point specific areas of the tissue or tumor by a two-photon technique [2]. Other nonluminescent bio-imaging agents have been used to enhance ultrasound [3], X-ray [4], Magnetic Resonance Imaging (MRI) [3] or Computed Tomography (CT) scanning [5] techniques (Table 1.1).

Ultrasound imaging involves sound pressure with very high frequency (20 kHz). The reflection signals reveal images of internal organs [3]. This technique shows images of tissues in real time and one of the most widely used diagnostic tools due to its inexpensiveness and portability especially when compared with MRI or CT. The ultrasound reflection signal is created by the echoes from tissues with different

**Table 1.1.** Comparison of bio-imaging techniques

<b>Bio-imaging techniques</b>	<b>Resolution</b>	<b>Contrast</b>	<b>Process speed</b>	<b>Radiation exposure</b>
<b>Ultrasound[3]</b>	< 0.1 mm	Echo by density change	Instant	No
<b>X-ray[4]</b>	< 0.1 mm	X-ray transmission by density	Instant	Yes
<b>MRI[3]</b>	< 1 mm	Hydrogen density	Slow	No
<b>CT scan[5]</b>	< 1 mm	Density difference	Slow	Yes
<b>Fluorescence bio-imaging[6]</b>	<1 $\mu$ m	Emission from fluorophore	Instant	No

density with a relatively low resolution of 0.1 mm range. Ultrasound also has a potential of enhancing inflammatory response and heating the tissues. The sonic pressure may cause microscopic bubbles in living tissues that lead to distortion of the cell membrane and change in ion fluxes and intracellular activity [7].

X-ray uses electromagnetic radiation with very short range of wavelength in the range of 10 to 0.01 nm, which is equivalent to 30 peta Hz (120 eV) to 30 exa Hz (120 keV). X-rays can penetrate solid objects and the resulting images are generated by the density of the target objects with the resolution of 0.1 mm range [4]. However the resolution is generally low and radiation exposure is a potential problem for this technique. The sum of all medical X-rays accounts for 10 % of total American radiation exposure [8].

MRI (Magnetic Resonance Imaging) is a medical imaging technique to visualize the internal structure and function of the body [3]. It uses a magnetic field to align the protons of water molecules with the direction of the magnetic field. Then the radio frequency (RF) fields are applied to alter the alignment of the magnetization of the protons. These alignment changes produce signals in different planes that are used to construct a body image after it is detected by the scanner. Using this technique, diseased tissues such as tumors can be detected due to the different rates to reach equilibrium of the protons. However, these are not sensitive enough to determine smaller-sized malignant tumors especially when they are in their early stage and the resolution is over 1 mm range.

CT (Computed Tomography) is also a medical imaging method using tomography generated by computer processing [5]. Three-dimensional images of the objects can be created by this technique by accumulating a large series of two-dimensional X-ray images taken with a specific axis of rotation. Even though it has

enhanced applicability compared to the two-dimensional X-ray images, it still lacks the sensitivity to pin-point smaller, early stage targets due to the similar contrast between the normal and malignant tissues. The resolution of the image is limited in 0.1 mm range like X-ray scanning technique.

Fluorescent bio-imaging is one of the most promising technologies due to its superior sensitivity, brightness, higher resolution, chemical identification, faster detection and the possibility of color-coded multiplexing [6]. The resolution of fluorescence bio-imaging can be as small as the size of the fluorophore (either an organic molecule or nanoparticle). Since it emits the light of a color different from what is absorbed it can be differentiated from the background easily [9]. Usually synthetic fluorophores absorbing and emitting light in the visible portion of the electromagnetic spectrum are used, but emission can also be detected from the natural fluorescence of amino acids such as tryptophan (W) and tyrosine (Y) [1] listed in Table 1.2. These autofluorescent amino acids have excitation and emission spectra in the UV range (250 ~ 350 nm). High energy UV light can cause DNA and tissue damage during the scanning and its penetration depth is short [10].

Chemiluminescence, emission as a result of a chemical reaction [11], can also be used for imaging. For example, luminol ( $C_8H_7N_3O_2$ ) interacts with hydrogen peroxide to produce excited state 3-aminophthalate. This intermediate molecule

**Table 1.2.** Fluorescent amino acids used in bioluminescence application

<b>Amino Acids</b>	<b>Excitation (nm)</b>	<b>Emission (nm)</b>	<b>Lifetime (ns)</b>
<b>Tryptophan</b>	280	348	2.6
<b>Tyrosine</b>	274	303	3.6
<b>Phenylalanine</b>	257	282	6.4

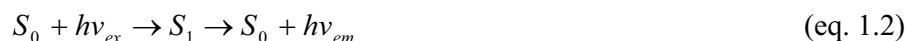
eventually loses its energy to reach ground state with the release of photon as shown in the following reaction equation 1.1.



Fluorescence bio-imaging using fluorescent molecules or quantum dots to the target tissue will be dealt in more detail in sections of 1.2.2 and 1.2.3.

### 1.2.2. Fluorescent molecules

In fluorescence, electrons from the ground state absorb energy from the excitation light and transfer to excited state (Figure 1.1). Then after a short period of time, usually ranging from  $10^{-9}$  to  $10^{-8}$  sec, these electrons move back to the ground state after releasing additional energy they acquired during the excitation state as light. This process can be written into a simple chemistry formula (eq. 1.2) shown below in which the first two terms indicate the excitation process and the last two terms indicate the emission process.



Here,  $S_0$  is a ground state of the fluorescence material,  $S_1$  is an excited state,  $h$  is Planck's constant and  $\nu$  is the frequency of light at excitation and emission as denoted in the subscript.

The energy difference between the absorption and emission light is called Stokes shift named after Irish physicist George G. Stokes [1]. The lost energies not contained in the emission phenomenon are usually released to the environment in the forms of molecular vibration, heat or rotations. In rare cases, the emitted photon has smaller wavelength, i.e., higher energy, than the excitation light and it is called anti-

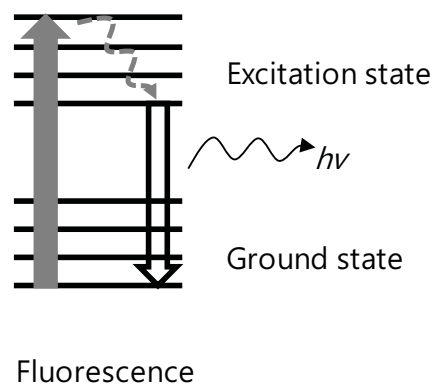


**Figure 1.1.** Schematic diagram of fluorescent process (Jablonski diagram [1], solid grey arrow: excitation, dotted grey arrow: nonradiation energy transfer, hollow arrow: radiation energy transfer)

Stokes shift. In this case, usually the extra energy comes from the involvement of phonons in the emission process [1; 12].

To quantitatively describe the efficiency of the fluorescence process, the idea of the “quantum yield” has been developed [1]. A quantum yield can be simply defined as the ratio of the number of photons emitted to the number of photons absorbed (eq. 1.3).

$$\Phi = \frac{\# \text{ photon}_{em}}{\# \text{ photon}_{abs}} \quad (\text{eq. 1.3})$$

Hence, the maximum possible fluorescence quantum yield is 1.0. Usually, a fluorescence material which has the quantum yield of 0.1 is still considered to be an “efficient” fluorescence material. Usually, it is more convenient to measure a given compound’s quantum yield by its “relative quantum yield”. In this case, a well-known standard fluorescence material, such as fluorescein, is used to calculate the quantum yield of the fluorescence material of interest (eq. 1.4) [1].

$$\Phi_{sample} = \Phi_{ref} \left( \frac{\nabla_{sample}}{\nabla_{ref}} \right) \left( \frac{n_{sample}^2}{n_{ref}^2} \right) \quad (\text{eq. 1.4})$$

Here  $\nabla$  is the slope of the integrated fluorescence intensity with respect to the absorbance at the excitation wavelength and  $n$  is the refractive index of the solution in which the fluorescent material is dissolved. The subscript *ref* represents reference fluorescence material whose optical properties are already known and *sample* represents the sample fluorescence material of interest.

Fluorophores such as fluorecein and bioluminescence proteins such as luciferase are widely used fluorescent molecules in bio-imaging research [6]. A drawback is the low photobleaching threshold of the fluorophore after a short time of exposure to excitation light and poor photochemical stability[1]. For this reason more resilient quantum dots have been used. Most organic dyes have 100 to 1000 times lower photobleaching thresholds than quantum dot [13; 14].

### 1.2.3. Quantum dots

Quantum dot emission arises from a phenomenon called quantum confinement [15]. In this mechanism there is physical confinement of excitons (hole/electron bound pair in the material). When the size of nanoparticle is smaller than the exciton radius (distance between electron-hole pair), the exciton energies start to split into discrete levels instead of remaining in a continuum (Figure 1.2). Transitions of electrons between these levels may correspond to visible wavelength energies. Relaxation from the higher levels back to the thermally equilibrated levels is detected as emission. Such nanoparticles absorb more energy than their bulk counterpart resulting in emitting stronger energy (shorter wavelength) [16]. This is why quantum dots can generate distinct emitting light which is one of the important

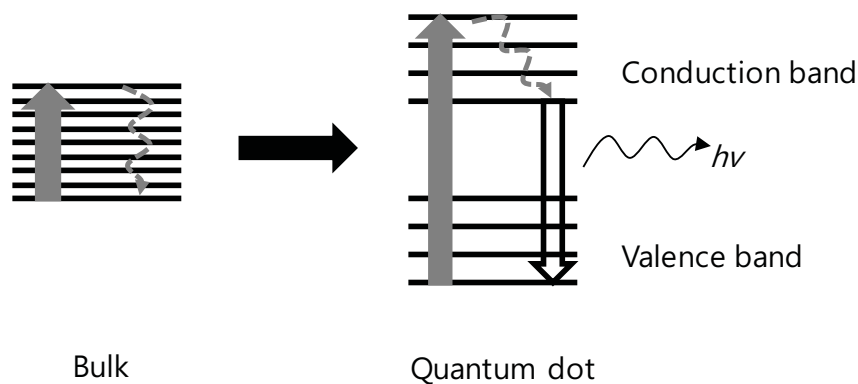


**Figure 1.2.** Schematic illustration of the light emission from quantum dot (solid grey arrow: excitation, dotted grey arrow: nonradiation energy transfer, hollow arrow: radiation energy transfer); Discrete energy levels forms with the particle size smaller than Bohr Radius.

factors to be a bio-imaging agent with greater resolution and sensitivity. Typical quantum dots include cadmium and zinc-based quantum dots have been developed as imaging agents [15; 17; 18; 19].

A critical disadvantage in the use of cadmium quantum dot system, namely cytotoxicity caused by the release of highly toxic  $\text{Cd}^{2+}$  ions from the cluster [20]. Free  $\text{Cd}^{2+}$  concentration in a 0.25 mg/mL solution of cadmium quantum dots can be as much as  $1 \times 10^3 \mu\text{M}$  and this value is known for significant cell death [21]. Physiologically, cadmium is known to cause diseases such as “Itai-Itai” disease [22] and malfunctions of the zinc-coenzyme proteins. Zinc and cadmium are in same group in periodic table with same charge number (+2) and similar ion size (Zn:  $R=1.42 \text{ \AA}$  and Cd:  $R: 1.61 \text{ \AA}$ ). Thus, cadmium can replace the position of zinc, but does not function biologically as zinc and it is known a carcinogen causing many types of cancer [23]. The safety of zinc-based quantum dots has not been thoroughly

demonstrated. Zinc is a bioactive element that affects numerous enzyme processes [24].

To overcome the cytotoxicity problem, the surfaces of the cadmium nanoparticles are often covered with biocompatible molecules like PEG [17]. Surface-covered PEG limits the exposure of the cadmium surface to water to minimize the leaching of cadmium ions to the surrounding area of the tissues or cells. However there is still a danger of cadmium release if the surface coating material is damaged by biochemical or mechanical stress.

#### 1.2.4. Possible alternative – luminescent gold nanoparticles

Based on the previous discussion it is clear that a different kind of fluorescence imaging agent is desired. As an ultimate solution, we need a system that possesses suitable photo-luminescence properties with low cytotoxicity and improved photo-stability including photobleaching and photo- and biochemical inertness. In addition, it should have predictable pH-dependent performance.

Water-soluble, fluorescent gold nanoparticles could be an answer. As Connor et al. showed using an MTT assay[25], gold nanoparticles are widely known and proven not to cause any biocompatibility issues such as acute inflammatory reactions even though it is uptaken by cells [26]. However there remains some controversy. For example, Alkylany et al.[27] showed a cytotoxic effect of CTAB (cetyltrimethylammonium bromide) capped gold nanorods on human colon carcinoma cells and Calamai et al.[28] also reported cytotoxicity of Au(III)-Cl complexes on human ovarian carcinoma cells. Because each of these involves different syntheses and reagents such as using CTAB or Cl ligands, we need to establish our own cytotoxicity results for our gold nanoparticle products.

Gold nanoparticles larger than 2-4 nm in diameter are poorly fluorescent and there have been considerable difficulties in preparing well-defined emissive materials. This area is reviewed in next section.

### 1.3. Luminescent gold nanoparticles

#### 1.3.1. Luminescent gold nanoparticles for bio-imaging techniques

The optical properties of gold nanoparticles have been studied for many years [29; 30; 31; 32; 33] but making luminescent gold nanoparticles is challenging. Because gold is not a semi-conducting atom, the gold nanoparticles greater than 3 nm in diameter are not strongly fluorescent. Thus, their past use has been more focused on absorption and reflection properties [34; 35]. For example, gold nanoparticles have been used as a contrast agent after being conjugated with targeting molecules such as antibodies or folate for MRI and CT scanning because of its density difference to the background [36; 37]. For spherical gold nanoparticles in the size range of 10 to 50 nm, visible light induces a resonant, coherent oscillation of the electrons near the surface of the nanoparticle [38]. This oscillation is called surface plasmon resonance (SPR). Recently, it was recognized that the SPR effect enhances light scattering and absorption giving the nanoparticles more intense color [39]. However, these techniques have less sensitivity compared to the fluorescent imaging techniques due excessive scattering of incident light which lowers the signal to noise ratio.

A great deal of effort has been expended to understand how the optical properties of these materials are affected by pH [40; 41; 42], dielectric function [43; 44] and refractive index [45]. Tracking pH change or pin-pointing the area with different pH is an important aspect of a bio-imaging agent since the target could have different pH than the surrounding area. One example is cancer cells with the pH

around 5 [46]. The SPR frequency of gold nanoparticles depends on the nearby dielectric medium and the size and composition of nanoparticles [44]. In the case of 40 nm gold nanoparticles, the resonance is sensitive to the environment 10 ~ 20 nm above the particle surface. So a slight change of refractive index in this nano-environment would cause a significant change in the resonance spectrum [45].

### 1.3.2. Gold-ligand complexes and quantum confined gold nanoparticles

Past attempts to make fluorescent gold nanoparticles yielded the following two types of nanoparticles: water soluble gold complexes [47; 48; 49; 50; 51; 52; 53; 54; 55; 56] and few-atom quantum-confined clusters. [32; 57; 58; 59; 60; 61; 62; 63; 64] that are smaller than Au<sub>39</sub>, grown and regulated by the assistance of dendrimers, proteins or argon matrices (Table 1.3). The details of each will be discussed in the following sections.

1.3.2.1. Gold-ligand complexes. Gold-ligand complexes have visible emissions and can be generated by binding nonfluorescent ligand molecules including phosphine and/or thiol based molecules to form luminescent gold (I) complexes [47; 48; 49; 50; 51; 52; 53; 54; 55; 65; 66]. The gold atoms in these complexes are loosely assembled gold clusters with adjacent Au···Au distances near or less than 3.6 Å [49] and bonding forces about 29–46 kJ mol<sup>-1</sup> [67].

Gold complexes have a broad absorption spectra and sometimes plasmon resonance features in addition to their ligand complex emissions suggesting heterogeneity of the system (Table 1.3). Electrophoresis analyses confirm a mixture of materials is present.

**Table 1.3.** Types of luminescent gold species reported in the literature.

Author	Ligand	Excitation((eV)	Emission (eV)	QY	Solvent	Reductant	Lifetime ( $\mu$ s)
Susha[53]	dodecylthiolate	2.58-3.1	1.94-1.99	0.002-0.08	EtOH, Polymer	none	1.18-1.85
Vogler[51; 52]	SMe <sub>2</sub> , SH	3.54-4.13	1.86-1.92	0.01-0.03	EtOH, ACN		--
White-Morris[49]	cyclohexyl isonitrile	4.59	1.98-2.03	--	DMSO		18-47
Cha[48]	Alkanethiolates	4	2.03	--	THF	none	--
Yam[47; 50]	PPh <sub>3</sub>	3.1-4.62	2.38-2.43	--	CH <sub>2</sub> Cl <sub>2</sub>	none	0.1-3.77
Bachman[66]	phenylthiolate	3.44	1.88	--	--		1.1
Jones[54; 55]	PPh <sub>3</sub>	3.14-3.26	2.41-2.56	--	CH <sub>2</sub> Cl <sub>2</sub>		40-50
Zhang[68]	mercaptoheptoxystilbene	4.4	3.2	-	CH <sub>2</sub> Cl <sub>2</sub>	none	-
Negishi[64; 69; 70]	Glutathione/dimercaptosuccinic acid	2-4	1.5-1.7	10 <sup>-3</sup> -10 <sup>-5</sup>	Methanol, water	NaBH <sub>4</sub> / <i>meso</i> -2,3-dimercaptosuccinic acid	--
Tzeng[56]	PPh <sub>3</sub> / quinoline-8-thiolate	3.3	1.91	-	Methanol, CH <sub>2</sub> Cl <sub>2</sub>	Sulfate	-
This work	Mercaptoalkanoic acid	4.3	2.03-2.48	.03	H <sub>2</sub> O	NaBH <sub>4</sub>	1.5
Bao[61]	dendrimer*	3.06-3.69	2.7-2.73	0.38	H <sub>2</sub> O		0.002-0.006
Huang[62]	mercaptoalcohol	3.17-3.38	2.38	10 <sup>-6</sup> -0.03	H <sub>2</sub> O	Tetrakis(hydroxymethyl)phosphonium chloride	0.02-0.045
Longo[71]	dodecanethiol in polystyrene	3.49-5.17	1.98-2.48	--	Ethanol, ACN		--
Zheng[32; 60; 72]	dendrimer	Depends on size	Depends on size	0.1-0.7	H <sub>2</sub> O		0.0035-0.0075

White-Morris [49] produced ligand complexes with cyclohexyl acetonitrile that were characterized with a sharp excitation peak maximum at an unusual energy of 4.6 eV (270 nm) and a profile that showed a steep decrease of intensity at the red edge of the excitation peak at 4.3 eV (290 nm). Susha and coworkers [53] produced Au(I)-thiolate or few-atom thiolated  $Au_x(SR)_y$  clusters in which the emission maximum between 620-640 nm was also accompanied by a narrow excitation spectrum with maxima at  $\sim 4.4$  eV (280 nm) with relatively high quantum yield (0.002~0.08). Their 1.8 nm particles were produced in a polystyrene polymer matrix via the thermal decomposition of Au(I) dodecylthiolate ( $AuSC_{12}H_{25}$ ) which has an absorbance at 3.2 eV (390 nm). Unfortunately their materials were short-lived, and continued processing led to a loss of emission and the growth of very large nanoparticles.

The origin of the gold-ligand complex luminescence has been attributed to ligand-to-metal charge transfer (LMCT) complexes or ligand-to-metal-metal charge transfer (LMMCT,  $S \rightarrow Au$ ) [56]. Yam et al. indicated that the lifetime of emission of gold-ligand complexes at 2.4 eV in dimethylchloride with the  $PPh_3$  ligands is in the microsecond range leading to the suggestion that the excitation may involve a triplet pathway [47; 50]. Gold-ligand complexes with very similar synthesis conditions and properties have also been reported by Jones et al.[54; 55].

In addition to solution-based syntheses, Cha et al., reported a new electron beam irradiation method to synthesize Au(I) complexes [48] and claimed that using alkanethiols with various carbon lengths, luminescent, functionalized Au(I) complexes were synthesized but were insufficiently soluble.

Most of the fluorescing gold-ligand complexes mentioned above are prepared and are stable in nonaqueous solutions, limiting their use in biology. Not all

of them have been thoroughly evaluated, but Vogler et al. showed that ligand complexes are very sensitive to light exposure using a Xe/Hg 1kW lamp which causes photodecomposition of the complexes and aggregation into large gold nanoparticles within a few minutes [51; 52]. For this measurement the absorbance or optical density value at 598 nm was monitored as an indicator of particle growth and was shown to increase from 0 to 0.45 in 20 min.

To summarize, several technical problems have slowed the development of luminescent gold–ligand complexes into usable products, particularly in medical areas. While their emissions are much stronger than the earliest reported photoluminescence from larger gold nanoparticles, they are still relatively weak compared to the better known quantum dot materials [52; 53; 64] (Table 1.3). The emissions of ligand complexes are highly susceptible to temperature- and photodecomposition [51]. Finally, Au(I)-ligand complexes have also historically been produced in organic solvent, and phase transfer to aqueous solution can result in interconversion between metal-ligand stoichiometry culminating in the growth of large gold particles [47; 48; 49].

1.3.2.2. Quantum-confined gold nanoparticles. Since gold is not a semi-conducting species, it is relatively harder to develop quantum-confined clusters comparable to those semi-conductors such as cadmium. The Bohr exciton radius of gold is very small so that the cluster size needed to maintain quantum confinement should be 0.5 nm diameter or less, which is roughly a size of Au<sub>39</sub> cluster[32; 60]. In contrast for Cd-based materials particles between 2 and 10 nm are needed [15]. In general, small clusters are inherently unstable and the equilibrium pushes toward the addition of other gold atoms to produce larger particles.

To develop successful small clusters with a size smaller than the Bohr radius stabilization of the cluster to prevent further growth of the particle size is required. As one of the examples of quantum confined gold clusters, Zheng et al. [32; 60; 72] have prepared gold clusters consisting of only a few-atoms clusters grown in the hydrophobic interiors of water soluble poly(amidoamine) (PAMAM) dendrimers. Smaller clusters such as Au<sub>5</sub> generated UV emission and larger ones such as Au<sub>31</sub> NIR emission. However, these are normalized intensities without a clear purification protocol for the gold nanoparticles. Later, Bao et al. used the same type of PANAM dendrimers but modified the synthesis protocol [61]. They adopted milder synthesis conditions in physiological temperature of 37 °C and pH range with higher yield of production compared to Zheng's protocol. Instead of dendrimers, amorphous polymer matrices such as polystyrene [71] have also been used to stabilize the growth of the gold clusters prepared by thermal decomposition.

Unlike others who prepared quantum confined gold clusters with the assistance of stabilizing matrices, Negishi et al.[64; 69; 70] showed that quantum confined gold nanoclusters could be stabilized by covalently bound glutathione. Their gold clusters are sized from Au<sub>10</sub> to Au<sub>39</sub> clusters and they have relatively weaker quantum yields (ranging 10<sup>-3</sup> to 10<sup>-5</sup>) compared to dendrimer stabilized gold nanoclusters. They also showed the size distribution by gel-electrophoresis with the size in 10 ~ 30 kDa size range.

1.3.2.3. Summary of difference between luminescent gold-ligand complexes and luminescent quantum confine gold nanoparticles. In general, the distinguishing observable difference between luminescent gold-ligand complexes and quantum confined gold nanoclusters is the relative positions of their absorption versus emissionspectra and the time dependent dynamics of the emitting species. For

instance, for quantum confined clusters, the Stokes shift between absorption and emission is relatively small (~50 nm) and shifts smoothly to the near infrared with increasing cluster size [32; 60]. The emission lifetimes for quantum-confined materials are in the picoseconds range. In contrast for gold-ligand complexes, the Stokes shift is much larger (~150-200 nm), and the emission exhibits microsecond kinetics [47; 48; 49; 50]. The metallic characteristics of the gold limits the size of the quantum-confined gold nanoclusters only up to Au<sub>39</sub> (~0.5 nm) for observing fluorescent emissions. On the other hand gold-ligand complexes are essentially molecules and each domain of LMMCT is locally responsible for the photoluminescence process.

Another main difference between the quantum-confined gold nanoclusters and gold-ligand complexes is the bonding between the gold atoms. Au-Au bond is essential for quantum confined gold clusters. Thus quantum-confined gold nanoclusters require a reductant for the formation of the core gold structure while it is not needed for the synthesis of gold-ligand complexes (Table 1.3).

A limitation inhibiting development of fluorescent gold nanoparticles into usable products has been the lack of a well-characterized and reproducible sample preparation that yields narrowly dispersed materials. From careful evaluation of reported spectral characteristics, it is clear that both quantum-confined clusters and ligand complexes can form under the same conditions and S-Au bonding between glutathione and core of the quantum-confined gold cluster, reported by Negishi et al.[64; 69; 70], is the same the covalent bonding between thiol to gold in gold-thiol complexes.

The pros and cons of the two types of photo-luminescent gold nanoparticles are summarized in the following table (Table 1.4).

**Table 1.4.** Summary of pros and cons of the two types of luminescent gold nanoparticles

	<b>Pros</b>	<b>Cons</b>
<b>Quantum confined gold nanoclusters</b>	High QY (> 0.1)	Requires stabilizing matrices; Difficult synthesis due to severe limitation on size (< 0.5 nm)
<b>Gold-ligand complexes</b>	Less limitation on its size	Weak photostability and photobleaching; Poor water solubility

#### 1.4. Outline and flow chart of the dissertation

A systematic plan to approach the development of photoluminescent gold nanoparticles with desirable properties for bio-imaging agents as described in section 1.2.4 was developed. An overall flow chart for this project is provided in Figure 1.3, and details are provided in the subsequent sections. The major parts were to establish the design criteria for the desired gold material, develop a reproducible synthesis, characterize the properties of the material and compare them to the desired properties, and redesign if needed.

##### 1.4.1. Design

After reviewing the references of the photoluminescent gold nanoparticles as described in section 1.3, it became clear to set a goal to develop photoluminescent gold nanoparticles for bio-imaging agents which can address the solutions for all the problems discussed. The ideal design of the photoluminescent gold nanoparticle would combine the advantages of the gold-ligand complexes and solid gold-cored nanoparticles (Table 1.4).

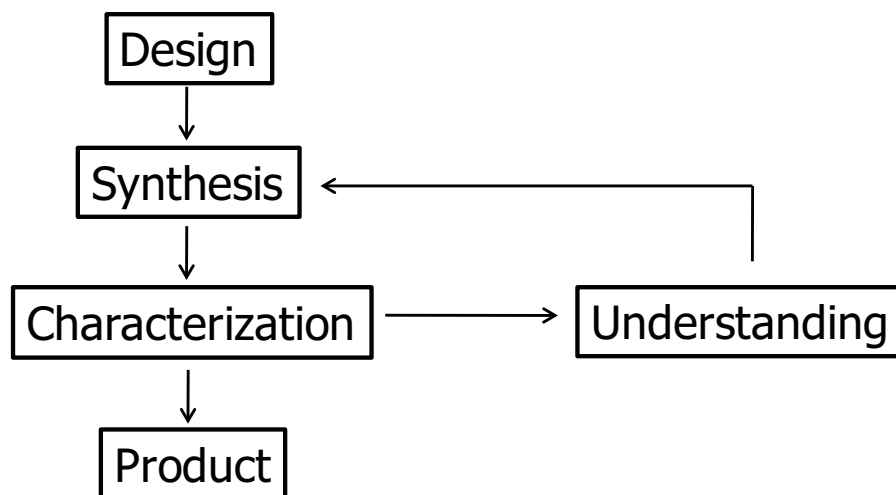


**Figure 1.3.** Systematic flow chart of the dissertation. Details of each are provided in the next sections.

By making the “hybrid” gold nanoparticles, we can expect to achieve the luminescent gold nanoparticles that possess these advantages while minimizing the disadvantages of both types of gold nanoparticles such as size limitation, matrix requirement and weak photostability. The gold-ligand complexes which are covalently bound on the surface of the core gold nanoparticle could improve the stability against the uncontrolled growth of gold nanoparticle. Any unbound gold atoms in the solution would be sterically hindered from accumulation by the surface-bound gold-ligand complexes that reduce the available sites for the Au-Au bonding from the core gold nanoparticle.

The structure of mercaptoalkanoic acid consists of two functional groups, thiol and carboxylic acid, at each end with a carbon chain backbone in between. Choosing the bifunctional mercaptoalkanoic acid molecules as a ligand could provide several advantages for the gold nanoparticle process in comparison with monofunctional thiols. Its S group works as a LMMCT forming domain as well as a gold core

stabilizing agent. The carboxylic acid group provides water solubility to the gold nanoparticle and it can also be utilized as a conjugation domain with possible signaling and/or drug molecules via ester or amide couplings. The pKa value of the carboxylic acid group is around pH 4.5~5 and the titratable range of pH is from pH 3 to pH 8. The carbon chain backbone is biochemically inert and its inherent hydrophobicity could create a surface layer can act as a carrier for the embedded hydrophobic molecules.

#### 1.4.2. Synthesis

A synthesis protocol was developed to produce a relatively pure suspension of gold nanoparticles ~2 nm in diameter surrounded by gold-ligand complexes in a simple one-pot synthesis. It is different from other gold-ligand complex protocols in using additional reductants and avoids the need for matrix for stabilization or tedious gel electrophoresis work-up. To produce the product, reducing agent was added to the pre-mixed starting solutions of gold and mercaptoalkanoic acid. Sodium borohydride was chosen for the reducing agent for its solubility and reducing power shown previously to be suited for the gold nanoparticle synthesis. The mixture was then sealed and stirred for 24 hr to avoid evaporation of the solvent. EtOH trituration was employed to separate the products from starting materials. Differences in solubility of the precursors, all of which are soluble in EtOH, and the product, results in precipitation of the final product. Simple centrifugation was sufficient to collect the product. The product pellet was dried and stored until further use. A detailed synthesis condition will be described in next chapter.

### 1.4.3. Characterization

The characterization of the properties of gold nanoparticle products included the physical properties such as mean size and zeta-potential as well as absorbance, emission and excitation spectra. The size was mainly analyzed by transmission electron microscopy (TEM) and dynamic light scattering (DLS) methods. TEM is a microscopy technique using a beam of electrons [73]. An image is generated from the electrons transmitted through the specimen after the interactions between the electrons and specimen. This technique enables one to verify fine structures as small as an atom owing to the small wavelength of electrons. DLS is a technique to determine the size distribution profile of small particles in suspension[74]. In this method, laser light is scattered by the particles which are constantly moving by Brownian motion and the distance of the particles' motion is correlated with the size of the particles. Then, the scattered light encounters either constructive or destructive interference with light scattered by the surrounding particles. Within this intensity fluctuation, the time scale of movement of the scatterers can be revealed. Also, gel electrophoresis was also performed for further size identification.

The zeta-potential[75] of the gold nanoparticle products was analyzed at different pHs to understand the iso-electric point and overall charge distributions of the materials. But in this case, repetitive oscillation of the electric field is applied to the suspension causing the movement of the charged particles and the scattered laser light by the particles determines the charge value of the particles.

The thiol to gold ratio was determined by the inductively coupled plasmon mass spectroscopy (ICP-MS) to identify the final compositions of the gold product[76]. The plasma creates high temperature up to 10,000 K and the ionized

substances breaks down in atomic level at this temperature and they are analyzed to determine the concentration.

The biocompatibility of the gold nanoparticles was tested in two different ways. First, cell viability test was performed using BEAS-2B cells (human pulmonary cancer cells). The gold nanoparticle solution was incubated with BEAS-2B cells and the cell viability was tested using Dojindo kit (Dojindo, Rockville, MD). Tetrazolium reagent changes to yellow colored formazan molecule by the dehydrogenase activity from the live cells. So, by analyzing the color change, the metabolic activity that is assumed to correlate with number of viable cells could be determined. Second, the effect of gold product on the formation and detectability of reactive oxygen species (ROS) was determined by the Amplex Red kit (Invitrogen, Carlsbad, CA). In this test the Amplex Red molecule is changed to fluorescent resorufin molecules by ROS in the presence of peroxidase. The ability of gold product to generate resorufin with and without added  $H_2O_2$  was determined, and a comparison made with other types of nanoparticles.

#### 1.4.4. Understanding

The effects of varied reaction conditions including different gold to ligand ratio, the length of stirring time of the synthesis mixture, different types of ligands, varying the length of the carbon chains and different polarity of solvents on the size and optical properties of gold nanoparticles was evaluated. A theory for gold nanoparticle nucleation and growth was presented after analyzing the time dependent optical property changes and assigning them to the four steps of ionization of starting materials, reduction of gold, formation of LMCT/LMMCT complexes and the formation of nanoparticles.

The emission change of the gold nanoparticles at different pHs was also studied to understand the limits of their use as a bio-imaging agent. The combined effect of salt and pH on the aggregation behavior was studied to understand the effect of the charges and the presence of charge screening species in the solution on the optical properties. Based on the result of this study, it was determined that the hydrophobicity of the stabilizing ligands affected the aggregation tendency. To better understand the complicated nature of the photoluminescence and optical properties of the gold nanoparticles, quantum chemistry calculations were used to identify the energy levels of the band gap system of gold bound mercaptooctanoic acid and uncomplexed mercaptooctanoic acid itself.

The simulation of the electronic structures of mercaptooctanoic acid-gold complexes was performed with density functional theory using the B3PW91 model and Pseudopotential Lanl2dz basis in the Gaussian03 program[77]. Two separate model systems were used, namely standalone mercaptooctanoic acid and complexes of the acid with one gold atom. Geometries of these model systems were fully optimized in an aqueous environment using a continuum PCM solvation model[78]. LUMO-HOMO gap was used to estimate the band gap.

#### 1.4.5. Product

The final gold nanoparticle product for bio-imaging was developed after numerous trials. The final product meets the criteria standard for a bio-imaging agent in terms of water-solubility, biocompatibility, photostability, adequate quantum yield, NIR range emission, and pH sensitivity. To show its ability as a bio-imaging agent, folate molecules were conjugated to the surface of gold nanoparticles and the attraction of these complexes to breast cancer cell line, MCF-7, was monitored.

### 1.5. Abstracts of each chapter

In this section, the abstracts of each chapter in this dissertation are provided to provide an overview of the accomplishments of this project.

#### 1.5.1. Abstract of Chapter 2

Water-soluble photoluminescent thiol-stabilized gold nanoparticles were produced using reductive reaction of gold salt and mercaptoalkanoic acid ligands at room temperature in aqueous solution. The origin of the observed photoluminescence was identified as coming from a ligand-metal-metal charge transfer complex. Electrophoresis and electron microscopy analyses along with studies elucidating the dependence of photoluminescence intensity on excitation wavelength suggest the charge transfer complexes are not free but are stabilized by interactions with nanoparticles which grow during the process leading to an enhanced emission intensity and greater stability against UV irradiation. Analysis of the excitation spectrum of the photoluminescent product reveals the interaction of both neutral and singly ionized gold atoms with the ligand complexes, which may be responsible for enhanced stability of these complexes compared with those produced as free molecules via other synthesis methods. The photoluminescence intensity was studied as a function of ligand concentration, ligand chain length, reductant concentration, solvent composition, particle size, and particle surface area, and indicated a relationship between photoluminescence intensity, nanoparticle size and polarity of the environment. The reductive synthesis is complicated by the reaction of the reductant with water which leads to variations in nanoparticle size and therefore photoluminescence intensity, but not wavelength. Time dependent spectroscopic changes during the first 48 hr of reaction suggested that the highly photoluminescent

product is a secondary product and may be the result of continued reduction of gold-thiol ligand complexes into nanoparticles.

#### 1.5.2. Abstract of Chapter 3

In this chapter, we have described the synthesis and properties of a pH responsive nanoparticle-supported molecular brush which utilizes the polarity-dependent photoluminescent signal of gold-thiol charge transfer complexes to report the pH change. This work shows that bifunctional molecular ligands in which one of the functional groups is protonatable while the other forms a stable bond with the gold nanoparticles can form a collapsible molecular brush on the surface of gold nanoparticles. By using a thiol-based ligand a polarity sensitive photoluminescent charge transfer complex can be localized at the particle periphery. When the brush is collapsed this species responds reversibly to the change in local polarity. The operational range of these materials is between pH 5 and 8, spanning the range of pH that are generally relevant in chemical and biological studies. The typical size of this material is about 2 nm, small enough for use in nanosized devices and intracellularly.

#### 1.5.3. Abstract of Chapter 4

ROS formation is an important method to determine biocompatibility of the material since it is widely known that the ROS can damage cells and tissues. The ROS formation by gold nanoparticles was tested using Amplex Red assay kit. The result showed that the presence of the gold nanoparticle in Amplex Red solution cause no sign of ROS generation. Interestingly, the result indicates that the gold nanoparticles even showed lowering the ROS comparing to the negative control, water, up to 20% less detection in the case of 0.2  $\mu\text{M}$  gold nanoparticles. This result suggests the

possibility of antioxidant activity of the gold nanoparticles. The effect of the metallic oxide nanoparticles on ROS formation and its effect on Amplex Red assay was also dealt as a positive control set and the detailed mechanisms of their effect were studied.

In comparison to the gold nanoparticles, other commonly used metallic oxide nanoparticles were also used to investigate the production of the ROS and its effect on the Amplex Red measurement. In this chapter, we have shown the effect of four different types of oxide nanoparticles, CeO<sub>2</sub>, Fe<sub>2</sub>O<sub>3</sub>, TiO<sub>2</sub> and SnO<sub>2</sub> on Amplex Red assay to detect H<sub>2</sub>O<sub>2</sub>. All four oxide nanoparticles showed intrinsic capability of converting Amplex Red molecules to fluorescent resorufin in the absence of H<sub>2</sub>O<sub>2</sub>. Also, during the Amplex Red assay in the presence of H<sub>2</sub>O<sub>2</sub> and horseradish peroxidase, CeO<sub>2</sub>, Fe<sub>2</sub>O<sub>3</sub> and TiO<sub>2</sub> nanoparticles under-reported the actual amount of H<sub>2</sub>O<sub>2</sub> while SnO<sub>2</sub> nanoparticle showed minimal effect. Similar trends were observed when these tests were repeated in cell culture media. The results suggest that there are catalytic effects of oxide nanoparticles to consume H<sub>2</sub>O<sub>2</sub> during the reaction. All kinetic parameters have been calculated and simulated concentration profile over time at different conditions has been performed using calculated parameters for the understanding of the complicated system. The significance of this work is showing the care is needed to be taken in interpreting the result of seemingly robust bioassays in the presence of nanoparticles.

### 1.6. Conclusions

In this chapter, current photo-luminescent bio-imaging techniques comparing to other bio-imaging techniques and the types of photo-luminescent gold nanoparticles were reviewed. During the review, pros and cons of the current technologies were summarized and the need for a better bio-imaging system was

stated. Based on the need for a new photoluminescent gold nanoparticles, the flow-chart of the dissertation was presented and each step of the chart was explained.

## CHAPTER 2

### SYNTHESIS, ANALYSIS AND PROPERTY OF MERCAPTOALKANOIC ACID STABILIZED GOLD NANOPARTICLES

#### 2.1. Abstract

In this chapter is described the synthesis, characterization and understanding parts of the flow chart described in the preceding chapter (Figure 1.4.). The production of water-soluble photoluminescent thiol-stabilized gold nanoparticles using reductive reaction of gold salt and mercaptoalkanoic acid ligands at room temperature in aqueous solution is described. Characterization of the product by electrophoresis and electron microscopy analyses is followed by studies elucidating the dependence of photoluminescence intensity on excitation wavelength. Through these studies we have understood that charge transfer complexes have been formed. These charge transfer complexes are stabilized by interactions with nanoparticles which grow during the process leading to an enhanced emission intensity and greater stability against UV irradiation. Analysis of the excitation spectrum of the photoluminescent product reveals the interaction of both neutral and singly ionized gold atoms with the ligand complexes, and this interaction may be responsible for enhanced stability of these complexes compared with those produced as free molecules via other synthesis methods. The photoluminescence intensity was studied as a function of ligand concentration, ligand chain length, reductant concentration, solvent composition, particle size, and particle surface area. The results indicated a

relationship between photoluminescence intensity, nanoparticle size and polarity of the environment. The reductive synthesis is complicated by the reaction of the reductant with water which leads to variations in nanoparticle size and therefore photoluminescence intensity, but not wavelength. Time dependent spectroscopic changes during the first 48 hr of reaction suggested that the highly photoluminescent product may be the result of continued reduction of gold-thiol ligand complexes into nanoparticles.

## 2.2. Introduction

Gold-thiol ligand complexes and thiol-stabilized gold nanoclusters have generated significant scientific and technological interest. However, because gold complexes experience strong aurophilic attractions [67], unless they are separated or protected, aggregation takes place and a mixture of variously sized materials is produced. This situation has led to difficulties in determining some of the properties of the individual species and identifying the synthesis parameters needed to obtain them in significant quantities. The purpose of this study is to understand the effects of reductant concentration, alcohol concentration, ligand concentration and ligand chain length on the formation of water-soluble photoluminescent gold-thiol ligand complexes and thiol-stabilized gold nanoclusters or nanoparticles. Water solubility is a necessary prerequisite for use of these materials in many applications. For example, some photoluminescent gold-based materials have potential as two photon imaging agents and could be a safer to alternative Zn- and Cd-based quantum dots in theranostic applications.

As they are discussed in the Chapter 1, many of the reported syntheses of photoluminescent gold complexes and gold nanoclusters take place in nonaqueous

solution or inside the hydrophobic regions of a polymer (Table 1.3). Largely, we can categorize the photoluminescent gold nanoparticles in the table into three types. These are 1) gold-ligand complexes, 2) gold clusters stabilized in dendrimers or polymer matrices and 3) gold clusters stabilized by surface ligands. Negishi et al.[64; 69; 70] have produced gold clusters stabilized with surface ligands, glutathione, and showed it was possible to physically separate variously-sized photoluminescent complexes and nanoclusters using SDS-PAGE as long as the synthesis and the electrophoresis were performed at cold temperatures to slow further development. This procedure is inherently low yield. Zheng et al.[32] led the development of quantum confined gold clusters stabilized in dendrimers and showed that the formation of gold-thiol complexes and nanoclusters could be better controlled if they took place in the hydrophobic void spaces of dendrimers. However, the photoluminescent properties of the gold materials produced seem to be quite different from that of the gold-thiol complexes and nanoclusters developed by Negishi et al. Adding to the confusion, recently Huang et al.[62] reported weakly luminescent water-soluble mercapto-alkanol-stabilized gold nanoparticles 1-3 nm in diameter similar in appearance to nanoclusters reported by Negishi et al., but with photoluminescence wavelengths corresponding to ligand-metal charge transfer (LMCT) and ligand-metal-metal charge transfer (LMMCT) complexes. They also indicated that the emission wavelength could be shifted over the visible range (i.e., from 620 nm to ~490 nm) by varying the chain length of the mercaptoalkanol ligand in the synthesis which affected the nanoparticle size. Susa et al. reported similar, albeit unstable, materials in a polymer matrix[53].

In this study, we focus on a more detailed understanding of the reductive production of fluorescent gold complexes and nanoparticles in water using  $\text{NaBH}_4$  as

the reductant and structurally simple mercaptoalkane carboxylic acids as ligands. Under reductive conditions, gold particle nucleation [79; 80] as well as particle growth takes place alongside ligand charge transfer complex formation. Reaction of the reductant  $\text{NaBH}_4$  with water competes with these processes. Following purification of the product by trituration,  $\sim 2$  nm diameter gold nanoparticles decorated

with thiol-ligands exhibiting the widely Stokes shifted emission of the type  $\begin{matrix} \text{Au} \\ \updownarrow \\ \text{Au} \end{matrix} \text{SR}$  (i.e., 2.03 eV or  $\sim 610$  nm) were produced. Electrophoresis gave no evidence for free gold-thiol clusters as reported by Negishi et al. The nanoparticle size was found to be adjustable in a variety of ways by altering the chain length of ligand, the amount of ligand, the reducing power of the reaction mixture, and the ethanol content in the reaction mixture. Although the emission intensities were found to depend on particle size, in contrast to the work of Huang et al.[62] the emission wavelength remained fixed. The emissive species had an unusually assymmetrically shaped excitation spectrum with maximum significantly blue-shifted compared to what is expected from free gold-ligand complexes. The production of luminescence was not immediate, but its appearance was delayed for over an hour after reagent mixing. An isosbestic point in the time dependent absorption spectra suggests that the formation of the luminescent species is the result of a two state conversion from an initially formed primary species.

### 2.3 Materials and methods

#### 2.3.1. Materials

Mercaptooctanoic acid ( $\text{C}_8\text{H}_{16}\text{O}_2\text{S}$ ) (MOA), mercatohexanoic acid ( $\text{C}_6\text{H}_{12}\text{O}_2\text{S}$ ) (MHA), mercaptododecanoic acid ( $\text{C}_{12}\text{H}_{24}\text{O}_2\text{S}$ ) (MDA), mercaptopropanoic acid

(C<sub>3</sub>H<sub>6</sub>O<sub>2</sub>S) (MPA), hydrogen tetrachloroaurate (HAuCl<sub>4</sub>), sodium borohydrate (NaBH<sub>4</sub>), ethanol (EtOH), fluorescein and all solvents used in this paper were purchased from Sigma (St. Louis, MO). Precast Tris-HCl 4-15% gradient gel, tris-glycine SDS buffer and Laemmli sample buffer were purchased from Bio-Rad (Hercules, CA). Formvar-coated carbon TEM grids were obtained from Ted Pella (Redding, CA).

### 2.3.2. Gold nanoparticle synthesis

The standard synthesis for gold nanoparticles involved mixing 2.30 mL of 0.01087 M HAuCl<sub>4</sub>•3H<sub>2</sub>O solution (9.8 mg, 0.025 mmole), with 1.75 mL of water solution containing various amounts of sodium borohydride (0.375 mmole, 0.25 mmole, 0.2 mmole, 0.15 mmole, 0.1 mmole), and 0.45mL of ethanol solution containing various amounts of mercaptoalkane carboxylic acid (0.025 mmole, 0.0375 mmole, 0.05 mmole, 0.075 mmole, .0875 mmole, 0.1 mmole, 0.125 mmole). For some syntheses, 0.45mL of ethanol solution containing mercaptopropanoic acid, mercaptoheptanoic acid, or mercaptododecanoic acid (0.025 mmole) was added instead of mercaptooctanoic acid.

The sequence of mixing was the addition of mercaptoalkane carboxylic acid solution to a previously prepared gold solution, followed by addition of NaBH<sub>4</sub> solution, each added within 10 sec of the other. Parafilm was used to seal the top of flask to prevent evaporation while the mixture was stirred overnight at 600 rpm in 25 °C. The next day, sample was separated into three pre-weighed 1.5 mL centrifuge tubes and centrifuged at 12,000 rpm for 10 min at 25 °C to pellet any large particulates that might have formed. The supernatant containing the fluorescent product was decanted and triturated twice using 200-proof EtOH (with 1 to 100

dilution with EtOH), allowing the fluorescent product to precipitate and be pelleted by centrifugation (12000 rpm, 10 min) using an IEC Micromax RF bench-top centrifuge (Thermo Scientific, Waltham, MA). This purified pellet was dried under vacuum for 3 days and was resuspended in E-pure water to make a concentration of 0.2 mg/mL. The final pH of the gold nanoparticle suspension was 8.5 and all the experiments were conducted at this pH unless noted otherwise.

### 2.3.3. Electrophoresis

SDS-Page gel electrophoresis was performed using a Mini-Protean 3 cell from Bio-Rad (Hercules, CA) using precast Tris-HCl 4-15% gradient gel, Tris glycine SDS buffer and Laemmli sample buffer. To prepare the sample mixture, a triturated pellet of mercaptooctanoic acid stabilized gold nanoparticles containing 1  $\mu$ M particles was redispersed in 1mL in E-pure water and mixed with sample buffer at 1:1 (v/v) ratio. Then, 30  $\mu$ L of sample mixture was loaded in the well of the gradient gel and 200V applied for 1 hour until the smallest size marker reached the bottom of the well. The gel was carefully removed from its cassette and luminescence from the gold nanoparticles observed by placing the gel on the surface of a UV transilluminator (White/UV transilluminator, Upland, CA) providing 254 nm excitation light. The luminescent image was recorded using a Canon digital camera for further analyses. The size ladder in the gel could be observed via absorbance of the UV light as dark lines seen in the image.

### 2.3.4. Mass spectrometry measurements

ICP-MS analysis using an Agilent 7500ce mass spectrometer (Santa Clara, CA) was used to obtain the gold ( $m/z$  197) content of aqua regia-digested samples. The

samples were diluted (1 in 100) in 5% HNO<sub>3</sub> and run together with a calibration curve prepared from a soluble gold standard (Inorganic Ventures, Madrid, Spain). Iridium (3.3% in HCl, Inorganic Ventures) was used as internal standard (m/z 192). A self aspirating PTFE nebulizer (ESI Scientific), PTFE cyclonic spray chamber (PC3 Elemental Scientific), and platinum cones were used. For sulfur (m/z 32) content analyses, the samples were diluted (1 in 2) using 2.4 % HNO<sub>3</sub> and run together with a calibration curve prepared from a soluble sulfur standard (H<sub>2</sub>SO<sub>4</sub>, Inorganic Ventures). In this case terbium (m/z 159) was used as internal standard. To discount any interference of gold in the solution on the detection of sulfur, a known amount of sulfur standard (10 ppm) was mixed with the different concentrations of gold (0, 5, 10, 15 and 20 ppm). Result showed there was no interference effect.

#### 2.3.5. Transmission electron microscopy

Transmission electron microscopy images were obtained using a JEOL JSM840a TEM at the Electron Microscopy facility at Brigham Young University, Provo, UT and Tecnai T12 TEM (Philips, Andover, MA) operated at 120 kV with the magnification of 666,667 X for observation from the Heath Science Core Facility in the University of Utah. A 5 µL drop of gold nanoparticle solution was allowed to air-dry on the center of the TEM grid at room temperature.

#### 2.3.6. Absorption spectrometry

Absorption spectra of the gold nanoparticle suspensions containing 1 µM of particles at pH 8.5 and pH 3 were recorded between 200-800 nm at room temperature, using a Shimadzu UV mini 1240 (Kyoto, Japan) absorption spectrophotometer, in 1 cm path length quartz cuvettes at 20 °C. Spectrometer resolution was ±2 nm.

### 2.3.7. Fluorescence spectrometry

Fluorescence emission spectra of gold nanoparticle suspensions containing 1  $\mu\text{M}$  of gold particles were obtained from 400 nm to 800 nm at 20  $^{\circ}\text{C}$  using a Cary Eclipse spectrophotometer from Varian (Palo Alto, CA). An excitation wavelength of 290 nm was used. Samples were placed in a 1 cm quartz Suprasil cuvettes, and spectrometer slit width was fixed to 5 nm to obtain a spectral resolution of 1 nm. The excitation spectra monitoring 610 nm emission as a function of excitation wavelength between 200 and 600 nm were taken using the same instrument. All spectra were obtained at pH 8.5 unless otherwise noted.

### 2.3.8. NaCl concentration effect

NaCl was added to the gold nanoparticle solution and its effect on absorbance and emission along with DLS measured mean size was measured. Concentrated NaCl solution (4M) was prepared in deionized water and added to 2 mL of gold nanoparticle solution to prepare mixtures containing the following concentrations of NaCl: 0, 12.5, 25, 50, 75, 100, 125, 150, 200, 250 and 300 mM.

### 2.3.9. Fourier transform infrared spectroscopy

FT-IR spectra were measured by putting a 10  $\mu\text{l}$  drop of concentrated sample (2 mg / 50  $\mu\text{L}$ ) on the crystal of an ATR cell (Varian 3100FT-IR, Palo Alto, CA). Spectra were obtained over the range of 40-4000  $\text{cm}^{-1}$ . Pure mercaptoalkane carboxylic acid and water were analyzed as controls.

### 2.3.10. Relative quantum yield measurement

The relative emission quantum yield of the gold nanoparticle stabilized with mercaptooctanoic acid was calculated in reference to the known quantum yield, 0.95 of an aqueous fluorescein dye solution [1]. A series of gold suspensions were prepared by diluting the as-prepared gold suspension by 2 to 20 times and the fluorescence yield relative to absorbance was measured. The maximum fluorescence yield was obtained by extrapolating the curve to infinite dilution in order to avoid problems with self quenching. A similar plot and extrapolation was obtained for fluorescein solutions prepared over the range of 0.01 to 1 uM in concentration. The relative quantum yield  $\Phi_{gold}$  of the gold product was obtained by:

$$\Phi_{gold} = \frac{\left(\frac{Fl}{Abs}\right)_{gold}^{max} 0.95}{\left(\frac{Fl}{Abs}\right)_{fluorescein}^{max}}$$

### 2.3.11. Simulation

The simulation of the electronic structures of mercaptooctanoic acid-gold complexes was performed with density functional theory using the B3PW91 model and Pseudopotential Lanl2dz basis in the Gaussian03 program [78] at the Center for High-Performance Computing, University of Utah. Two separate model systems were used standalone mercaptooctanoic acid and complexes of the acid with one gold atom. Geometries of these model systems were fully optimized in aqueous environment using a continuum PCM solvation model LUMO-HOMO gap energies were estimated in the usual manner.

### 2.3.12. Lifetime measurement

Gold nanoparticle suspensions were placed in a UV-transparent cuvette and positioned 2 cm in front of a photomultiplier tube (R636P, Hamamatsu Photonics, Hamamatsu, Japan) with a 10 ns rise time. The excitation wavelength at 266 nm was generated as the fourth harmonic of a Nd:YAG regenerative amplifier (4400 series, Quantronix, East Satauket, NY). The average laser power was measured to be 0.2 mW. A repetition rate of 770 Hz was used. The photomultiplier signal was collected with an SR400 photon counter (Stanford Research Systems, Inc., Sunnyvale, CA) triggered by the excitation pulse using a moving gate. Exponential decay fitting using the following equation,  $y = A * \exp(-\frac{x}{t}) + B$  was used to obtain the lifetime of the emission from the recorded data.

### 2.3.13. Cytotoxicity test

For cytotoxicity assays, gold nanoparticle suspensions were dialyzed overnight at pH 7.4 in cellulose dialysis membranes with molecular weight cut-off (MWCO) 1000, sonicated for 15 min in a bath sonicator, diluted by a factor of 9:1 in PBS to give a final concentration of 137 mM NaCl, 2.7 mM KCl, 4.3 mM Na<sub>2</sub>HPO<sub>4</sub> and 1.47 mM KH<sub>2</sub>PO<sub>4</sub>. The mixture was boiled for 5 min. There was no effect observed on the property of gold nanoparticles for boiling. The gold nanoparticle suspensions were diluted by 9:1 in OptiMEM cell culture medium. Appropriate volumes were added to microplate wells (Nunc, Thermo Fisher Scientific, Rochester, NY) pre-seeded with BEAS-2B endothelial cells (immortalized pulmonary cell line, CRL-9609 from ATCC). This is a widely used cell type for cell viability testing [81]. The cells were seeded (20k/cm<sup>2</sup>) in the microwell plate and grown for two days in OptiMEM cell culture media at 37 °C, in a 5% CO<sub>2</sub> chamber. The cells were

incubated with the gold nanoparticles in a series of doses ranging from 0.065 nM to 1  $\mu$ M for 24 hr at 37 °C, in a 5% CO<sub>2</sub> chamber (VWR, West Chester, PA). After this period, cell media was replaced with fresh the Opti-MEM culture media containing 4% of the WST-8 reagent (CCK-8, Dojindo Laboratories, Gaithersberg, MD). The plates were incubated at 37 °C for an additional 2 hr before reading of absorbance at 460 nm using Molecular Devices plate reader (Sunnyvale, CA). During this process, the tetrazolium reagent is changed into yellow-colored formazan after reducing reaction by dehydrogenase of living cells. Thus the absorption by the formazan molecule at 460 nm is directly related the amount of the viable cells.

#### 2.3.14. Photobleaching test

Gold nanoparticles (200 nM) and fluorecein solutions (19 nM) in a 1 cm path length quartz cuvette mounted in a water-cooled jacket at 30 °C. The output from a 300W Xenon arc lamp (14200 LUX at the sample position) was directed at the cuvette and the fluorescence spectrum of the sample was measured every 5 min. The experiment was performed in water and pH 8. For comparison of the light intensity, the microscope stage was exposed to the light with the intensity of 7320 LUX.

#### 2.3.15. Preparation of gold-PEG-folate conjugate and imaging

Folate was first conjugated to monoamino-PEG (polyethyleneglycol) by mixing folate (0.1 mmol, 0.0389 g) in 10 mL of a 1:1(v/v) water:DMSO mixture and adding EDAC (1-Ethyl-3-[3-dimethylaminopropyl]carbodiimide Hydrochloride, 0.1 mmol, 0.0192 mmol) and SNHS (N-hydroxysulfosuccinimide, 0.1 mmol, 0.0217 g). The mixture was stirred for 10 min at 600 rpm in a 20 mL glass vial. Monoamino-PEG (0.1 mmol, 0.0149 g) was added to the stirring mixture and stirring continued

overnight in a sealed vial at room temperature. A yellow colored solution was obtained that contained folate-monoamino-PEG conjugates. The product was not analyzed further or purified, because it is known that  $\gamma$ -carboxylic acid is more reactive than  $\alpha$ -carboxylic acid about 8:2 reaction ratio[82]. Most of the applications for the folate directed drug delivery reported so far do not consider the difference of the conjugation position important and a mixture of conjugates involving  $\alpha$  and/or  $\gamma$ -carboxylic acid are used without any further purification[82; 83; 84]. Therefore we have also used this conjugate as synthesized for further application.

Two mL of gold suspension (containing 0.4 mg of gold) was mixed in a separate container with the ester bond formation coupling agents EDAC (0.67  $\mu$ mol, 0.128 mg) and DMAP (0.33  $\mu$ mol, 0.04 mg) and stirred for 10 min. The folate-monoaminePEG conjugate solution (containing 0.67  $\mu$ mol of folate, 67  $\mu$ L) was added to the gold suspension and the mixture stirred at 600 RPM overnight at 20°C. The final 2 mL of product was dialyzed three times against 1L deionized water using a 1kDa MWCO cellulose dialysis membrane (SpectraPor, Rancho Dominguez, CA) to remove unreacted materials while retaining the newly formed gold nanoparticle-monoamine-PEG-folate conjugate. This purified material was stored in the dark at room temperature until used.

For microscopic imaging, one  $\mu$ M gold nanoparticle suspension was used for incubation with cultured cells. The gold nanoparticle was purified by EtOH trituration and E-pure filtered water was used for the resuspension of the gold nanoparticles. The gold nanoparticle solution was boiled for 3 min in the water bath for the sterilization before the cell incubation. MCF7 and A549 cells were exposed to gold nanoparticles for 4 hr at 37 C° at the incubator. Fluorescence microscope images of the cells after incubation and rinsing off of the supernatant were obtained using a Olympus IX71

fluorescence microscope (Olympus America Inc., Melville, NY) with Qimaging Retiga 1300 color CCD camera (Quantitative Imaging Corporation, Burnaby, BC, Canada). Specimens were prepared by placing 5 uL of the cell solution on the glass slide and covering it up with glass cover slip. The microscope images were taken at an exposure time of 20 ms and 50X magnification. The light intensity at the point of illumination was approximately  $1 * 10^9$  Lux/ m<sup>2</sup>.

#### 2.4. Result and discussion

##### 2.4.1. Electrophoresis, ICP MS, TEM and FT-IR

The final photoluminescent product produced after 48 hr of reaction, and purified with trituration, exhibited an absorbance maximum at 290 nm and emission at 610nm. Electrophoresis showed that the material consisted of relatively monodisperse nanoparticles with electrophoretic migration properties similar to that of MW markers ~120 kDa in size (Figure 2.1A). For an Au<sub>25</sub> cluster, the reported electrophoresis band position was 10 kDa[64], so the 120 kDa band observed in this study corresponds to a particle with over 300 Au atoms. This value is also consistent with the particle size estimated from TEM analyses (Figure 2.1B). Notable, was the absence of any bands in the 10-30 kDa range which are typical of molecular-sized ligand complexes [64; 69; 70].

HRTEM showed particles with a clearly visible atomic lattice (Figure 2.1C). Detailed analysis of the images using Photoshop (Adobe, San Jose, CA) allowed the estimation of the average d-spacing of the gold lattice in the nanoparticles of ~0.22-0.24 nm. This value is very close to that of other reported Au (111) lattice spacings (0.235 nm and 0.312nm [85]). Using the density of pure gold, 19.32 g/cm<sup>3</sup>, one Au

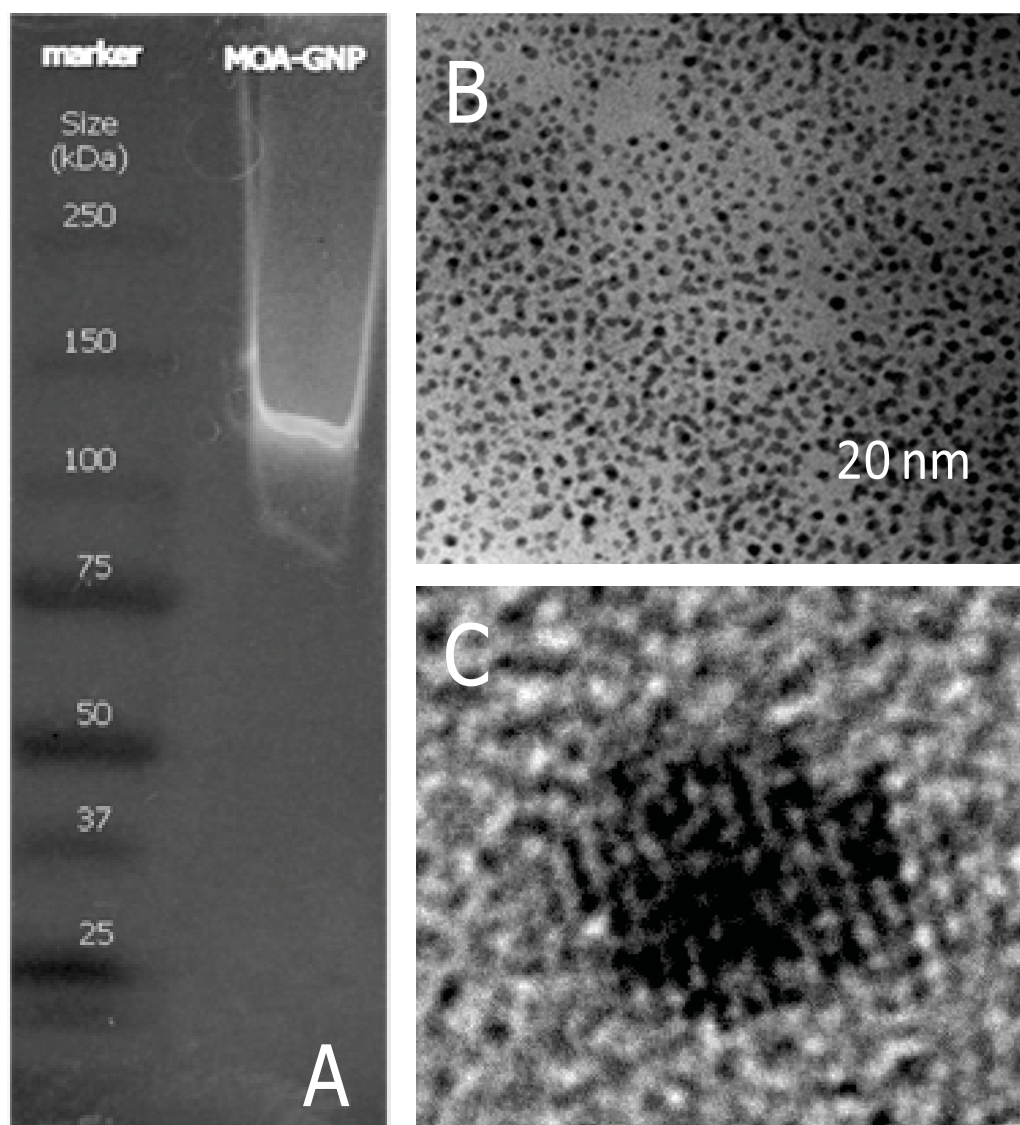


**Figure 2.1.** Characterizations of gold nanoparticle **A)** Image of the electrophoresis gel showing (right lane) mercaptooctanoic acid-stabilized gold particles and 25-250 kDa MW markers (left lane). The gel is illuminated using 254 nm UV-excitation so the gold particles appear brightly fluorescent while the MW marker appears as dark black lines. **B)** TEM micrograph of luminescent gold product produced using reductive aqueous synthesis using a 3:1 molar ratio of gold to ligand. The average particle size is  $2.2 \pm 0.6$  nm. **C)** High resolution TEM micrograph of the particles obtained.

atom should occupy  $0.017 \text{ nm}^3$ . Since the volume of a 2.2 nm diameter (radius,  $r=1.1 \text{ nm}$ ) gold nanoparticle is  $5.58 \text{ nm}^3$ , the number of Au atoms in a 2.2 nm diameter gold nanoparticle should be about 333. Therefore, both TEM and electrophoresis measurement are in agreement. ICP-MS analyses of gold and sulfur content in the final product showed that the gold to sulfur molar ratio was 1:0.27. Although this ratio is consistent with what is calculated for gold nanoparticles in the 2 nm diameter range such as  $\text{Au}_{309}(\text{thiol})_{75}$  to  $\text{Au}_{225}(\text{thiol})_{68}$  [86], similar values have also been reported for samples in which polynuclear  $d^{10}$  metal complexes [47; 50] making this result somewhat inconclusive.

ATR-FTIR spectrum of the purified photoluminescent product was compared to that of pure mercaptooctanoic acid (Figure 2.2). The result indicated the loss of SH stretch vibrations in the product sample, which is consistent with the formation of gold thiol ligand complexes. A shift of the characteristic C=O stretch and  $\text{CH}_2$  bend vibrations to lower wave number are consistent with a strong interaction of this molecule with another entity, which is suggested later to be an underlying gold nanoparticle support.

#### 2.4.2. Spectroscopy and computational analysis

The aim of the theoretical calculation was to show graphically the expected location of the emissive active site of the Au-S species. The existence of charge transfer complexes and the nature of the active species have been speculated in the past, and this calculation confirms that the active site will be located underneath the ligand layer on the particle surface. MOA has no appreciable emission of its own, and its HOMO-LUMO gap energy obtained experimentally and by calculations is in the far UV (Table 2.1). Simulated orbital isosurfaces obtained using the Gaussian 3

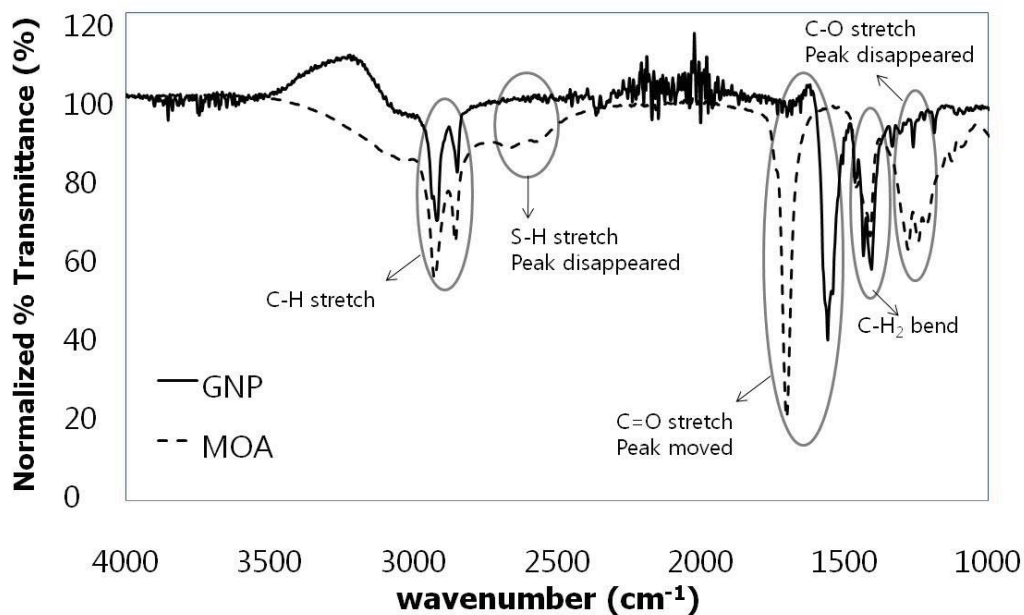


**Figure 2.2.** ATR-FT-IR spectra; gold nanoparticle product (solid line) and mercaptooctanoic acid (dotted line). Loss of SH stretch is consistent with the formation of gold-thiol bonding, and shift of C=O stretch and C-H<sub>2</sub> bend vibrations to lower wavenumber with a strong interaction of this molecule with another species, likely the gold nanoparticles present in the sample.

**Table 2.1.** Calculated and experimental HOMO-LUMO gap energies

Molecule	Solvent/Polarity index	HOMO-LUMO Calculation (eV)	HOMO-LUMO Experiment (eV)	Emission (eV)	Stokes shift (eV)
MOA	Dichloromethane/3.1		5.44		
only	Isopropanol/3.9		6.11		
	Ethanol/5.2		6.14		
	Water/9	5.90	6.30		
Au-MOA	Isopropanol/3.9		4.77	2.03	2.74
	Ethanol/5.2		4.43	2.03	2.40
	Water/9	3.80	4.28	2.03	2.25

program show that for unbound MOA, the LUMO orbital is located at the carboxylic acid group and the HOMO orbital is located at the thiol end region of the molecule (Figure 2.3). When complexed to one or more gold atoms, a significant change in orbital distribution takes place, and the isosurface plot shows that both molecular orbitals become located at the sulfur end of the molecule. This difference results in a shift of the HOMO-LUMO energy gap to lower energy (Table 2.1).

The spectral trends of unbound MOA and gold-complexed MOA produced in this work in solvents of different polarity are also consistent with a major difference in orbital distribution of the two species. As solvent polarity increases, the energy of the singlet excited state of MOA shifts to higher energy (Table 2.1). A blue shift of the excitation spectrum with increasing polarity is rather unusual and suggests that the absorbing species is already quite polar and additional stabilization by dipole-dipole interactions with water has minimal effect. This is consistent with the isosurface plots shown in Figure 2.3, which show that the HOMO is at the sulfur terminus of the molecule, while the electronegative carboxylic acid group is at the opposite end.

In contrast, for gold-MOA complexes, the excitation maxima red shifts with increasing polarity (Table 2.1) suggesting an absorbing species that has a comparatively smaller dipole moment. This too is consistent with the isosurface plots. There are few studies of the dependence of solvent polarity on gold-complexed MOA HOMO-LUMO energies with which to compare. Lee et al. [87] reported differences in the stability of reduced versus oxidized ligand complexes produced electrochemically, but their material was very different and had near infrared emissions 1.38 eV (~902 nm) and 1.2 eV (~1025 nm) with a HOMO-LUMO gap of only 1.33 eV.

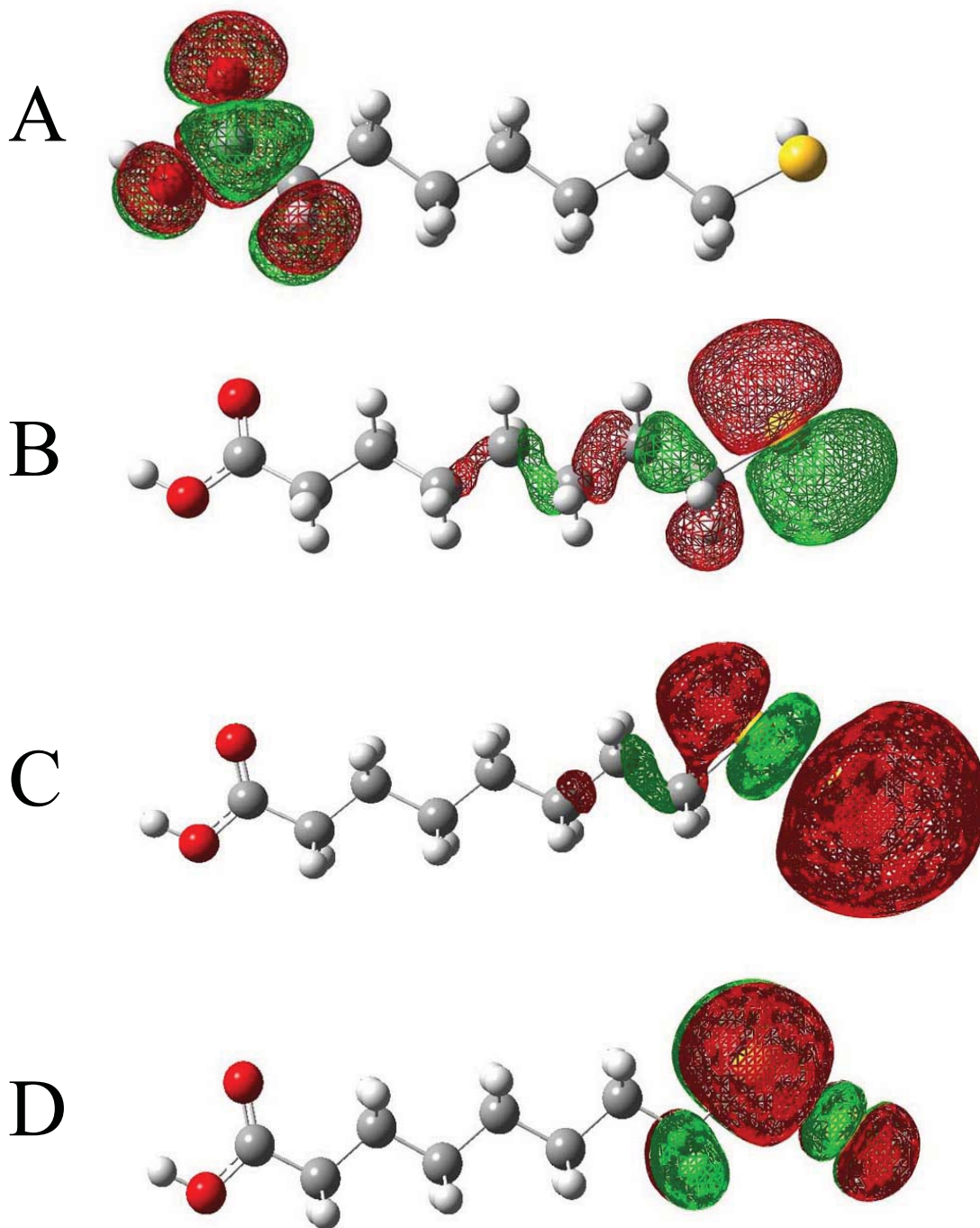


**Figure 2.3.** Gaussian3 simulated orbital isosurfaces of Mercaptooctanoic acid, **A)** LUMO. **B)** HOMO and gold-mercaptopentanoic acid, **C)** LUMO, **D)** HOMO. Yellow spheres: sulfur, Red spheres: oxygen, Grey spheres: carbon: White sphere: hydrogen.

The final product produced in this synthesis exhibited an absorbance and excitation spectra with maximum at  $\sim 4.3$  eV (290 nm), and an emission maximum at 2.03 eV (610 nm). According to Tzeng et al.[56], complexes with an intrinsic absorbance maxima at around  $\sim 3.1$  eV (400 nm), and very weak emission at  $\sim 2.7$  eV (477 nm) are of the type Au-SR and are referred to as LMCT complexes, while those with an absorbance at  $\sim 3.9$  eV (320 nm) and a very intense emission  $\sim 1.94$  eV (640

nm) are LMMCT with an  $\begin{matrix} \text{Au} \\ \uparrow \\ \text{Au} \end{matrix} \text{SR}$  configurations. Variations in these parameters are sometimes attributed to mixing with metal centered orbitals.

Based on the emission wavelength and emission lifetime of 1.45  $\mu\text{s}$  an LMMCT species seems likely [54]. The blue-shifted excitation energy maximum to 4.3 eV (290 nm) for the complexes produced here compared to that of other reported ligand complexes can be understood in terms of overlap of the electronic orbitals of gold atoms and CT complexes with the resulting wavefunction having more amplitude on the gold. According to Vogler et al.[52], the oxidizing and reducing ability of the ligand plays an important role in this mixing, so different types of ligands are expected to display different characteristics. As summarized in Table 2.2, the ionization spectra of neutral and singly ionized Au[88; 89; 90] show numerous strong or persistent lines (Table 2.2). Features in the asymmetric excitation spectrum obtained from samples prepared using MOA seem to correlated with at least some of these lines (Figure 2.4A, Table 2.2). These features are unique to this sample, and are well-reproduced from sample to sample.

The fact that excitation using any of the wavelengths associated with gold ionization leads only to LMMCT emission at 610 nm strongly suggests that the ligand metal complexes are strongly associated with both neutral and Au (I) gold atoms. An

electronic energy diagram illustrating this relationship is shown in Figure 2.4B. In this diagram excitation of gold or the complex leads to triplet emission from the complex. As a result of the electronic interaction between gold atoms and the ligand complex, there is a decrease in photodegradation of the photoluminescent complex under UV excitation, over what has been reported for other gold-thiol complexes in

**Table 2.2.** List of energies and wavelengths of persistent or strong lines in neutral Au and single ionized Au [88; 89; 90], compared to features in the excitation spectrum of MOA-Au nanoparticles produced in this work. (\*Au(I) refers to the absorption spectrum of neutral gold atoms, while Au(II) refers to the absorption spectrum of single ionized gold atoms.)

Experiment (eV(nm))	Persistent lines (eV(nm))	Strength	Spectrum*	Configuration
--	6.15(202)	1000	Au(I)	$5d^9 6s^2 - 5d^9 (^2D_{3/2}) 6s 6p (^3P^0_1)$
<b>5.52 (225)</b>	5.49(226)	700	Au(II)	$5d^9 (^2D_{3/2}) 6p \rightarrow 5d^9 (^2D_{3/2}) 7s$
<b>5.09(244)</b>	5.11(243)	250	Au(I)	$5d^{10} 6s \rightarrow 5d^{10} 6p$
<b>4.61(269)</b>	4.63(268)	300	Au(I)	$5d^{10} 6s^2 \rightarrow 5d^9 (^2D_{5/2}) 6p$
<b>4.48 (277)</b>	4.51(275)	100	Au(I)	$5d^9 6s \rightarrow 5d^{10} 6s 6p (^3P^0_1)$
	4.43(280)	600	Au(II)	$5d^9 (^2D_{5/2}) 6p - 5d^9 (^2D_{5/2}) 7s$
<b>4.39(283)</b>	4.40(282)	1000	Au(II)	$5d^9 (^2D_{3/2}) 6p \rightarrow 5d^9 (^2D_{3/2}) 7s$
<b>4.28(290)</b>	4.3(289) &	400	Au(II)	$5d^9 (^2D_{3/2}) 6p \rightarrow 5d^9 (^2D_{3/2}) 7s$
	4.25(292)			
<b>4.10(303)</b>	4.14(300) &	400	Au(II)/Au(I)	$5d^9 (^2D_{5/2}) 6p - 5d^9 (^2D_{5/2}) 7s$ &
	4.10(303)			
<b>3.94(315)</b>	3.98(312)	150	Au(I)	$5d^9 6s^2 \rightarrow 5d^{10} 6p$

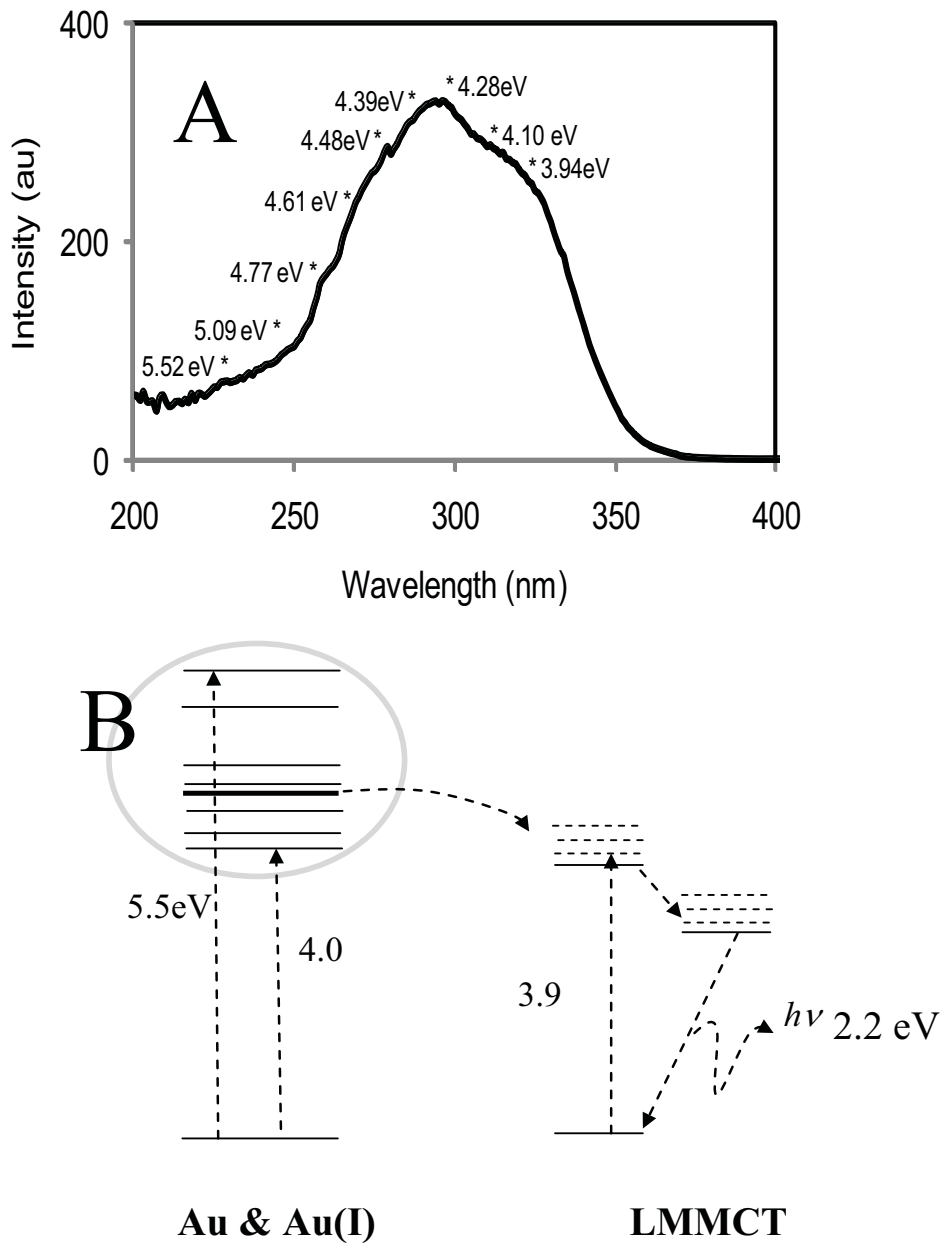


**Figure 2.4.** Gold nanoparticle excitation spectrum and proposed energy diagram; **A**) Excitation spectrum obtained by monitoring the emission at 2.2 eV (~610nm) of luminescent gold produced in this work. Mark points landmark the known positions of persistent line in Au(0) and Au(I) spectra from references [89; 90; 91]. **B**) Electronic energy levels of Au(0) and Au(I) relative to the ligand-metal-metal charge transfer complex (LMMCT) formed by reaction of gold with mercaptoctanoic acid.

free solution without the presence of nanoparticles [51] (Figure 2.5). In this graph the optical density in the visible at 598 nm is monitored over time as a measure of particle agglomeration.

The photobleaching test was performed for the gold nanoparticle solution with the comparison of the fluorescein solution. The two solutions were exposed to the same intensity of the light (14600 lux) and the photoluminescence was monitored every 5 min. As shown in Figure 2.6, the photoemission did not change significantly. In this experiment, while the control, fluorescein solution lost most of its fluorescence emission after 50 min of light exposure, the gold nanoparticle solution maintained its photoluminescence up to 84% of its original strength. These two photostability test results showed the gold nanoparticle has a superior stability than gold-ligand complexes and other fluorescent dye molecules.

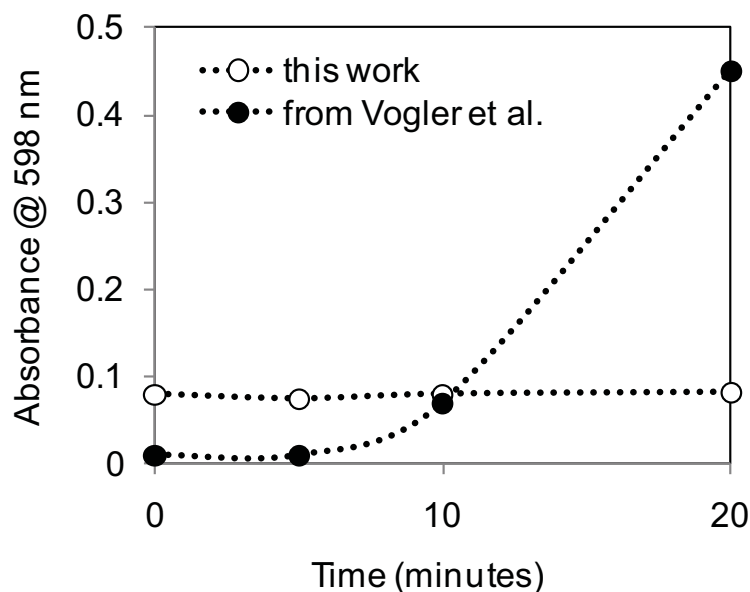


**Figure 2.5.** Photostability of luminescent gold materials exposed to of light from a 300W xenon arc lamp. Open circles (this work), solid circles (from Vogler et al [52])

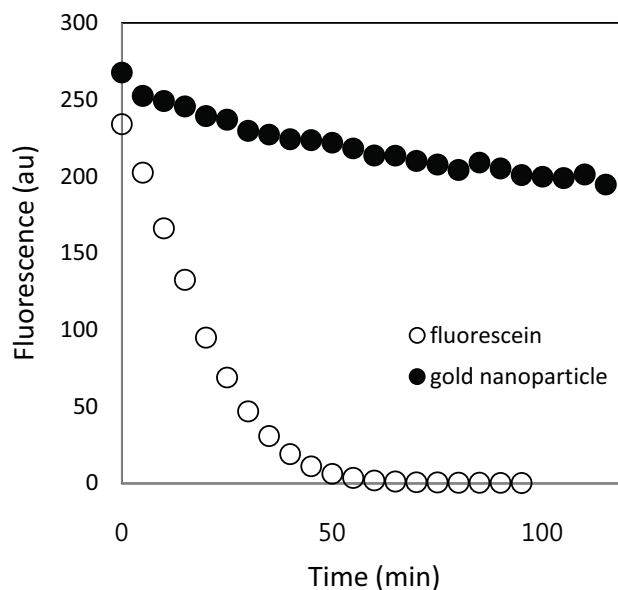


**Figure 2.6.** Photobleaching property of gold nanoparticle solution

The hypothesis is that the gold nanoparticles interact with the LMMCT complexes act as a sensitizer of complex emission. Sensitization of emission by electron rich compounds with correct electronic energy overlap is a well accepted phenomenon [92]. The mechanism by which this takes place can vary and can involve the transfer of electrons from the sensitizer to the emitter before photogradation can take place, thereby increasing emission intensity. This interaction is supported by an excitation spectrum of the emissive product that is higher in energy compared with what has been measured for LMMCT molecular complexes in the absence of gold nanoparticles. Its shape is also skewed, which leads to an energy maximum at  $\sim 290$  nm that happens to correspond to the persistent gold line with the highest intensity listed in Table 2.2).

#### 2.4.3. Effect of chain length on particle size and optical properties

The TEM analysis shows the difference in the obtained particle diameter between the different ligand stabilized gold nanoparticles (Figure 2.7). With shorter chain length, the size of the gold nanoparticle is larger and with longer chain length, the size of the gold nanoparticle is smaller. In the particle size analysis using PhotoShop program with 50 particles per sample, the average diameter of MHA stabilized gold nanoparticle is  $3.3 \pm 0.9$  nm, MOA stabilized gold nanoparticle is  $2.2 \pm 0.6$  nm and MDA stabilized gold nanoparticle is  $1.7 \pm 0.3$  nm.

In the case of MDA stabilized gold nanoparticles, aggregates are visualized in the TEM picture while it is not apparent from the other two sets of gold nanoparticles with shorter chain length. In the case of shorter carbon-chained ligands, it is possible for the aggregates to be separated during the drying process by the interaction with hydrophobic Formvar (poly-(vinyl formal)) coating material of the TEM grid. Formvar is a polymeric surface coating material consisting of  $C_5H_8O_2$  repeating units. This hydrophobic polymer layer would interact with the hydrophobic ligands of the gold nanoparticles. The competing process between the Formvar and surface ligands and between the surface ligands of different nanoparticles can determine whether

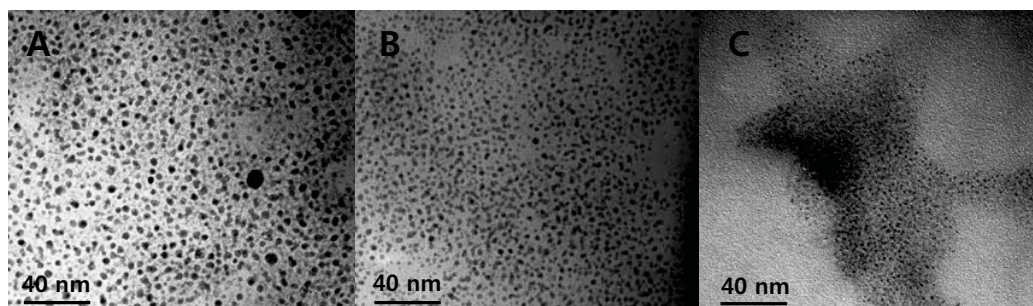


**Figure 2.7.** TEM pictures of different ligand stabilized gold nanoparticles. (A) MHA stabilized, (B) MOA stabilized and (C) MDA stabilized gold nanoparticles.

aggregates form on the TEM grid. In the case of very long hydrophobic ligands like MDA-stabilized gold nanoparticles, strong hydrophobic interaction between each other are not broken apart by the interaction with hydrophobic TEM grid surface.

Changing the chain length of the mercaptoalkanoic acid ligand did not result in a shift in emission wavelength, but did result in both a change of shape and blue-shift of the excitation spectrum maximum to higher energy from  $\sim 4.32\text{eV}$  to  $\sim 4.97\text{eV}$  (Table 2.3, Figure 2.8). Variations in photoluminescence intensity were also noted. In contrast, Huang et al.[62] reported that photoluminescence yield increased with decreasing particle size (from  $2.9 \pm 0.5\text{ nm}$  to  $2.0 \pm 0.2\text{ nm}$ ). The change in particle size was obtained by increasing mercaptoalkane alcohol ligand chain length. Accompanying a change of nearly 1000-fold in intensity was a shift in the emission wavelength to shorter ( $\sim 500\text{ nm}$ ) wavelength as the nanoparticle size was reduced.

**Table 2.3.** Effect of chain length on photoluminescence and particle size (*\*The logP of each uncharged ligand was ranked by Smiles-logP calculator provided by Molinspiration software ([www.molinspiration.com/services/logP.html](http://www.molinspiration.com/services/logP.html)) which uses atom-additive methods as described in Wang et al.[93].*)

Ligands	# of C	Estimated Hydrophobicity (LogP)*	Excit (eV)	Emission (eV)	TEM size (nm)	Stokes shift (eV)
MPA	3	0.2	none	none	Very large	-
MHA	6	1.4	4.32	2.05	$3.3 \pm 0.9$	2.27
MOA	8	2.4	4.36	2.03	$2.2 \pm 0.6$	2.33
MDA	12	4.5	4.97	2.00	$1.7 \pm 0.3$	2.97

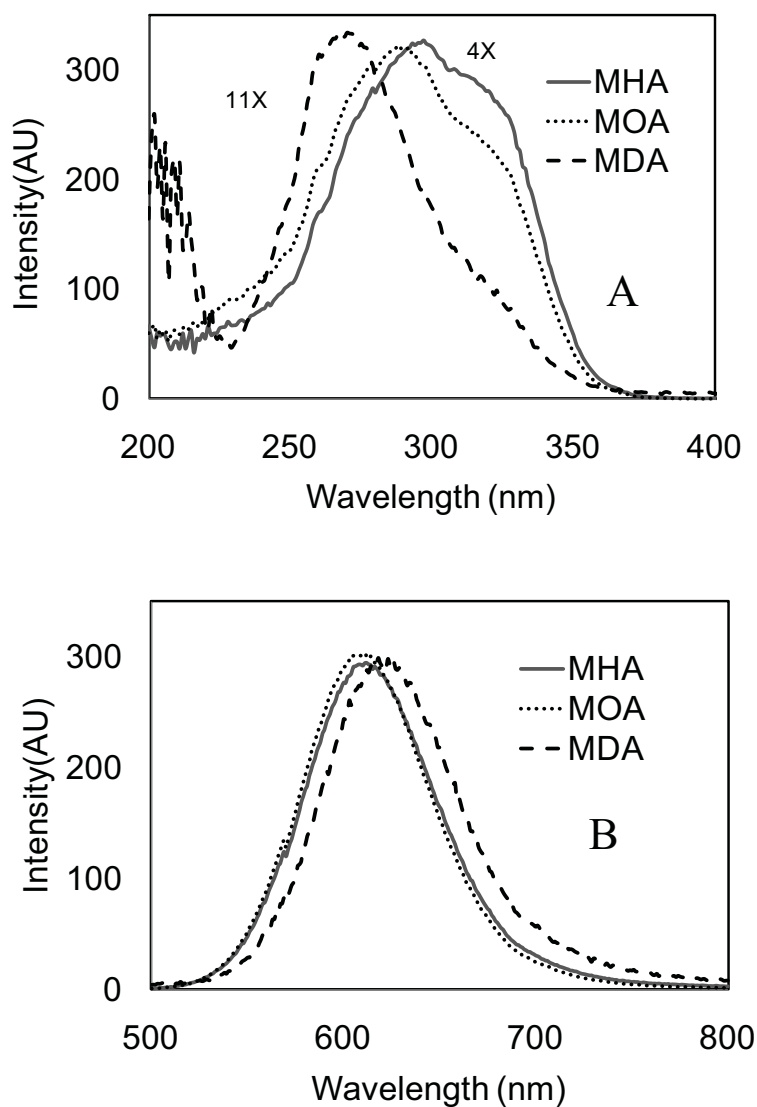


**Figure 2.8.** Excitation and emission spectra of GNP with different ligand. **A)** Excitation spectra obtained for luminescent gold product produced using mercaptododecanoic acid (dotted line), mercaptooctanoic acid (solid line) and mercaptohexanoic acid (dashed line). **B)** Emission spectra obtained for the same samples. Data normalized to highlight shape and position changes. In the excitation spectrum MDA is multiplied by 11, and MOA by 3 relative to MHA. In the emission spectrum MHA is multiplied by 4 and MDA by 11. MOA is unchanged. This means MOA is more efficiently being sensitized.

Although these observations were suggested to be related to size dependent confinement effects, without additional information about the excitation spectrum it is difficult to be conclusive. The limited range of the shift in their emission wavelengths and the fact that all spectra could be obtained using 365 nm excitation energy from a hand-held UV lamp, does not exclude the possibility that photodecomposition of LMMCT complexes into LMCT complexes had taken place in their observation.

When the mercaptoalkanoic acid ligand carbon chain length was changed, there was no significant effect on the emission wavelength but there was a shift the position of the excitation spectrum maximum to higher energy. This shift is caused by changes in the local hydrophobicity at the surface of the gold nanoparticles where the LMMCT site is likely to be located. More discussion of this is provided in Chapter 3.

In general, a greater stabilization of the absorbing state of the CT complex due to dipole-dipole interactions in low hydrophobicity environment should lead to red shift in the excitation spectrum maximum, while less stabilization and a corresponding blue shift should occur in more hydrophobic environments. The longer chain of MDA interacts with the underlying gold core via stronger dispersion forces, and is more likely to have a collapsed configuration (Figure 2.9A), which protects the underlying LMMCT bonds from interaction with the surrounding water, lowering the local polarity. A schematic of this situation is illustrated in Figure 2.9B shows what may happen in the case of shorter chain ligands.

Regardless of the position of the excitation energy maximum there is little change in the emission energy maximum. This observation suggests a significant difference in bonding structure of the triplet ( $^1T^*$ ) LMMCT state relative to that of the singlet ( $^1S^*$ ). Electronic structure calculations for the singlet and triplet excited states of gold-ligand complexes indicate that a major difference between the two is a much

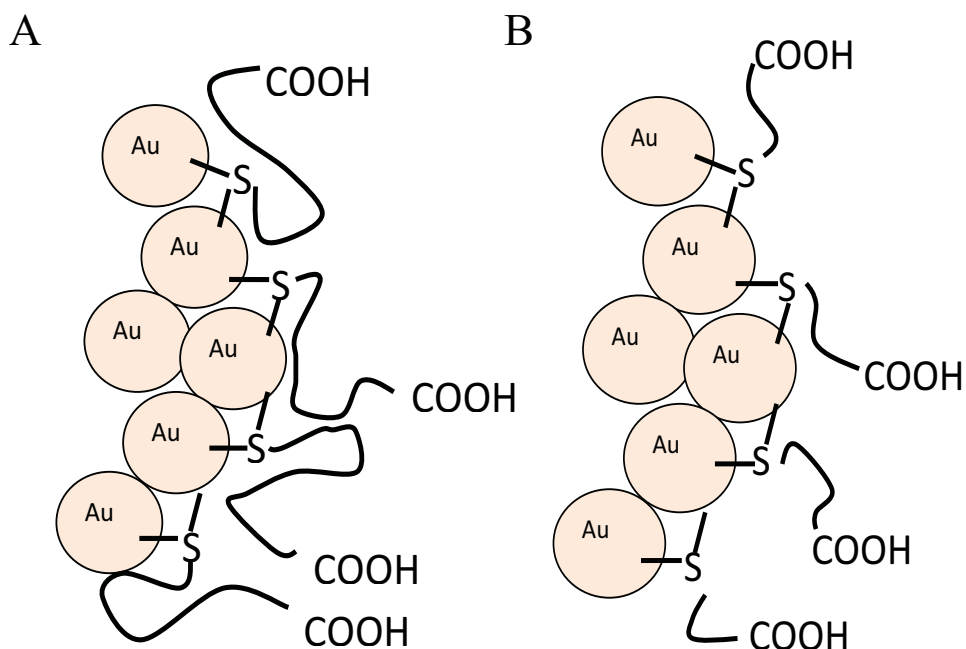


**Figure 2.9.** Cartoon illustrating a hypothetical cutaway configuration of gold-ligand complexes and gold atoms at the surface of gold nanoparticles. Gold atoms comprising the rest of the gold nanoparticle core are not shown in this picture. **A)** Mercaptododecanoic acid, **B)** Mercaptohexanoic acid. The longer chain ligand has greater potential to protect the gold-sulfur bond portion of the molecule from interaction with the surrounding solvent. Under the reaction condition, other gold nanoparticles and gold atoms are only present at the periphery.

shorter Au-Au bond distance of the excited triplet state[91]. This geometry change could be responsible for making the emitting state more compact, and either reducing the overall dipole moment or moving the electronic distribution of the emitting species to a part of the molecule that relatively isolated from the surrounding solvent.

There are differences in photoluminescence intensity when the excitation spectrum maximum shifts, and this matter will be discussed more thoroughly later in

this chapter for the case of varying ligand concentration used during the synthesis, which also had this effect.

Steric hindrance as a function of chain length of the stabilizing agents could be an alternate explanation for different particle size as a function of ligand chain length. Longer carbon chains in a growing cluster could hinder the addition of other gold atoms to the cluster during the synthesis by hindering the formation of Au(0)-Au(0) bonding even under reducing conditions. In this case, ligand chain length should also be inversely related with the final gold nanoparticle size (Table 2.3). Increased hydrophobicity of the longer carbon-chained ligands strengthens the hydrophobic interaction between the ligands, which would attract other ligand molecules from the solution, speeding up the coating. Also, longer carbon-chained ligand molecule would prevent the approach of gold atoms from the solution by steric hindrance. These processes prevent the growth of gold nanoparticles (Figure 2.10).

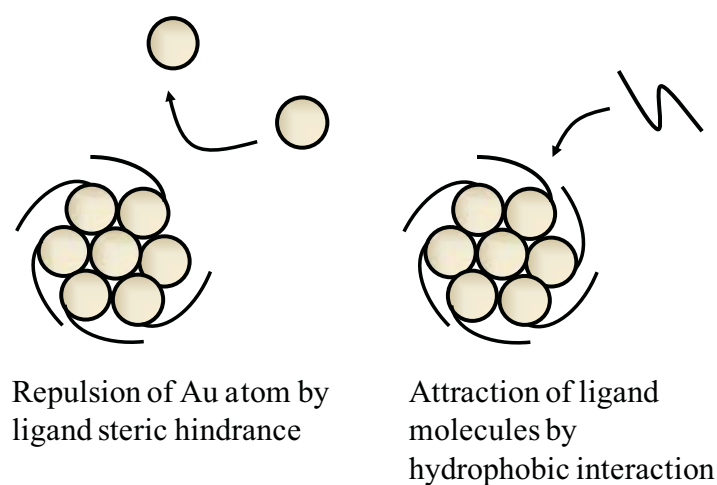


**Figure 2.10.** Scheme describing one of the possible effects of the longer surface carbon chain length on the size of the gold nanoparticles; Due to steric hindrance (Left) and hydrophobic attraction between ligands (Right), the limiting size of gold nanoparticles is smaller when the ligand carbon length is longer.

#### 2.4.4. The effect of the carbon chain length on salt-induced aggregation

Based on the concepts of DLVO theory[94], in the presence of the salt ions ionic screening effects[95] reduce the charge-charge repulsions which makes the particles dispersed. Factors which modulate salt-induced aggregation include the hydrophobicity of the surface-covering ligands[96; 97; 98] and ionic strength which affects the thickness of the double charge layer[95]. If the double charge layer becomes too thin at high salt concentration for the particles to repel each other they will start to aggregate via the dominating van der Waals or hydrophobic interaction.

In the case of alkane thiol-stabilized gold nanoparticles, the length of the alkane thiol carbon chain is the factor for controlling the hydrophobicity of the nanoparticle system. Since the number of the carboxylic acid groups of a ligand is fixed to one per molecule, by changing the carbon chain length of the ligand, the balance between the ionic and hydrophobic interactions can be controlled since the increased number of the carbons in the carbon chain would increase the overall hydrophobicity of the molecules as it is shown in Table 2.3.

The carbon chain length of the ligand plays an important role to determine the concentration of the salt needed to create aggregates. With longer chain length, such as MDA, the particle starts to aggregate even without the addition of salt and forms micrometer-sized aggregates. The hydrophobicity of the longer carbon chained ligand was too strong to make the particles dispersed by the single charge from the carboxylic acid groups at the end of the ligand.

Both MOA and MHA stabilized gold nanoparticles showed more tolerance against salt-induced aggregation. For example, MOA gold nanoparticle showed aggregates forming at higher than 200 mM salt, while MHA did not show any significant aggregation until 300 mM (Figure 2.11).

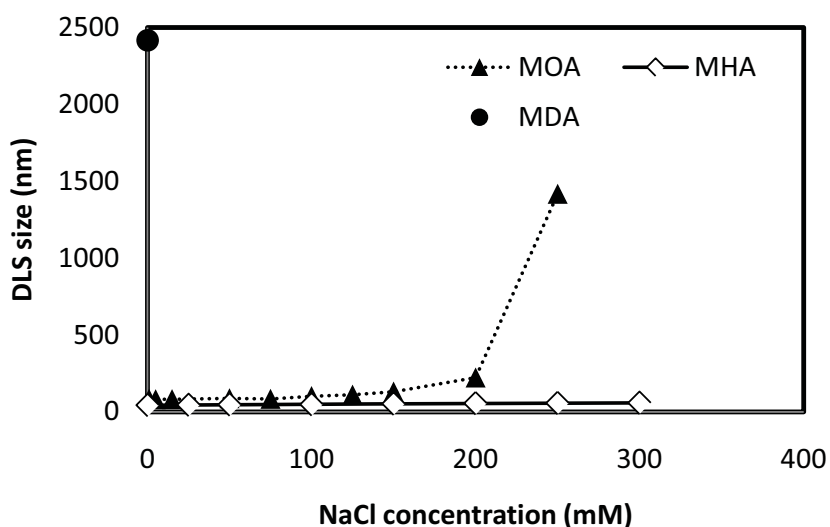


**Figure 2.11.** NaCl induced aggregation of the gold nanoparticles stabilized with MHA, MOA and MDA. The MDA stabilized gold nanoparticles showed large aggregates even without the presence of NaCl. No further salt concentration test has been performed due to the size of the aggregates was out of limit for the reliable reading for the DLS machine.

#### 2.4.5. Salt concentration effects on gold nanoparticles with MPA and MHA ligands

Hybrid gold nanoparticles with different ratios of MHA and MPA were synthesized to control the hydrophobicity of the gold nanoparticles. The MHA to MPA ratios of 9 to 1, 4 to 1, and 1 to 1 were prepared and the salt induced aggregation test was performed (Figure 2.12). The hydrophobicity of each hybrid gold nanoparticles is summarized in Table 2.4. Larger portions of MPA were not successful in making stable gold nanoparticles. MPA may be too short to be utilized as stabilizing agent to protect the gold nanoparticles from uncontrolled aggregation. A more hydrophobic surface resulted in more sensitivity for aggregation in the presence of salt ions. In the case of 9 to 1 and 4 to 1 ratios, hybrid gold nanoparticles,

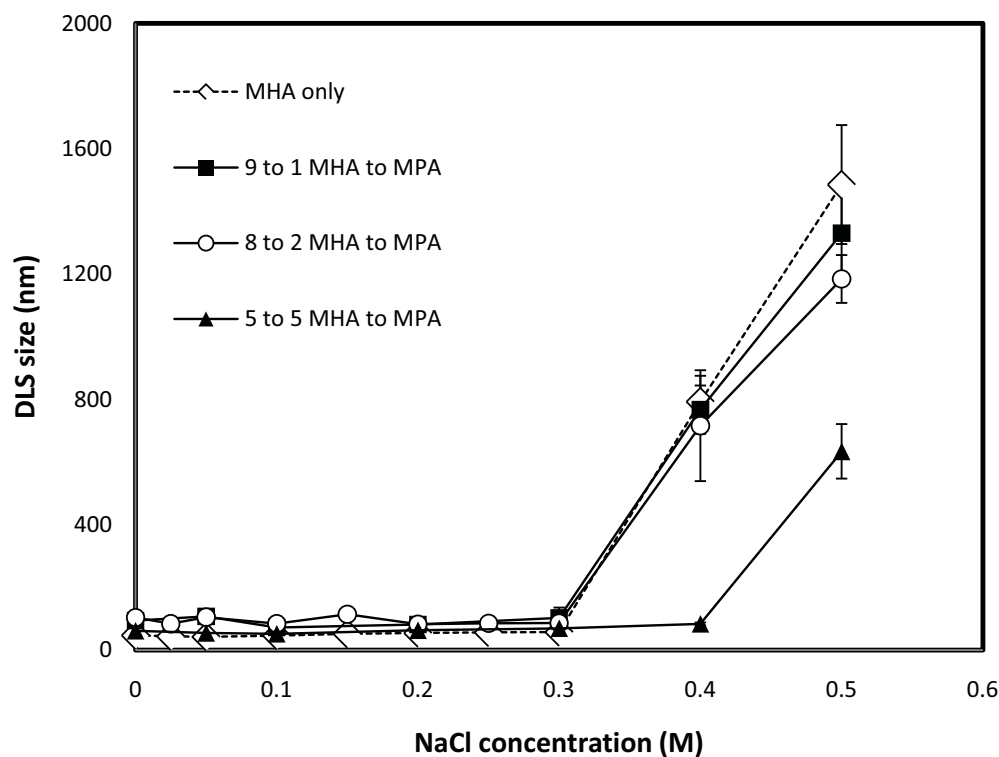


**Figure 2.12.** NaCl induced aggregation of hybrid gold nanoparticles stabilized with different ratios of MHA to MPA (MPA percentages of 0 %, 10 %, 20 % and 50 %).

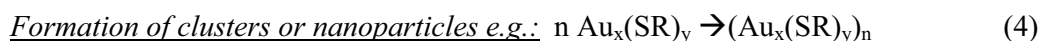
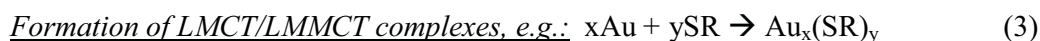
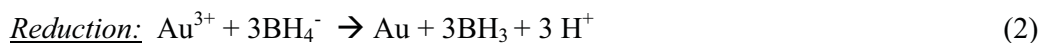
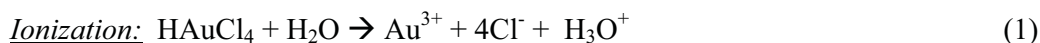
#### 2.4.6. Time dependent spectral changes

**Table 2.4.** Hydrophobicity comparison of the MHA to MPA hybrid gold nanoparticles

MHA to MPA ratio of hybrid GNP	Average number of carbon per stabilizing molecule	Average hydrophobicity per stabilizing agent (LogP3)
MHA only	6	1.4
9:1	5.7	1.28
4:1	5.4	1.16
1:1	4.5	0.8

showed similar aggregation trend as we have monitored from MHA only gold nanoparticles. But at the ratio of 1 to 1 MHA to MPA hybrid gold nanoparticles, showed tolerance against NaCl concentration up to 400 mM concentration.

The basic steps of the reactions involving NaBH<sub>4</sub> driven reduction of gold are reviewed below:



Reaction 2 has been suggested to be a two step reaction involving the reduction of auric salt to aurous salt, followed by a disproportionation step to form two Au(0) [99; 100]. Without the presence of reductant Reactions (2), (3), (4) are not favored.

To understand the reactions taking place in this system further, we monitored the absorbance, excitation and fluorescence spectra of samples periodically within the first 48 hr of reaction. Immediately after mixing of the MOA and NaBH<sub>4</sub> solutions with HAuCl<sub>4</sub>, the characteristic absorption peak of HAuCl<sub>4</sub> at 4.15eV (~300 nm) disappeared (Figure 2.13A).

A broad absorbance at ~3.1 eV (~400 nm) and developed in the first hour of the reaction. After an hour, the absorbance at 400 nm declined, and a peak at ~4.4 eV (280 nm) appeared and continued to grow over the subsequent 48 hr (Figure 2.12B&C). At the same time a new emission at ~2.03 eV (610 nm) appeared and grew in intensity (Figure 2.13D). The time dependence of emission increase at ~2.03 eV is similar to that of nucleation processes reported by Turkevich et al. for citrate gold

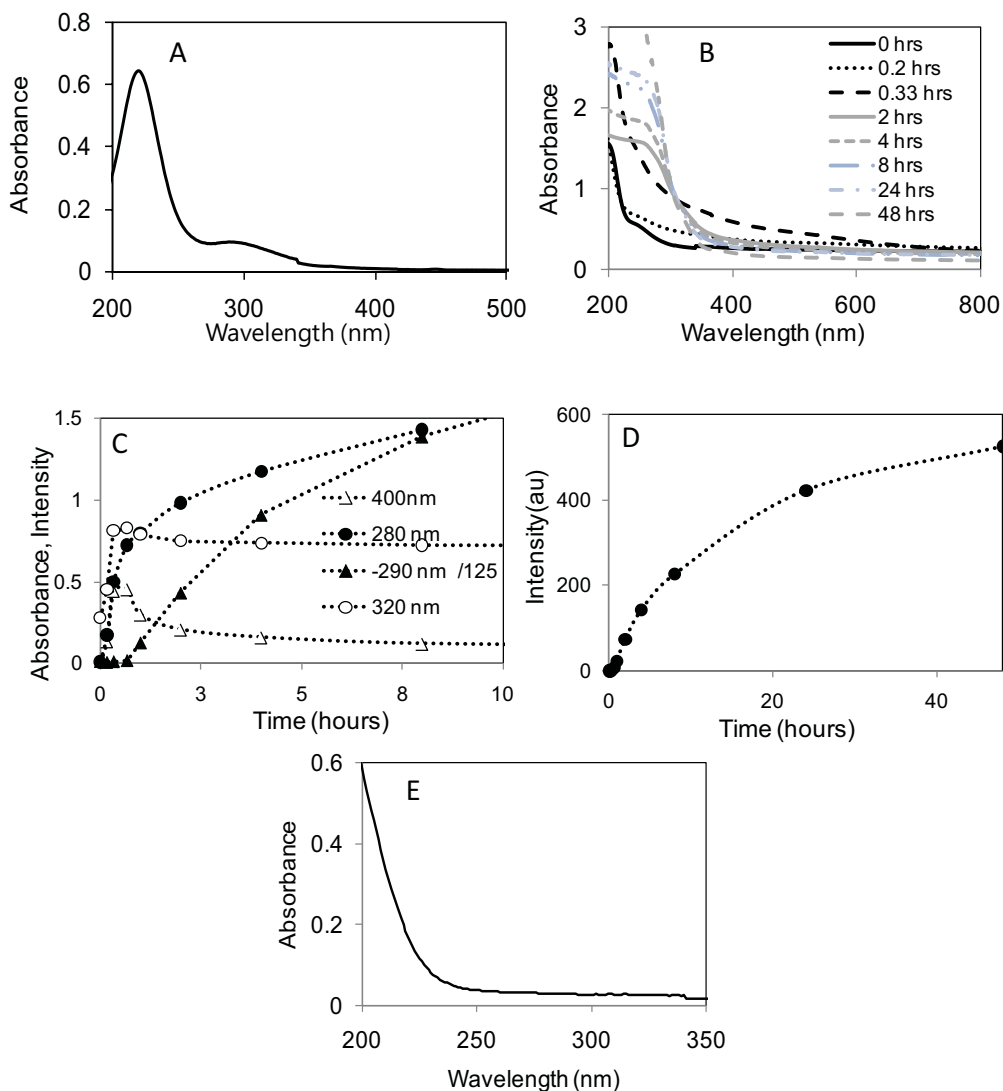


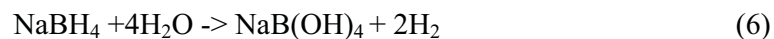
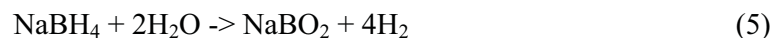
**Figure 2.13.** Spectra and analysis on timed gold nanoparticle synthesis, **A)** Absorption spectra of 50  $\mu\text{M}$   $\text{HAuCl}_4$  solution dissolved in water. **B)** Time dependent change in absorbance as a function of time after reagent mixing. **C)** Comparison of time dependent spectral changes at various wavelengths: absorbance at 400 nm (open triangles), absorbance at 280 nm (solid circles), emission intensity at the excitation spectrum maximum of 290 nm divided by 125 (solid triangles), and absorbance at the isosbestic point of 280 nm. **D)** Time dependence of emission at 610 nm as a function of synthesis time. **E)** Absorption spectrum of final product produced when reductant  $\text{NaBH}_4$  was omitted from the reaction.

[101]. The appearance of an isosbestic point in the UV-Vis absorption spectrum at 320nm (Figure 2.13B) suggests that the photoluminescent product is the result of a two state reaction, that starts with an initially formed nonphotoluminescent material which converts to another photoluminescent product. Eventually most of the initial species is consumed. Reaction (4) is the likely process reflected by the isosbestic point of the UV-Vis absorption spectra. As expected, without added NaBH<sub>4</sub> there is no spectroscopic evidence for Reactions (2), (3) and (4). The absorption spectrum shown in (Figure 2.13E) is taken 48 hr after mixing MOA and HAuCl<sub>4</sub> in water, but without reductant and shows no growth in absorbance at 4.4. eV (~280 nm) and no emergence of photoluminescence at 2.03 eV (~610 nm).

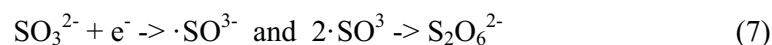
### 2.3.7. Effect of solvent

The solvent in which gold reduction takes place is an important parameter determining the reaction outcome. In water, NaBH<sub>4</sub> forms several products not all of which retain reducing ability [102; 103].

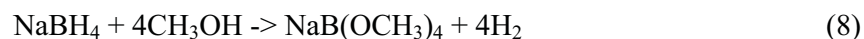
The first product is BH<sub>4</sub><sup>-</sup> formed via Reaction (2). This species is the primary reducing species-the oxidation potential of BH<sub>4</sub><sup>-</sup> is -1.24 eV. Two other competing reactions must be considered, one which forms insoluble sodium metaborate, NaBO<sub>2</sub> (Reaction (5)) and another which forms tetrahydroxyborate, NaB(OH)<sub>4</sub>, a boron oxoanion (Reaction (6)).



NaBO<sub>2</sub> does not directly participate in Au<sup>3+</sup> reduction. Whether NaB(OH)<sub>4</sub><sup>-</sup>, a boron oxoanion could is not clear. In general oxoanions can be 1e<sup>-</sup> or 2e<sup>-</sup> oxidants and tend to have positive electron potentials[104]. However, a few oxoanion species can also act as 1e<sup>-</sup> reductants. One of these is SO<sub>3</sub><sup>2-</sup> which can participate in reactions similar to:



Given that mixing NaBH<sub>4</sub> with water has the potential to form three products, BH<sub>4</sub><sup>-</sup>, NaBO<sub>2</sub>, and NaB(OH)<sub>4</sub><sup>-</sup>, it is clear that *any situation which increases the concentrations of the latter two at the expense of the BH<sub>4</sub><sup>-</sup> concentration at the time of mixing* can affect gold reduction and nanoparticle growth. Factors expected to play a role include pH [103], ethanol content [102], and amount of NaBH<sub>4</sub> initially used. For instance, the formation of sodium metaborate, NaBO<sub>2</sub> is favored in basic solution. Since the pH of the gold-thiol reaction mixture is naturally alkaline ~ 8.5, we can expect this is a significant reaction in our system and is responsible for small amounts of insoluble material formed after mixing. Addition of alcohol to the mixture is known to inhibit the formation of NaBO<sub>2</sub> and instead form alkoxyoxoanions:



As expected in the presence of alcohol no insoluble precipitates are formed at the early stages of the reaction. By blocking Reaction (5), the amount of BH<sub>4</sub><sup>-</sup> available for reaction with gold would be increased, increasing the efficiency of particle nucleation. In conditions where gold is a limiting reagent, this should result in

greater numbers of relatively smaller particles detected by TEM. Consistent with this mechanism, we observed smaller gold particles in the final product when 75 vol% ethanol was used and larger gold particles in the final product with small amounts of ethanol (e.g. 10 vol%).

Comparing in greater detail 75, 25 and 10 vol% EtOH, the average particle sizes were  $1.5 \pm 0.3$  nm,  $1.7 \pm 0.3$  nm, and  $2.2 \pm 0.6$  nm, respectively (n=30) (Figure 2.14). Starting with more NaBH<sub>4</sub> had a similar effect on final product particle size which can be attributed to better nucleation. For example, an initial NaBH<sub>4</sub> concentration of 0.375 mmole produced nanoparticles of smaller dimension,  $1.8 \pm 0.4$  nm (n=50), compared to larger concentrations (0.25 mmol) which produced  $2.2 \pm 0.6$  nm particles (n=50). For very low reductant concentrations, 0.2 mmole and lower, few nanoparticles were produced.

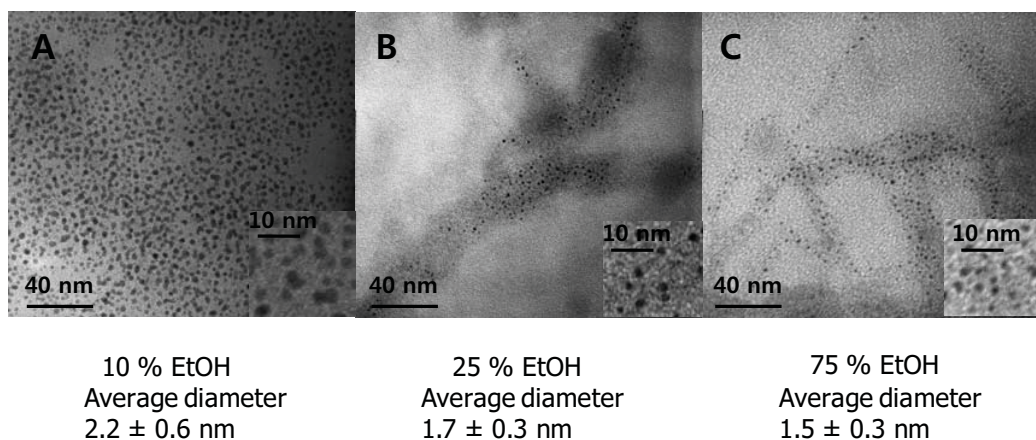


**Figure 2.14.** TEM pictures (360,000X magnification) of the gold nanoparticles synthesized in different solvent ratio of EtOH to water; **A)** 10%, **B)** 25% and **C)** 75% of EtOH to water ratio

#### 2.4.8. Ligand concentration and particle size

The effect of increasing mercaptoalkane carboxylic acid ligand concentration on particle size is shown in Figure 2.15. For the images shown the average particle diameters were  $2.9 \pm 0.8$  nm,  $2.2 \pm 0.6$  nm and  $1.8 \pm 0.3$  nm, for 1.5:1, 3:1, and 5:1 S:Au ratios respectively (n=50). Such a trend might be expected for a nanoparticle capping agent which competes for surface sites on a growing gold nanoparticles [100].

However in Reaction (3) we postulated that the mercaptoalkane carboxylic acids are mainly responsible for the formation of gold-thiol ligand complexes, and in Reaction (4) these complexes retain significant aurophilic attractions which lead to the formation of nanoparticles with associated complexes. In reducing conditions, clustered complexes can form what is essentially a nano-sized reactor environment, not unlike that of dendrimers, but with less complex and organized structure. In this environment gold atoms have a chance to react with permeating reductant to nucleate

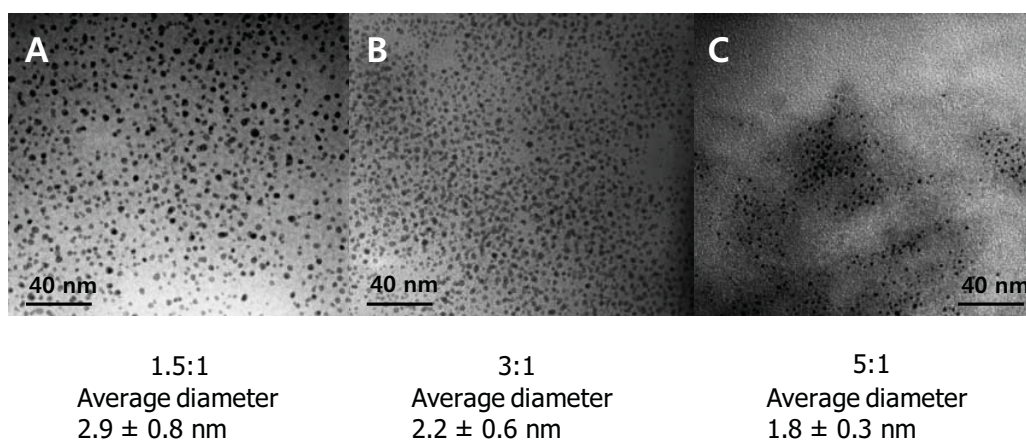


**Figure 2.15.** TEM pictures (360,000X magnification) of the gold nanoparticles synthesized with different thiol to gold ratios; **A)** 1.5:1, **B)** 3:1 and **C)** 5:1 ligand to gold ratio

particles. When the initial ligand concentrations are high enough to react with all the gold atoms a maximum number of ligand complexes are produced, and the number of clusters that nucleate will also be high. If reduction is efficient, each of these clusters has the potential to generate a nanoparticle which will be of relatively smaller dimension, since each cluster will have fewer gold atoms in it. On the other hand if the ligand concentration is limiting, then there is likely to be excess gold atoms that can add to any existing cluster increasing their size given sufficient reducing conditions. Consistent with this, the particle diameter increased with decreasing ligand content with an  $R^2$  of 0.94 (Figure 2.14). It is likely that as the gold atom reduction takes place there is some rearrangement within a cluster, and the ligand then takes on the role of a capping agent to prevent combination of more than one cluster into larger particles. This has been suggested to occur with alkanethiols in organic solution to form core shell structures [105]. The mechanism may be tested in the future using detailed time dependent luminescence and X-ray photoelectron spectroscopy methods but the question is beyond the scope of this current dissertation.

#### 2.4.9. Particle size, excitation spectrum and photo-luminescence

Shown in Figure 2.16 is that the relative quantum yield of photoluminescence decreases with increasing nanoparticle diameter. According to calculations and experiments by Zheng et al. and others, pure gold nanoparticles  $> 2\text{nm}$  in diameter are not expected to be significantly photo-luminescent [106; 107]. We also observe a decrease in photoluminescence with increasing particle size. However, if the origin of the observed luminescence is from nanoparticle-bound LMMCT complexes, these results could be explained by a reduction in total nanoparticle surface area available for LMMCT complex attachment. In other words, the larger the particles, the smaller

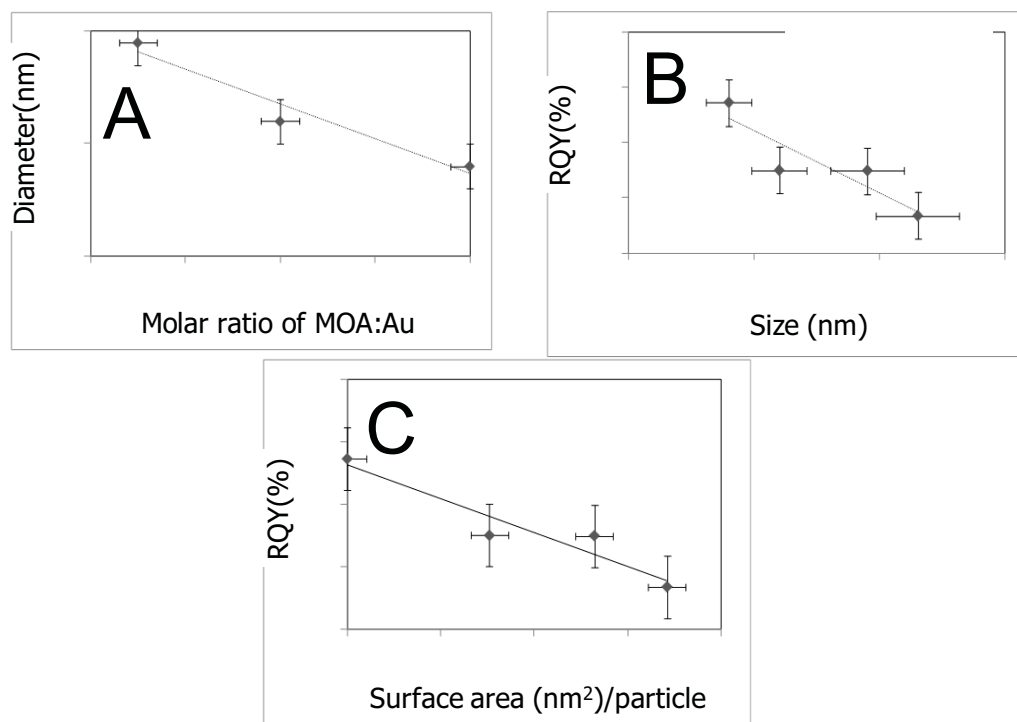


**Figure 2.16.** Particle size analysis, **A)** Diameter of particles as a function molar ratio of MOA to gold, **B)** Relative quantum yield of emission at 610 nm as a function of particle size, **C)** Relative quantum yield as a function of particle surface area.

the overall surface area, the fewer bound ligand complexes. Looking at Figure 2.16B, and considering the change in photoluminescence intensity for a change in particle diameter between 2 and 3 nm we can see that the fractional change in surface area is roughly equal to that of photoluminescence decrease. Specifically, for 2nm diameter the surface area is 12.56 nm<sup>2</sup> and RQY% is 4.5% and for 3nm the surface area is 28.26 nm<sup>2</sup>, and the RQY% is 2, so the ratio of 12.56/28.26 is 0.444 and the ration of 2/4.5 is also 0.444.

It is found that as the particle size decreases, the wavelength or energy maximum of the excitation spectrum changes parabolically (Figure 2.17). However, when normalized by the absorbance at wavelength of the absorbance maximum (Figure 2.18), the obtained relative quantum yield of photoluminescence plotted

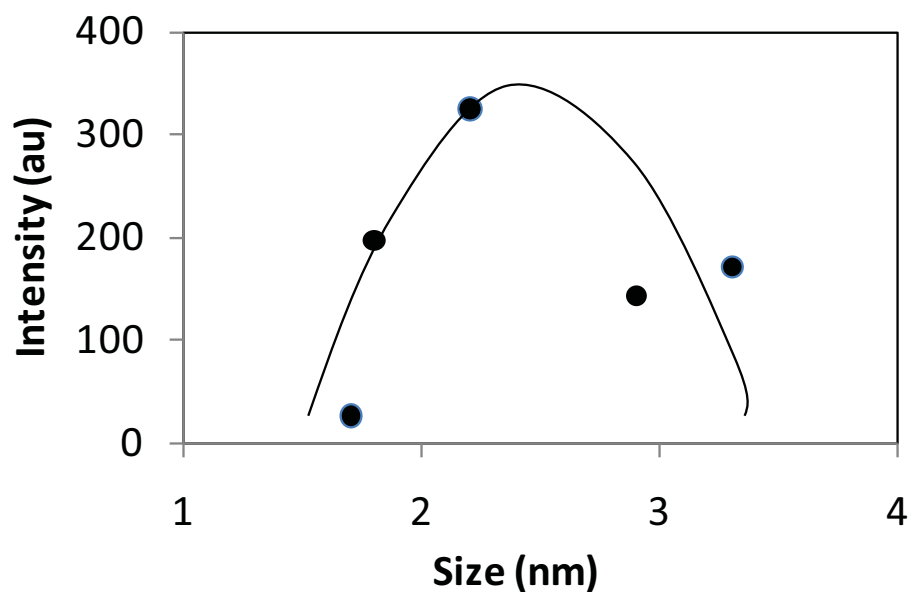


**Figure 2.17.** The size of the gold nanoparticles and its relation with the emission intensity.

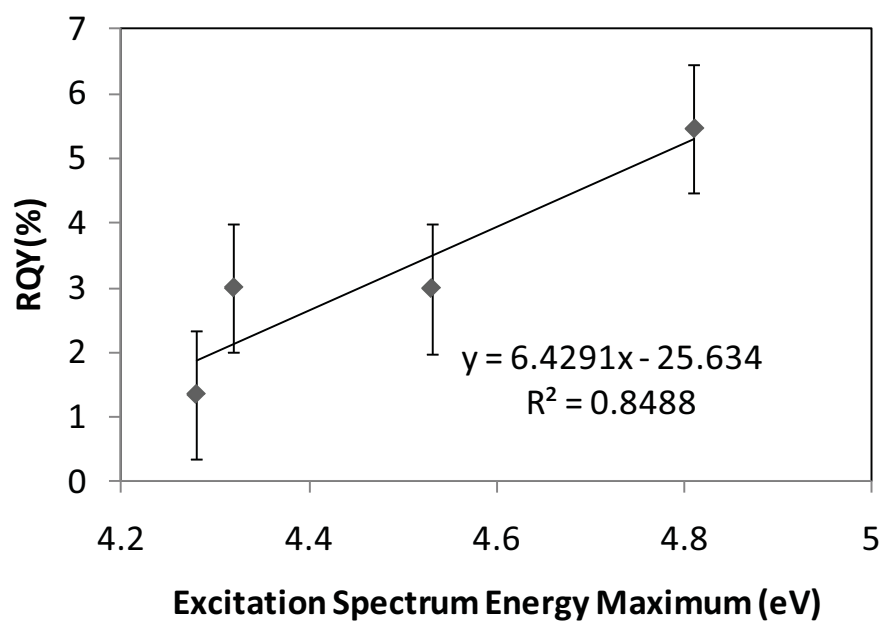


**Figure 2.18.** Excitation spectrum energy maximum and its relation to the relative quantum yield.

against excitation spectrum energy maximum is a linear plot. In other words, higher the photoluminescence yield corresponds to smaller particles, and more blue shift excitation spectrum.

With our model, this trend can be explained if the  $1S^*$  level of the LMMCT is able to move up and down in energy with change in particle size in order to allow better overlap with different levels of neutral and Au(I). As the energy level of the absorbing state moves up in energy, there is greater overlap of the LMMCT complexes with more of the gold levels and this corresponds to an overall increase in the photoluminescence quantum yield. The explanation for why the excitation spectrum energy maximum changes parabolically with particle size is unknown at this time.

#### 2.4.10. Temperature dependence of emission

The fluorescence intensity at 610 nm excited using 280 nm light was found to have a reversible, inverse dependence on temperatures between 1 °C to 35 °C (Figure 2.19). The  $R^2$  value of the slope was 0.9991.

The temperature dependent fluorescence emission behavior of the gold nanoparticles can be used to estimate its energy transfer efficiency. Schulman described the effect of the temperature for the quantum yield of the fluorescence ( $\Phi_f$ )[108] of ZnS/CdSe as following equation,  $\Phi_f = \frac{k_f}{k_f + \Sigma k_d}$ , where  $k_f$  is the rate constant of the fluorescence and  $\Sigma k_d$  is the sum of rate constants of deactivation by all competitive nonradiation processes including heat. An increase in competing processes eventually lowers the efficiency of the overall emission yield resulting less fluorescence.

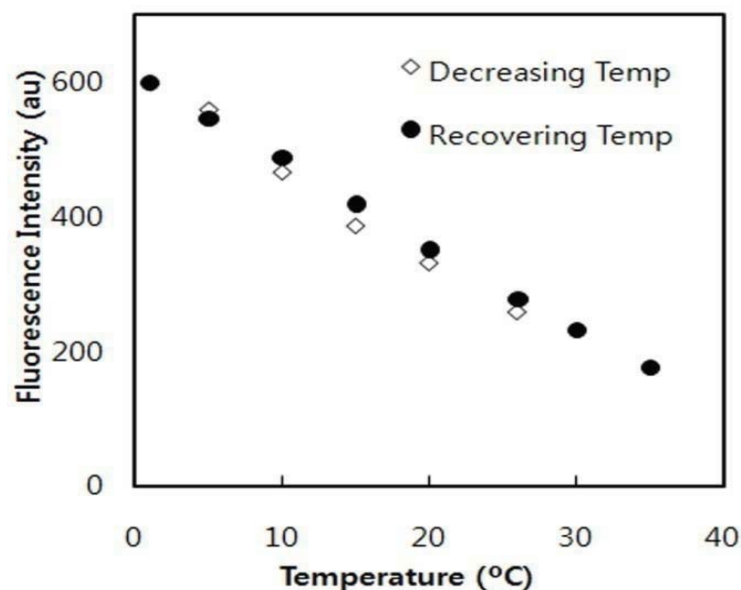


**Figure 2.19.** Temperature dependence of the fluorescence emission intensity at 610 nm measured using 280 nm excitation light. The sample was placed in the temperature-controlled antifreeze bath for 5 min and the fluorescence intensity at 610 nm emission of the sample was read at each temperature point after being transferred within 5 sec to the fluorometer next to the antifreeze bath.

Eychmuller et al. [109] suggested that at higher temperatures, electrons can be deeply trapped in a regional energy gap created by the surrounding heat which allows nonradiative energy release. In earlier work by his group, they showed that electron trapping in CdS quantum dots occurs in  $10^{-13}$  to  $10^{-14}$  sec time, a time with which spontaneous fluorescence process cannot compete [110]. This reservoir of the excited electrons are later detrapped to the conduction band for the spontaneous fluorescence process,  $k_f$ , while some would be released in the form of nonradiative processes,  $\Sigma k_d$ . The electron trap becomes deeper at higher temperatures for those electrons trapped would be more inefficient to overcome the energy gap to reach conduction band.

Decreased fluorescence emission intensity with increased temperature was seen in the case of quantum dots (CdSe/ZnS core/shell), with and without an accompanying change in emission peak position [111; 112].

Liu et al. argued that the dependency of the fluorescence emission intensity on the temperature is related with changes in the quantum yield of the materials [111]. In their work, they showed that a decrease in fluorescence intensity with temperature could be correlated to particles which possessed a lower effective quantum yield. For example, a 50% decrease of the fluorescence emission was observed with 15 K temperature increase (280 K to 295 K) for the quantum dots with 9.8% relative quantum yield, while 35.6 K temperature increase (280 K to 315.6 K) was needed for the same fluorescence emission intensity decrease for quantum dots with 22.4% relative quantum yield. These relative quantum yields are referenced to Rhodamine 6G fluorescent dye molecule solution (QY = 0.95). For our gold nanoparticles, there is a linear dependence of the fluorescence intensity on temperature and it required an increase of 24.7 K (280 K to 304.7 K) for 50% decrease of the fluorescence emission intensity.

#### 2.4.11. Cytotoxicity test

Understanding biological mechanisms is often a challenging task due to the complexity of the biomolecular interactions and low concentration of molecules of interest. Most biomolecules lack the characteristics to distinguish themselves from surrounding objects during the observation. Fluorescent probes are widely utilized as bio-imaging agents due to their sensitivity, noninvasive nature, safe detection and simple usage over other technologies including MRI or radioisotope labeling [6]. Fluorescent dye molecules such as fluorescein have been widely used due to its

brightness and sensitivity accounted by its superior quantum yields (0.95) [1]. However, a lower photobleaching threshold has been a major drawback making them not suitable for elongated monitoring and analysis. Recently, quantum dots are utilized as fluorescent probes mainly due to their more stable photobleaching properties [15; 17; 18; 113]. However quantum dots are composed with biologically active heavy metals, such as cadmium, and their cytotoxicity limits biological usage as they are known to release toxic metal ions to surrounding environments [20].

Gold has been widely used as a biomaterial for implant in medicine and dentistry [114]. Also, Connor et al showed no acute inflammatory reaction caused by negatively-charged gold nanoparticles uptaken in human body [26]. They tested various capping molecules including citrate, cysteine, glucose and CTAB and showed no toxicity even though they are uptaken by cells. Positively charged nanoparticles fare worse. Goodman et al. reported cytotoxicity for 2 nm gold nanoparticles presenting a positively charged surface while anionic gold nanoparticle showed little cytotoxicity [115]. An *in vivo* study conducted by Harper et al. using zebra fish also showed 100% mortality at 250 ppm concentration range for 1.5 and 0.8 nm cationic gold nanoparticles while anionic and neutral gold nanoparticle showed less than 20 % of mortality [116].

Gold nanoparticles did not cause any death of BEAS-2B cells up to a particle concentration dose of 1  $\mu\text{M}$  (Figure 2.20). The highest concentration of 1  $\mu\text{M}$ , showed 57% increased cell viability comparing to the control. The increase of apparent viability at 1  $\mu\text{M}$  concentration compared to the control may be an indication that at these levels the cells are beginning to feel some stress. The high concentration of gold nanoparticles irritates the cell's metabolic system so that the cells actually produce more dehydrogenases at these conditions. This upregulation of active dehydrogenase

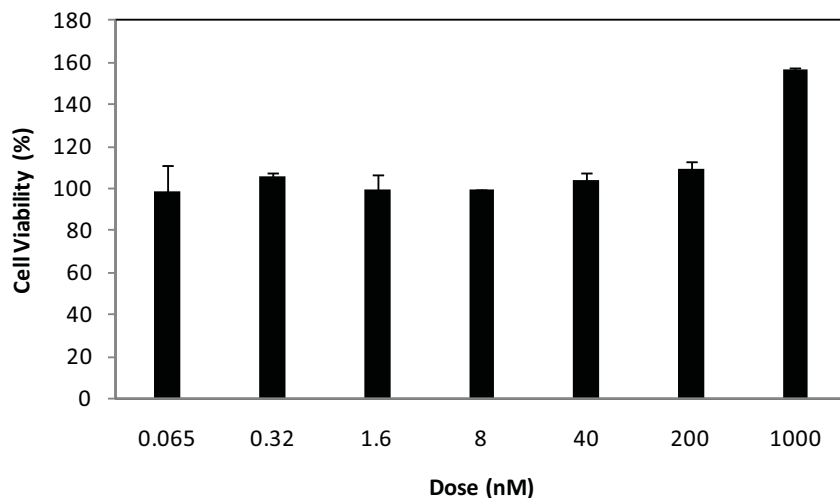


**Figure 2.20.** Beas-2B cell viability versus dose of gold nanoparticles

in the live cells is responsible for the direct conversion of the tetrazolium assay reagent which leads to higher than baseline level of 460 nm absorbance. For future cytotoxicity tests, assuming that an eventual application of these materials may be IV injection into humans, should include macrophages, liver and kidney cell evaluations.

### 2.5. Conclusions

A goal of this work was to understand the details of the reductive reaction of  $\text{HAuCl}_4$  and mercaptoalkanoic acids at RT in  $\text{H}_2\text{O}$  as a function of reaction condition, ligand chain length, and solvent concentration. Reports of synthesis in other solvent systems have shown variability in results in terms of photoluminescence yield, emission wavelength and the coproduction of other materials. Confounding the problem is the potential for reductants such as  $\text{NaBH}_4$  to react with water to form other products that cannot participate in gold reduction. The importance of this competing reaction is discussed in this study. In water the reductive reaction of  $\text{HAuCl}_4$  and mercaptoalkanoic acids synthesis reaction forms nanoparticle-stabilized

photo-luminescent ligand complexes of LMMCT character and which are stable against UV irradiation with relatively high photoluminescence yields. No free ligand complexes were detected using electrophoresis, further suggesting the gold-thiol ligand complexes formed are strongly interacting with gold nanoparticles. The excitation spectrum revealed the interaction of both neutral and single ionized gold atoms with the ligand complexes. These interactions are likely responsible for enhanced stability of these complexes compared with those produced as free molecules via other synthesis methods.

It was found that there are two stages to the production of photoluminescence: an initial phase in which absorption spectral characteristics typical of reported gold-thiol ligand complexes with little photoluminescence grow in magnitude over the course of the first hour, and a second step in which a photoluminescence consistent with LMMCT complexes is greatly amplified along with the appearance of gold nanoparticles. Isosbestic features in the time dependent spectra taken during the first 48 hrs of reaction showed that the intense emission was produced as the terminal product of a two state reaction that likely involves the continued reduction of gold-thiol ligand complexes into nanoparticles. Nanoparticle size was adjustable by altering specific reaction parameters: the chain length and amount of ligand, and the amount of  $\text{NaBH}_4$ , but in contrast to previous work by other researchers no effects on the emission wavelength were noted. Nanoparticle size did affect the photoluminescence yield and the energy maximum of the excitation spectrum. This suggests that the terminal state is always the same, but the overlap between the metal and the ligand complex is changing with nanoparticle size. Changes in chain length of the ligand had dual effects of changing particle size as well as local hydrophobicity of the emitting species. Both the energy level of the absorbing LMMCT species, and the

electronic overlap between the CT complex and the gold atoms was affected. Changes in MOA ligand concentration used in the synthesis also affected particle size and excitation spectrum energy maximum in a way that suggests particle size alters the binding of the LMMCT complexes to the particles and possibly the structure of the particles themselves. The hydrophobicity of the ligands was calculated by LogP3 values. Longer chain ligands with more hydrophobicity had less tolerance against salt-induced aggregation. Two nanometer diameter is considered to be a transition between ordinary nanoparticles and quantum-enhanced particles. Although further study is needed to better understand the nature of the particles in this transitional size range, the relative purity and robustness of the materials produced suggests their practical potential in applications such as two photon imaging or bioelectronics will be possible using these particles. Gold nanoparticle products did not show cytotoxicity with BEAS-2B cells which may indicate the applications for the product can be expanded into biological and medical fields. To demonstrate targetability, the gold nanoparticles were conjugated with folate molecules and uptaken to the folate-positive breast cancer cell line, MCF-7, was monitored. As a negative control, the gold nanoparticles were incubated with the folate-negative human lung cancer cell line, A549, and showed no binding for the gold nanoparticles (Figure 2.21).

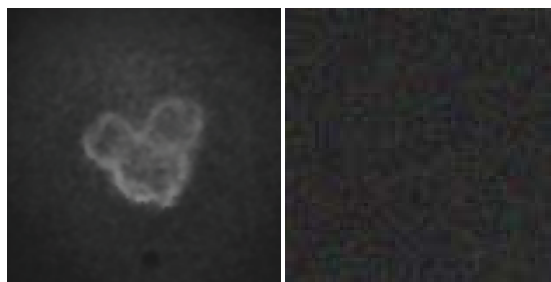


**Figure 2.21.** The fluorescence microscopic image of MCF7 cells (left) and A549 cells (right) after incubating with folate-conjugated gold nanoparticles for 6 hr (50X).

## CHAPTER 3

### PH DEPENDENT EMISSION PROPERTIES OF MERCAPTOOCTANOIC ACID TERMINATED GOLD NANOPARTICLES

#### 3.1. Abstract

In this chapter, we describe the synthesis and properties of a pH responsive nanoparticle-supported molecular brush which utilizes the polarity-dependent photoluminescent signal of gold-thiol charge transfer complexes to report the pH change. This work shows that bifunctional molecular ligands in which one of the functional groups is protonatable while the other forms a stable bond with the gold nanoparticles can form a collapsible molecular brush on the surface of gold nanoparticles. By using a thiol-based ligand a polarity sensitive photoluminescent charge transfer complex can be localized at the particle periphery. When the brush is collapsed this species responds reversibly to the change in local polarity. The operational range of these materials is between pH 5 and 8, spanning the range of pH that are generally relevant in chemical and biological studies. The typical size of this material is about 2 nm, small enough for use in nanosized devices and intracellularly.

The Lippert-Mataga analysis was performed to show the expected linear dependence between the solvent polarity and change in dipole moment between ground state and excited state. The slope of this curve indicated the excited state is more polar than the absorbing ground state, and so it more affected by local

environment. The Grahame model was used to estimate the number of charges per particle.

### 3.2. Introduction

Recently developed nanotechnologies enabled the development of various types of nanoparticles [117; 118; 119; 120; 121]. These nanoparticles are useful for the biochemical analysis including bio-sensors or bio-markers [122; 123; 124]. Since the measurement of pH is one of the most important indications for agricultural, chemical, industrial, diagnostic and biological applications. The pH sensor is one of the mostly studied types of nano-sensors [40; 124; 125]. Many of the nanoparticles designed for the pH sensors utilize pH indicating molecules encapsulated in nano-shells or covalently attached on the surface of the nanoparticles.

To be distinctively differentiated from the background in the nanometer scale, a fluorescent indicator preferred over color changing indicators. Commercially available pH sensitive commercial dye molecules [126; 127; 128; 129; 130] such as 2,7-Bis-(2-carboxyethyl)-5-(and-6)carboxyfluorescein and green fluorescent protein [126; 127; 131] are adopted for their sensitivity, size and relative safety in biological environments [132; 133; 134; 135; 136]. However, most of these have aromatic macrocycles [1; 132; 133; 135] and can be susceptible to photobleaching and biochemical reactions. Leakage of dye from the carrier is another concern for this type of the nano-pH sensors. A nanoparticle with pH indicating ability but without fluorescent dyes would be more desirable. Quantum dots overcome many of the problems of fluorescent dye molecules [15; 18], but have no intrinsic pH dependent change unless pH responsive dyes can be conjugated on the surface [125; 137]. However, cytotoxicity concerns continue to drive the search for improved sensors [20;

22; 23]. A potential solution to the problems are water-soluble, nontoxic pH-sensitive photo-luminescent gold nanoparticles. Gold nanoparticles have been utilized in many biological applications in nanobiotechnology areas including nanoimmunology and nanomedicine due to their perceived biocompatibility, noncytotoxicity and nonimmunogenicity [26; 138; 139]. Their optical properties have been of interest for various applications including photonics [140], biomaterials [141] and bio-imaging agents [31; 72]. However, only a few studies have been reported for the pH sensitive gold nanomaterials. These involve pH sensitive surface plasma resonance (SPR) changes when the particle size, shape or surface is altered [142; 143; 144; 145; 146], and colorimetric responses which measure the aggregation-induced changes to the integrated extinction between 600 and 800 nm or SERS signals [40; 42; 147; 148; 149]. A fluorescent gold-based pH sensor embedded in a polythiophene polymer matrix was reported but with significant polydispersity and limited range of detectable pH, in outside of biological region of pH 3 to pH 6 [150].

The goal of this study was to use molecular brush technology to design a gold nanoparticle-based photo-luminescent pH sensor that works in the range of pH 5 to pH 8. Molecular brushes are an emerging technology aimed at smart, switchable, and multifunctional surfaces. Application areas include coatings that control wetting, adhesion, friction, or the emission of light [151]. In this case the brush consists of short mercaptooctanoic acid (MOA) molecules which on binding to the gold nanoparticles generates a photoluminescent charge transfer complex at the nanoparticle metal/ligand interface [47; 54; 56; 61; 66; 70]. The singlet excited state of the charge transfer (CT) complex is polarity sensitive and exhibits a characteristic change in its excitation spectrum and photoluminescence intensity when the surrounding polarity drops. Deprotonation of the carboxylic acid group of MOA

causes a collapse of the molecules onto the nanoparticle surface. This obscures the emitting part of the molecule from the polar surroundings and induces a polarity-consistent change in position and shape of the excitation spectrum and change in emission intensity. The pH response of this system between pH 5 and 8 was found to be reversible with no aggregation of suspended materials.

### 3.3. Materials and methods

#### 3.3.1. Materials

Mercaptooctanoic acid ( $C_8H_{16}O_2S$ ), hydrogen tetrachloroaurate ( $HAuCl_4$ ), sodium borohydrate ( $NaBH_4$ ) were purchased from Sigma (St. Louis, MO). E-Pure filtered water (18 M $\Omega$ ) (Barnstead, Thermo Scientific, Waltham, MA) was used for all syntheses. Dialysis membranes (1000 MWCO) were obtained from SpectraPor (Rancho Dominguez, CA) and rinsed in E-Pure water before use. Formvar-coated carbon TEM grids were obtained from Ted Pella (Redding, CA). Two hundred nanometer pore size GD/X syringe filter was purchased from Whatman (Kent, UK) and 100 nm pore size Acrodisc syringe filters were purchased from Pall Corporation (East Hills, NY).

#### 3.3.2. Gold nanoparticle synthesis

Gold nanoparticles were synthesized by adding 12.8  $\mu$ L of mercaptooctanoic acid (0.075 mmole) in 0.45 mL of ethanol into 2.30 mL of stirring 0.01087 M gold chloride solution (0.025 mmole) in water in a 25 mL Erlenmeyer flask using 1.5 cm stir bar spun at 600rpm using a magnetic stirrer. Ten sec after the mercaptooctanoic acid addition, 1.75 mL of 0.143M sodium borohydride (0.25 mmole) were added and the mixture stirred overnight at room temperature at 600 rpm. Parafilm was used to

seal the top of flask to prevent evaporation. The next day, sample was separated into three 1.5 mL centrifuge tubes and centrifuged at 12000 rpm using bench-top centrifuge (Micromax RF, Thermo Scientific) for 10 min at 25 °C. The supernatant was triturated with 200-proof EtOH leaving the product pellet to dry. The dried pellet was weighed and the final yield of the synthesis was determined to be  $37.1 \pm 2.7\%$ . The pellet was resuspended in E-pure water to obtain the concentration of 0.2 mg/mL.

### 3.3.3. Transmission electron microscopy

Transmission electron microscopy images were obtained using a JSM840a TEM (JEOL, Tokyo, Japan) at the Electron Microscopy facility at Brigham Young University, Provo, UT and Tecnai T12 TEM (Philips, Andover, MA) operated at 120 kV with the magnification of 666,667 X for observation from the Heath Science Core Facility in the University of Utah. A 5  $\mu$ L drop of gold nanoparticle solution was allowed to air-dry on the center of the TEM grid at room temperature.

### 3.3.4. Fluorescence and absorption spectrometry

Absorption spectra of the gold nanoparticle suspensions containing 1  $\mu$ M of particles at pH 8.5 and pH 3 were recorded between 200-800 nm at room temperature, using a Shimadzu UV mini 1240 (Kyoto, Japan) absorption spectrophotometer, in 1 cm path length quartz cuvettes at 20 °C. Spectrometer resolution was  $\pm 2$  nm. Fluorescence emission spectra of gold nanoparticle suspensions containing 1  $\mu$ M of gold particles were obtained from 400 nm to 800 nm at 20 °C using a Cary Eclipse spectrophotometer from Varian (Palo Alto, CA). An excitation wavelength of 290 nm was used. Samples were placed in a 1 cm quartz Suprasil cuvettes, and spectrometer slit width was fixed to 5 nm to obtain a spectral resolution of 1 nm. The excitation

spectra monitoring 610 nm emission as a function of excitation wavelength between 200 and 600 nm were taken using the same instrument.

### 3.3.5. Dynamic light scattering (DLS) and Zeta-potential

Particle size distributions and zeta-potentials were obtained using a Malvern Zetasizer NanoZS (Worcestershire, UK) in 1 cm quartz cuvettes at 20 °C. Typical polydispersity of the samples was between 0.4- 0.6. The number of scans to be averaged was determined automatically by the machine depending on the output quality and was usually in the range of 12 – 17.

To exclude the possibility that the loss of emission at lower pH was due to only to precipitation, the gold nanoparticle solutions (prepared at a particle concentration of 1  $\mu$ M and pH 8.5) were mixed with NaCl to contain 0, 5, 15, 25, 50, 75, 100, 150, 200, and 250mM of NaCl. The fluorescence emission was measured at each NaCl concentration

### 3.3.6. pH and NaCl dependent measurements

This experimental set was designed for determining the effect of pH and NaCl concentration on the gold nanoparticle's optical properties. For pH dependent spectroscopic measurements 3 mL of triturated and resuspended gold nanoparticles synthesized by the process described containing 1  $\mu$ M gold nanoparticles was adjusted to specific pH using either 1 M HCl solution or 1M NaOH solutions. The pH was measured using AR60 pH meter (Fisher Scientific, Pittsburgh, PA). At each pH increment, the sample was characterized by measuring the emission intensity, absorbance, and DLS. This procedure was repeated several times with the same specimen to ascertain repeatability and the emission and absorbance spectra were

corrected for dilution of the sample accordingly. For NaCl concentration effect on gold nanoparticle's optical properties, 1 M NaCl solution was added into the gold nanoparticle solution up to NaCl concentration of 100 mM. All the measurement described above repeated. The excitation spectra with 610 nm emission were measured as a function of pH.

### 3.4. Results

#### 3.4.1. Transmission electron microscopy

The TEM analysis was performed for both high and low pHs at pH 8.5 and pH 3.0 (Figure 3.1). After counting 50 particles for each specimen, gold nanoparticles at higher pH up to 8.5 were found to have an average particle diameter of  $2.2 \pm 0.6$  nm and the particles at lower pH around 3.0 had an average particle diameter at  $2.3 \pm 0.5$  nm. There is basically no difference between the TEM images of gold nanoparticles at higher and lower pH (Figure 3.1).

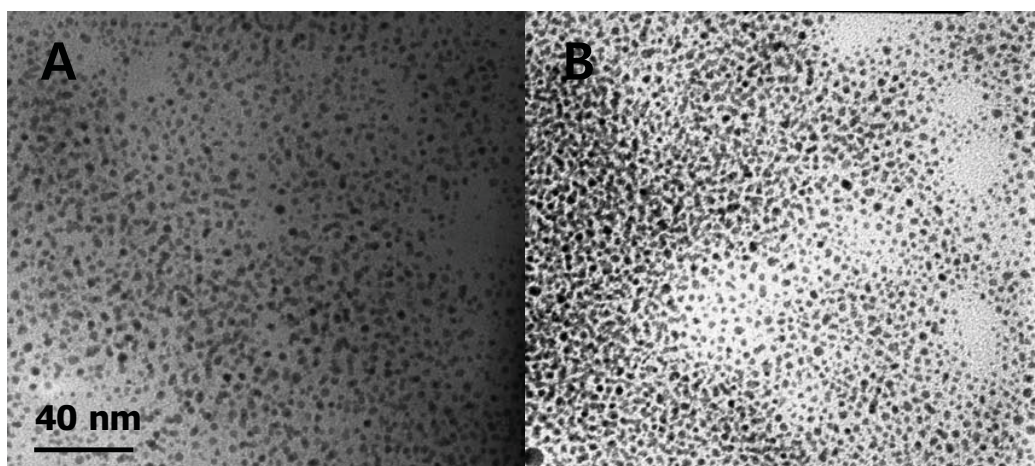


**Figure 3.1.** Transmission electron microscope image of fluorescent gold nanoparticles, A) at pH 8.5 and B) at pH 3.

#### 3.4.2. Emission and absorption measurements

When placed onto a UV transilluminator with excitation wavelength 254 nm, the as-synthesized materials at pH 8.5 produced a bright red emission with a maximum near 610 nm (Figure 3.2).

The pH dependence of the emission, excitation and absorption spectra as a function of pH were measured (Figure 3.3). The peak intensity at 610 nm emission (Figure 3.3A) declined approximately 3- fold as the pH was changed from pH 9 to pH 6. The change is not sigmoidal and there is a 60% rise in emission intensity between pH 6.0 and 3.9 (Figure 3.3B). The change in emission intensity as a function of pH was found to be reversible between pH 9 and 5 (Figure 3.4). At pH below 4.5 increasingly irreversible aggregation was observed. Excitation spectra measured with 610 nm emission as a function of pH are shown in Figure 3.2C. The excitation peak position showed a sudden shift from 280-290 nm range to 250-260 nm range at pH around 5 (Figure 3.3D). A sudden change in the absorption spectrum took place around pH 5 as well. Absorbance spectra were measured as a function of pH. The



**Figure 3.2.** Red-emitting gold nanoparticle solutions on the UV transilluminator (excitation 254 nm)

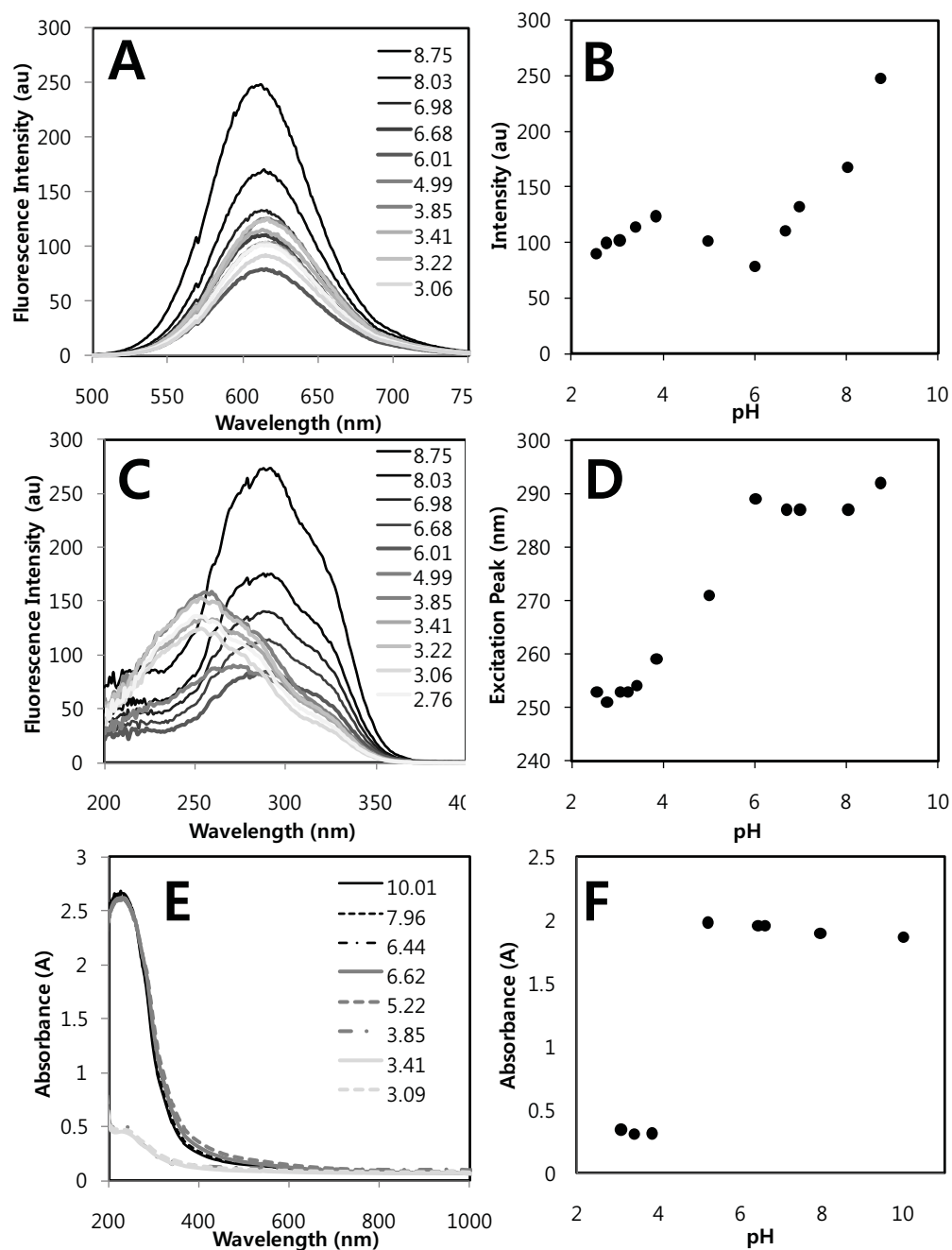


**Figure 3.3.** Gold nanoparticle optical spectra at different pH, A) Emission spectra of fluorescence gold nanoparticles with the peak excitation for each point as a function of pH, B) Emission peak intensity change as a function of pH, C) Excitation spectra with 610 nm emission as a function of pH, D) Excitation peak change as a function of pH, E) Absorbance spectra change as a function of pH and F) Absorbance at 280 nm plotted as a function of pH.

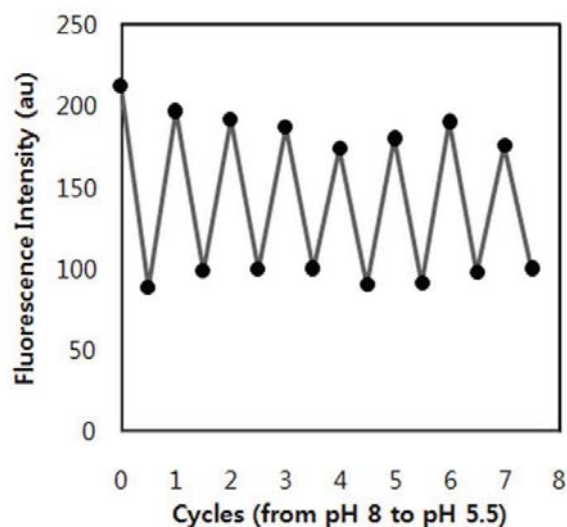


**Figure 3.4.** Reversibility of fluorescence intensity as a function of pH.

result showed that between pH 6 to pH 5 a definite shift in the position of the excitation peak maximum occurred (Figure 3.3E and F).

The fluorescence intensity of gold nanoparticles measured at different pH conditions was shown to be correlated with the pH. The emission intensity of gold nanoparticles excited with each pH point's excitation peak decreased from higher pH down to pH 6 and then recovered slightly (Figure 3.3B). However, when the emission intensity was normalized by the absorbance at the absorption wavelength maximum, the normalized emission intensity displayed a typical sigmoidal dependence of a titration curve (Figure 3.5).

#### 3.4.3. DLS size and Zeta potential versus pH

The DLS size distribution of the gold nanoparticle suspension increased from 70~80 nm at high pH to more than 1  $\mu\text{m}$  range as the pH decreased. This was due to the enhanced hydrophobic interaction between the octane backbones of mercaptooctanoic acid surface capping molecules between neighboring nanoparticles

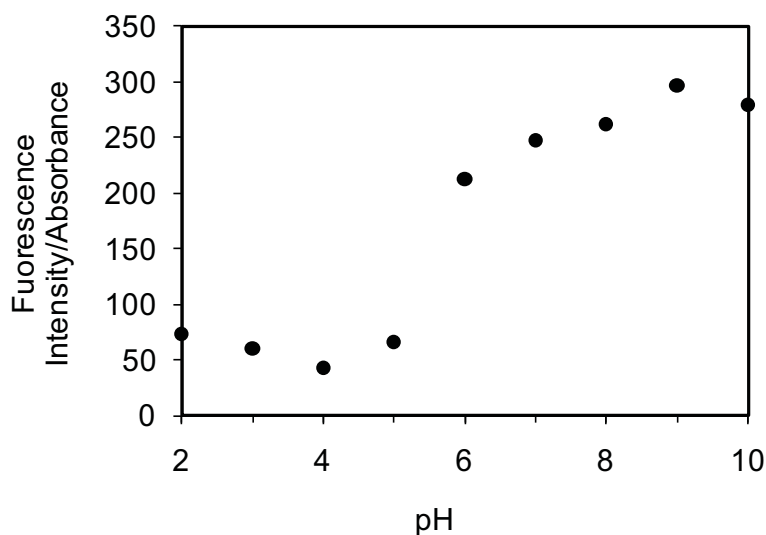


**Figure 3.5.** Normalized emission intensity at different pH

at low pH where the surface charge is low. The size of the aggregation dramatically increased near the isoelectric point of pH 5.5 and the exact size at pH lower than the isoelectric point was not accurately measurable by the DLS machine (Figure 3.6A). Consistent with the observed aggregations, the zeta potential of the particle suspension between pH 9 and pH 4 declined from  $-35$  mV to  $-5$  mV (Figure 3.6B), becoming essentially zero at more acidic pH values. At low pH where the particle surface charge is reduced the van der Waals interaction of essentially uncharged gold nanoparticles dominates.

The isoelectric point of the sample was calculated as 5.5 from zeta-potential analysis using Henderson-Hasselbalch equation [152], where the molecules are half neutralized,  $\frac{[A^-]}{[HA]} = 1$ . The typical  $pK_a$  of carboxylic acid group is 4.8 and our result showed a little shift (0.7) to higher. The shift of the isoelectric point of the carboxylic groups on the surface gold nanoparticles may be influenced by the electron-rich

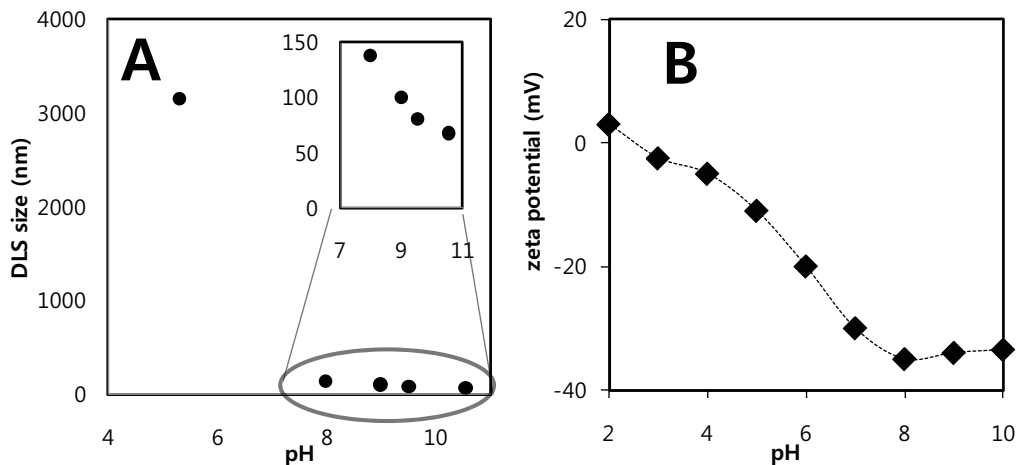


**Figure 3.6.** DLS size and zeta potential, A) DLS size analysis as a function of pH, B) Zeta potential of gold nanoparticles as a function of pH.

metallic surface. The local electron concentration near the surface of the gold nanoparticles would be higher than the bulk solution. These highly populated electrons then attract  $H^+$  ions resulting higher local  $H^+$  concentration, resulting the shift of the  $pK_a$  value.

#### 3.4.4. Salt induced gold nanoparticle aggregation

To exclude the possibility that the loss of emission at lower pH was due to only to aggregation, gold nanoparticles were treated with increasing concentration of NaCl up to 250 mM NaCl to induce flocculation. The size distribution and fluorescence emission of gently stirred suspensions to avoid any settling was measured with DLS using (Figure 3.7A). The fluorescence intensity was unchanged despite the detectable increase in the flocculation of the materials in the suspension (Figure 3.7B). In contrast, although a similar degree of flocculation was induced by pH change around pH 5 (Figure 3.3), a dramatic loss in emission intensity was observed suggesting different behavior for both cases.

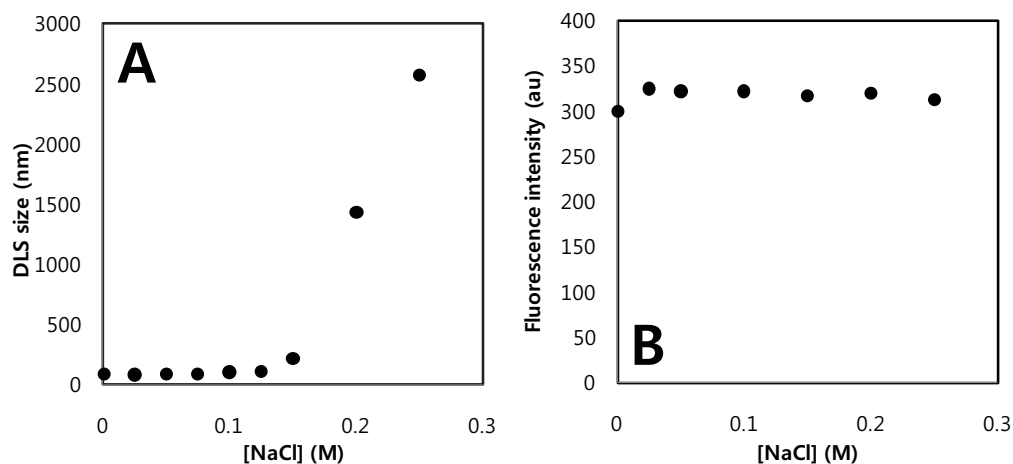


**Figure 3.7.** Controlled aggregation of the gold nanoparticle and its fluorescence: A) DLS particle size with different NaCl concentration, B) The fluorescence intensity with different NaCl concentration.

#### 3.4.5. Salt effect on excitation spectrum

The excitation spectra monitoring with 610 nm emission was measured as a function of pH for gold nanoparticle suspensions with and without added NaCl. For this, NaCl was added to a gold nanoparticle solution containing 1  $\mu$ M particles to form a mixture containing 100 mM NaCl. The result showed that the sudden transition in peak position of the excitation peak shift occurred at pH 7 (Figure 3.8A, B), whereas without added NaCl (Figure 3.3C, D), the transition was shifted about 2 pH unit lower.

#### 3.4.6. Mercaptooctanoic acid surface coverage estimation

The electric double layer (Debye layer) thickness was calculated from recently developed equation by Kimura et al. [153]. The Debye parameter,  $\kappa$  is defined from

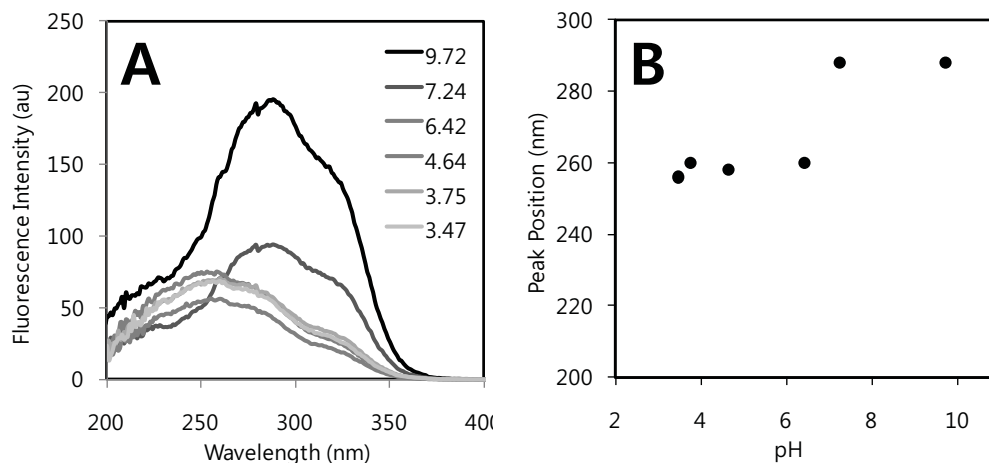


**Figure 3.8.** Excitation spectra shift in the presence of salt, A) Excitation spectra monitoring 610 nm emission from a gold nanoparticle solution containing 100 mM NaCl as a function of pH, B) Excitation peak wavelength change as a function of pH.

the following equation,  $\kappa = \left( \sum \frac{z_i^2 e^2 n_i}{\epsilon_r \epsilon_0 k T} \right)^{0.5}$ , in which  $z_i$  is the valence of  $i$ th ion,  $e$  is

the elementary electric charge,  $n_i$  is the bulk concentration of  $i$ th ion and is connected to the total bulk ion concentration by  $n = \sum n_i \epsilon_r$ , and  $\epsilon_r$  and  $\epsilon_0$  are the relative and

vacuum dielectric constants, respectively. The Debye layer is defined as  $1/\kappa$ . With the assumption of the added electrolytes, such as NaOH and HCl are dissociated completely over the whole pH region, the degree of electrolytic dissociation,  $\alpha$ , is

defined as,  $\alpha = \frac{[R^-]}{R_0}$ , where R is mercaptoctanoic acid. The surface charge density,

$\sigma$ , can be derived as a function of pH using the degree of electrolytic dissociation  $\alpha$  and the maximum surface charge density  $\sigma_0$ ,  $\sigma = \sigma_0 \alpha$ . Since mercaptoctanoic acid has one charge value, the calculated charge density for a carboxylic acid with one

charge is  $-1.6 \times 10^{-19}/0.214 \text{ nm}^2$  or  $0.75 \text{ C/m}^2$ , where the maximum surface area of the thiol for gold surface,  $S_0$ , was  $0.214 \text{ nm}^2$  [154].

Using the relationship shown in equation 3.1,

$$\sigma = \frac{V_e}{Area} = \frac{\varepsilon\varepsilon_0\psi}{\frac{1}{\kappa}} \quad (\text{eq. 3.1})$$

where  $V_e$  is the charge of an electron in Coulombs,  $\varepsilon$  is the dielectric constant,  $\varepsilon_0$  is the vacuum permittivity, and  $\psi$  is the surface potential, the surface area actually occupied by one charge in our samples can be estimated. To obtain  $\psi$  the surface potential we use the previously estimated surface charge density in the equation,

$$\sigma = \frac{2\varepsilon_x\varepsilon_0\kappa kT}{e} \sinh\left(\frac{y}{2}\right) \left[1 + \frac{1}{\kappa a} \left(\frac{2}{\cosh^2(y/4)}\right) + \frac{1}{(\kappa a)^2} \left(\frac{8 \ln[\cosh(y/4)]}{\sinh^2(y/2)}\right)\right]^{\frac{1}{2}} \quad (\text{eq. 3.2})$$

and solve for the parameter  $y$ . Using the relation,  $y = e\psi_0/kT$ . We obtain  $\psi_s$  the surface potential which can be used in equation 3.2 shown above, along with the other parameters to solve for the area occupied. Dividing the surface area of a particle by the surface area footprint of our charge the number of charges per particle can be obtained. The result at different pH is summarized in the Table 3.1. Overall, the result showed that the surface coverage of mercaptooctanoic acid on a particle is calculated to be 71 molecules per particle. Interestingly, this result is very well matched with our previous ICP-MS gold to thiol ratio analysis as reported in Chapter 2 and other reported gold to thiol ratio of 2 nm diameter gold nanoparticles with the range of  $\text{Au}_{309}(\text{thiol})_{75}$  to  $\text{Au}_{225}(\text{thiol})_{68}$  [86].

**Table 3.1.** Surface coverage by mercaptooctanoic acid

<b>pH</b>	<b>Debye layer (1/<math>\kappa</math>) (nm)</b>	<b><math>\sigma</math></b>	<b><math>\psi_s</math></b>	<b>Area occupied by one charge (m<sup>2</sup>)</b>	<b>MOA coverage/particle</b>
<b>2.7</b>	9.67	-0.061	-335	$2.7 \times 10^{-18}$	5.78
<b>5.3</b>	192.58	-0.296	-343	$5.4 \times 10^{-19}$	28.16
<b>7.97</b>	444.14	-0.716	-348	$2.2 \times 10^{-19}$	68.04
<b>8.3</b>	305.42	-0.728	-348	$2.2 \times 10^{-19}$	69.11
<b>8.98</b>	139.69	-0.740	-348	$2.2 \times 10^{-19}$	70.30
<b>9.5</b>	76.80	-0.744	-348	$2.2 \times 10^{-19}$	70.71
<b>10.54</b>	23.20	-0.748	-348	$2.1 \times 10^{-19}$	71.02

### 3.5. Discussion

The main hypothesis drawn from this work is that a change in the protonation status of the carboxylic acid of relatively short MOA can make a dramatic change in MOA brush configuration. A hypothetical diagram is shown in Figure 3.9A. In the charged, extended form the accessibility of water to the gold nanoparticle surface is greater than in the uncharged collapsed form. In the collapsed form, the local hydrophobicity at the gold surface is higher and the LMMCT excitation spectrum shifts to the blue.

The emission intensity at various pH divided by the corresponding absorbance at ~290 nm to correct for concentration effects (Figure 3.9B) can be used to extract a pK<sub>a</sub> of ~5.5. Although the pK<sub>a</sub>s of small carboxylic acids tend to be around pH 3-4, they can be higher for molecules with longer aliphatic chains, such as 4.9 for acetic acid and 4.89 for octanoic acid. Interaction of titratable groups with nanoparticle surfaces can lead to further pK<sub>a</sub> shift by up to 1.1 pH units [155].

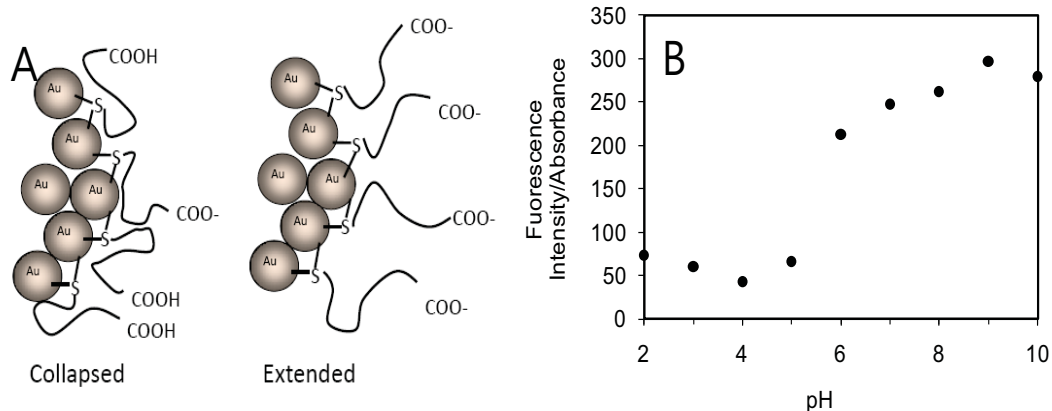


**Figure 3.9.** Brush configuration, (A) Hypothetical brush configuration; (B) Emission intensity divided by absorbance. The spheres are gold atoms at the particle interface. The gold atoms that form the rest of the nanoparticle are not shown.

Our gold nanoparticle system is believed to be different from the Au(I)-ligand complexes as evidenced by the following: (1) The improved photo- and thermal stability compared to the Au(I)-ligand complexes, (2) TEM image clearly showing 2.2 nm nanoparticles with gold lattice with typical Au-Au bond d-spacing of 0.22~0.24 nm and (3) ICP-MS result showed the ratio of elemental gold to sulfur is 1:0.27, which suggests sulfur layer covering the gold core of the particles. The starting Au(III) species would be in form of reduced Au (0) and start to produce Au(0)-Au(0) cluster as widely reported for the production of the thiol stabilized gold nanoparticles. As suggested in Chapter 2 it is possible that part of Au species forms Au(I)-S complexes on the surface of the gold nanoparticles and is responsible for the emission.

As described in the orbital diagram (Figure 3.10), the electron orbital change at different carboxylic acid protonation state could be involved in the transfer of excitation between the gold and the LMMCT complex. Protonated COOH which

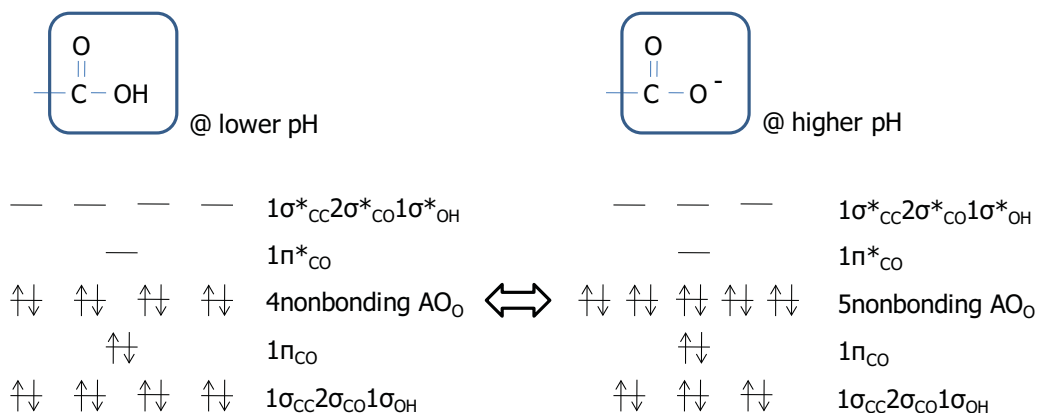


**Figure 3.10.** Molecular orbital change between charged and neutral carboxylic acid functional groups and its proposed band structure/electron population change.

lacks the number of nonbonding orbitals but deprotonated  $\text{COO}^-$  has an additional oxygen nonbonding orbitals. At higher pH the excitation spectrum maximum of the LMCCT complexes is lower in energy possibly due to some stabilization by the charged carboxylic acid.

In Figure 3.11, we have proposed energy diagrams to explain the dependency of the emission intensity on pH. As it is explained in Figure 3.8, and earlier, at lower pH, excitation is less efficient due to the increased overall energy gap between ground and excited states. This results in a change in overlap with gold transitions which affects the excitation spectrum energy maximum. The photoluminescence intensity also changes and is reduced at low pH despite the shift in the position of the the LMMCT singlet excited state to higher energy. This could be explained if in spite of increased electronic orbital overlap there is also an increased chance for nonradiative relaxation of the LMMCT excited state via bond geometry shift other process.

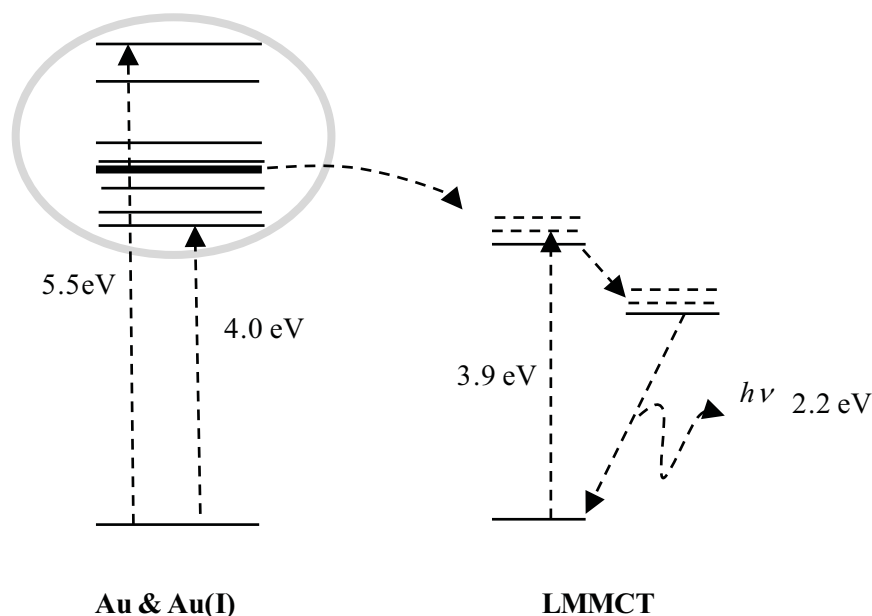


**Figure 3.11.** Proposed energy transfer diagram; The singlet excited state of the LMMCT complex is higher at low pH and lower at high pH. The position of the triplet state is same since the emission wavelength does not change by the pH.

It is also important to clarify the effect of aggregation itself in terms of the fluorescence intensity loss. As shown in the Figure 3.5, the addition of the NaCl in the gold nanoparticle solution did not affect the fluorescence intensity even though flocs formed at higher concentrations of NaCl. It means that interactions between the particles are not as strong of an influence of emission as is change in the protonation status of the molecules at the surface. Reversible aggregation behavior of carboxylated gold nanoparticles as a function of pH was reported by Li et al.[156] In their work, aggregation was identified by the distance-dependent red shift in the plasmon absorption. Their hypothesis was that pH dependent aggregation is the result of hydrogen bonding between the carboxylic acid groups on adjacent nanoparticles. This is certainly possible in our materials, since the DLS determined size of the

materials in the suspension is significantly larger than the 2 nm intrinsic particle size determined using TEM.

Via the NaCl-induced aggregation of the gold nanoparticle test, we have confirmed that the aggregation itself has less impact on the fluorescence intensity than does pH change. Increased ion concentration of Na<sup>+</sup> and Cl<sup>-</sup> screens the charge-charge interaction between the negatively charged carboxylic groups of the gold nanoparticle causing the aggregation between the particles. At the concentration of 100 mM of NaCl, the salt concentration which does not cause any significant aggregation, the pH dependence on the fluorescence intensity was tested and the result showed that the excitation peak position changed from 290 nm to 250 nm as before but at pH 7 while without NaCl the transition occurred around pH 5. The shift of the pKa value in the presence of the NaCl suggests the screening effect of the salt ions dissociated in the solution. The charged carboxylic acid groups attract the Na<sup>+</sup> ions so that they are more stabilized and may stay similarly charged at lower pH ranges.

The interactions between the fluorophore and solvent affect the energy difference between the excited and ground states. The energy difference can be estimated by the Lippert-Mataga equation, where  $\bar{\nu}_A$  and  $\bar{\nu}_F$  are the wavenumbers (cm<sup>-1</sup>) of the absorption and emission, respectively, h is Planck's constant (erg\*s), c is the speed of light (cm/s), a is the radius of the cavity in which the fluorophore resides (cm),  $\epsilon$  is the dielectric constant of the solvent, n is the refractive index of the solvent and  $\mu_E$  and  $\mu_G$  are dipole moments (Debye) at excited and ground states, respectively [1]. This equation is an approximation with neglecting the polarizability and higher-order terms (eq. 3.3).

$$\bar{\nu}_A - \bar{\nu}_F = \frac{1}{hc} \left( \frac{\epsilon - 1}{2\epsilon + 1} - \frac{n^2 - 1}{2n^2 + 1} \right) \frac{(\mu_E - \mu_G)^2}{a^3} \quad (\text{eq. 3.3})$$

In this equation, an increased value of  $n$  will decrease this energy loss while increased  $\epsilon$  value will increase the energy loss, which is  $\bar{\nu}_A - \bar{\nu}_F$  ( $\Delta\nu$ , here after). The refractive index is a high-frequency response which depends on the motion of electrons within the solvent molecules. This process is essential for the light absorption. In contrast, the dielectric constant is a static property which depends on both electronic and molecular motions. The molecular motion is the solvent reorganization at excited state. An increase in refractive index allows both ground and excited states stabilized by the movements of electrons within the solvent molecules. This will eventually decrease the energy difference between the ground and excited state. However, the reorientation of the solvent dipoles by the dielectric constant leads the energy decrease of the excited state and this requires the movement of entire solvent molecule.

The term in the above equation,  $\left(\frac{\epsilon-1}{2\epsilon+1} - \frac{n^2-1}{2n^2+1}\right)$  is the orientation polarizability ( $\Delta f$ , here after). The first term including the dielectric constant accounts for the shifts due to reorientation of the solvent dipoles and to the redistribution of the electrons in the solvent molecules. The second term containing refractive index accounts for only the redistribution of electrons. Thus, the difference of these two terms represents the spectral shifts due to the reorientation of the solvent molecules and it is why it is called orientation polarizability. Since the effect by the refractive index and electronic redistribution has only minor effect due to the approximately equal stabilization of the ground and excited states by the process, the Stokes shift is mostly affected by the solvent reorientation [1].

A Lippert-Mataga plot has been constructed as shown in Figure 3.12. The

slope is  $\frac{2}{hca^3} * \Delta\mu$  with the unit of  $\frac{\text{erg} \cdot \text{cm}^3}{(\text{erg} \cdot \text{s}) \cdot (\text{cm} \cdot \text{s}^{-1}) \cdot (\text{cm}^3)} = \text{cm}^{-1}$ . As shown in the

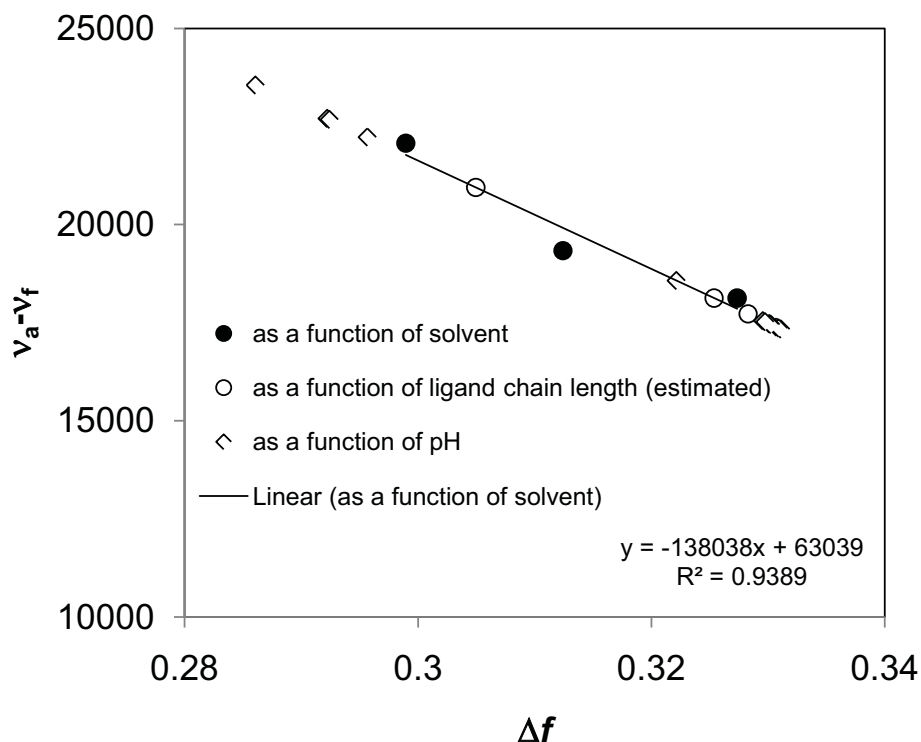


**Figure 3.12.** The Lippert-Mataga plot with the function of solvent, ligand chain length and pH. The slope is calculated to be 138038 (1/cm).

Figure, the slope is 138038 ( $\text{cm}^{-1}$ ). Since the dipole moment unit, Debye is defined as  $\text{erg}^{0.5} \text{cm}^{1.5}$ , the difference of dipole moment,  $\mu_E - \mu_G$ , can be determined by the following equation (eq. 3.4).

$$(\mu_E - \mu_G) = \left( \frac{\text{slope} \cdot h \cdot c \cdot a^3}{2} \right)^{0.5} \quad (\text{eq. 3.4})$$

From the above equation, the dipole moment is calculated to be -24 Debye after applying maximum excitation peak values from Figure 3.2D and also the different excitation and emission values with different solvent polarity shown in Table 3.2.

**Table 3.2.** Excitation and emission maximum, and energy shift for gold-MOA materials as function of solvent polarity.

<b>Molecule</b>	<b>Solvent/ Polarity Index</b>	<b>Excitation (eV)</b>	<b>Emission (eV)</b>	<b>Stokes Shift (eV)</b>
<b>Au-MOA</b>	Isopropanol/3.9	4.77	2.03	2.74
	Ethanol/5.2	4.43	2.03	2.40
	Water/9	4.28	2.03	2.25

The calculation was performed after assuming the fluorophore cavity radius is half the length of the Au-MOA molecule length. This is a reasonable number compared to dipole moment changes of other organic molecules. For example, molecule such as potassium bromide has the dipole moment of 10.4 Debye [157]. The true fluorophore cavity is difficult to estimate since the conformation of the ligand complex may vary slightly with different solvents.

The apparent value of  $\Delta f$  was calculated from the measured values of  $\bar{\nu}_A - \bar{\nu}_F$  ( $\Delta\nu$ , here after) for ligands of different chain length as well as a function of pH assuming that polarity is the major cause of the Stokes shift and follows the trend established in experiments using different solvents. In each case, experimentally deduced  $\Delta f$  values are within the norm as expected for short chain ligands at surfaces.

The argument for the collapse of the molecular brush at high pH is built from the observations regarding the change in Stokes shift of the emission as a function of solvent polarity. The Lippert-Mataga analysis was first used to show that for a given ligand, MOA, solvent polarity was able to cause a dipole moment change of -24 Debye between ground state and excited state, indicating that the excited state is more polar than the absorbing ground state.

Stokes shifts of similar magnitude and sign were also obtained for different ligand chain lengths, and used to estimate effective  $\Delta f$  (a function of dielectric constant and refractive index). These were found to lie in a reasonable range as estimated from solvent polarity and showed that even short ligands slightly shield the active site from the solvent. Because similar changes to the excitation spectra were also observed with changing pH, using the Lippert-Mataga fitted line,  $\Delta f$  values were also estimated. For both chain length and pH titration the estimated  $\Delta f$  were slightly less polar than that of Isopropanol. This is reasonable given the overall short chain lengths of ligands, and the ability of the carboxylic acid group to hydrogen bond water molecules. For reference, chloroform has a calculated  $\Delta f$  of 0.15 and hexane 0.01. Because the particles precipitate strongly in these solvents it is not possible to make the measurements described under those circumstances.

### 3.6. Conclusion

We have shown the different effects of the pH change on the properties of the mercaptooctanoic acid stabilized gold nanoparticle solution. The photo-luminescence intensity of the gold nanoparticle solution was linearly dependent on the pH change in the weak acidic to basic region above the pH 6. A significant shift in the excitation peak from 280-290 nm to 250-260 nm occurred at pH 6, near the  $pK_a$  value of the gold nanoparticle solution.

The surface bound mercaptooctanoic acid coverage was estimated to be 71 molecules per particle from the surface charge density calculation. This result agrees with the previously estimated from ICP-MS result and other reported gold nanoparticles with similar diameter. Also, the Lippert-Mataga analysis showed that the solvent polarity was able to cause a dipole moment change of -24 Debye between

ground state and excited state with the MOA ligand which suggests the excited state is more polar than the absorbing ground state and explains why the excitation spectra shifts with pH, but not the emission spectra.

## CHAPTER 4

### EFFECT OF NANOPARTICLES ON THE MEASUREMENT OF REACTIVE OXYGEN SPECIES BY THE AMPLEX RED ASSAY

*Part of this work has been published in part as a regular article in Lee et al, "The Accuracy of Amplex Red Assay for Hydrogen Peroxide in the Presence of Nanoparticles", Journal of Biomedical Nanotechnology, 5, 477-485 (2009).*

#### 4.1. Abstract

ROS formation is an important method to determine biocompatibility of a material since it is widely known that excessive ROS can damage cells and tissues. Changes in the level of ROS induced by materials are usually determined with assay kits such as Amplex Red (Invitrogen, Carlsbad, CA). However the nanoparticles themselves may interact with the reagents and affect the accuracy of the measurement. In some cases if they generate ROS themselves, a higher ROS content maybe detected. On the other hand if they have an antioxidant effect they may reduce the measurable ROS level. The ability of Amplex Red to report ROS concentration in the presence of several oxide nanoparticles as well as the gold nanoparticles of this project is examined.

#### 4.2. Introduction

Reactive oxygen species (ROS) including hydrogen peroxide ( $\text{H}_2\text{O}_2$ ) are harmful in body due to their superior reactivity toward biological components including tissues, proteins and DNA, and have been associated with skin and tissue aging, DNA damage and tumor development [158; 159]. Chemical assays such as Amplex Red (Invitrogen) are widely used to measure  $\text{H}_2\text{O}_2$  generated by cells in response to environmental or internal triggers. Amplex Red detects  $\text{H}_2\text{O}_2$  with a 1:1 stoichiometry. In the presence of horseradish peroxidase as a catalyst, the Amplex Red molecule degrades into ethanol and resorufin. Resorufin gives red fluorescence (emission at 590 nm) for detection (Figure 4.1)[160]. The detection limit of Amplex Red for  $\text{H}_2\text{O}_2$  is as low as 2 picomoles in ideal situations [161].

Recently there is great interest in using ROS levels for the evaluation of the biological safety of a variety of nanomaterials [20; 116; 162; 163; 164; 165; 166; 167; 168; 169]. For example, Lovric et al.[20] reported that cadmium-based quantum dots generated ROS and led to cell death and multiple organelle damage.

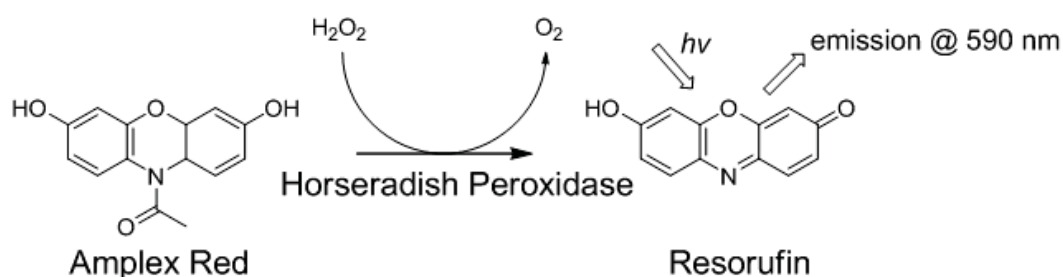


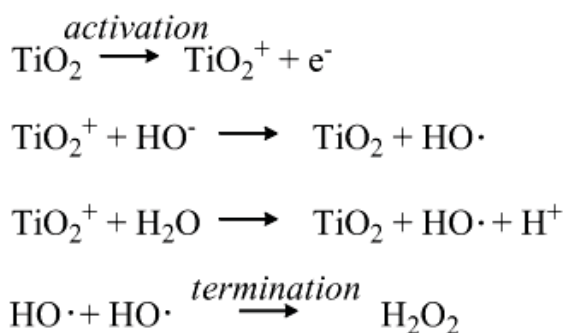
**Figure 4.1.** Chemistry scheme of Amplex Red conversion to resorufin in the presence of hydrogen peroxide using peroxidase: Optically transparent Amplex Red molecule is converted to fluorogenic molecule, resorufin with interacting 1:1 molar ratio to hydrogen peroxide. The reaction is catalyzed by horseradish peroxidase.

Similarly, Xia et al.[168] tested various nanoparticles ranging from TiO<sub>2</sub>, carbon black, to polystyrene, and showed some of the particles produced more oxidative stress than others and initiated mitochondrial apoptotic pathways. Park et al. [170] reported that CeO<sub>2</sub> nanoparticles induced oxidative stress of BEAS-2B cells, and the elevated level of ROS in the cell triggered cytosolic caspase-3 and chromatin condensation which led to cell apoptosis. Reeves et al. [171] showed that TiO<sub>2</sub> nanoparticles photolytically generated hydroxyl radicals ( $\cdot$ OH) which led to the formation of hydrogen peroxide and oxygen. These results clearly suggest a connection between some nanoparticles and the occurrence of oxidative species, however, to better understand the mechanisms involved, quantitative measurement of H<sub>2</sub>O<sub>2</sub> levels in the cell is necessary.

Accurate, quantitative measurement of H<sub>2</sub>O<sub>2</sub> levels in cells using Amplex Red is considered to be relatively straightforward, using a calibration curve obtained in appropriate medium for known amounts of H<sub>2</sub>O<sub>2</sub>. Typically, the concentration of H<sub>2</sub>O<sub>2</sub> in the experimental sample is derived by comparison of the measured fluorescence intensity of resorufin, relative to that observed at known concentrations of H<sub>2</sub>O<sub>2</sub> in the calibration standard. This assumes that the experimental specimen has had no effect on the intrinsic performance of the Amplex Red assay and on its ability to detect H<sub>2</sub>O<sub>2</sub>. This assumption may not hold in the presence of nanoparticles which have large surface areas able to interact both with the detection reagents (in this case Amplex Red), its products, and on the H<sub>2</sub>O<sub>2</sub> analyte.

In this work the performance of Amplex Red assay in the presence of oxide nanoparticles, cerium oxide (CeO<sub>2</sub>), tin oxide (SnO<sub>2</sub>), iron oxide (Fe<sub>2</sub>O<sub>3</sub>) and titanium oxide (TiO<sub>2</sub>). Also examined is the ability of gold nanoparticles studied in this work to generate ROS.

These nanoparticles are widely used in catalysis, but also for various biological applications including cellular uptake [172; 173], biological affinity reaction [174], and cell toxicity tests [175]. CeO<sub>2</sub> and Fe<sub>2</sub>O<sub>3</sub>, have been suggested to have antioxidant capability [176; 177; 178; 179], while TiO<sub>2</sub> is known to generate HO· species as water molecule is broken which eventually forms H<sub>2</sub>O<sub>2</sub> via the following several mechanisms including photolytic or electronic dissociation mechanisms [171; 180; 181]:



There are a few reports which state about the possible antioxidant activity by gold nanoparticles [182; 183]. Esumi et al. [182] showed the possibility of antioxidant activity by gold-chitosan composite nanoparticles. Here the particles had 80 times higher antioxidant activity compared to just chitosan composite which did not have any antioxidant activity. In their report, they have observed the best antioxidant activity at the 0.01 wt% to 0.1 wt% of chitosan in gold nanoparticles while the antioxidant activity was reduced with increasing chitosan coverage due to loss of gold surface exposure to the hydroxyl radicals formed by an H<sub>2</sub>O<sub>2</sub>/FeSO<sub>4</sub>. In this experiment the concentration of hydroxyl radicals were determined by spin-trapping method. Yakimovich et al. [183] showed antioxidant properties of gold nanoparticles using electron spin resonance (ESR) spectroscopy method. According to them, the antioxidant activity of the gold nanoparticles depended on the “specific” surface of the particles.

### 4.3. Materials and methods

#### 4.3.1 Materials

Amplex Red was purchased from Invitrogen (Carlsbad, CA). Other chemicals, solvents and enzymes including hydrogen peroxide, horseradish peroxidase, disodium phosphate, monosodium phosphate, dimethylsulfoxide (DMSO) were purchased from Sigma-Aldrich (St. Louis, MO). Water used in this experiment was purified with a Barnstead E-pure system (Waltham, MA). EBM (Endothelial cell basal medium without Phenol Red) was purchased from Lonza (Walkersville, MD).

Oxide nanoparticles were provided by the Center for Excellence in Nanopowders at the University of Utah (Table 4.1). Gold nanoparticle synthesis was described in section 2.2.2. Nanoparticles synthesized with 3 to 1 mercaptooctanoic acid to gold ratio in 10% EtOH in water were used.

#### 4.3.2 Reagent preparation

Amplex Red was dissolved in DMSO to make 500  $\mu\text{M}$  solution. Hydrogen peroxide solutions ranging from 0 to 5  $\mu\text{M}$  were prepared in E-pure water (pH 7, 18 mOhm) and used fresh. Horseradish peroxidase (HRP, 1 U/mL) was prepared as a 125 mM solution in sodium phosphate buffer at pH 7.4. One unit of HRP is defined to form 1.0 mg of purpurogallin from pyrogallol in 20 sec at pH 6.0 at 20°C by the manufacturer.

Nanoparticles were dispersed in E-pure water at as specified concentrations ranging from 0 to 0.5 mg/mL and sonicated in a pan sonicator (Fisher Scientific) for 10 min before the experiment to disperse the particles. Gold nanoparticles were used after purification by EtOH trituration.

#### 4.3.3. Measurement of nanoparticle size

The size of the oxide nanoparticles was measured by X-ray crystallography and confirmed by liquid nitrogen adsorption isotherm surface area measurement (AxisUltraDLD, Kratos, Manchester, UK). The size of gold nanoparticles was determined from TEM analysis. A Spectra Max fluorescence micro-well plate reader from Molecular Device (Toronto, ON) was used for the fluorescence analysis.

#### 4.3.4. Measurement of resorufin formation

Resorufin emission was measured using an excitation wavelength of 550 nm and emission wavelength at 590 nm using a microwell plate reader (Spectra MAX M2, Molecular Devices, Sunnyvale, CA).

#### 4.3.5. Effect of nanoparticles on resorufin formation in the absence of H<sub>2</sub>O<sub>2</sub>

To determine whether nanoparticles directly caused resorufin formation, 20  $\mu$ L of nanoparticles at various concentrations from 0 to 0.5 mg/mL were mixed with 20  $\mu$ L of 500  $\mu$ M of Amplex Red (AR) in separate wells of an opaque bottom microwell plate (Fisher Scientific, Pittsburg, PA) containing 160  $\mu$ L of 125 mM phosphate buffer prepared at pH 7.4. The total reaction volume was 200  $\mu$ L. The plate was incubated for 30 min at 37 °C during which the resorufin emission was measured every 5 min. The measured fluorescence intensity was corrected for light scattering and absorbance attenuation of measured nanoparticle emission at 590 nm. For example, Fe<sub>2</sub>O<sub>3</sub> a red colored nanoparticle suspension had the largest correction (~74 %), TiO<sub>2</sub> (~14 %) while the other nanoparticles required no appreciable correction of the measured fluorescence intensities.

#### 4.3.6. H<sub>2</sub>O<sub>2</sub> concentrations in the presence of nanoparticles via resorufin formation

To determine whether Amplex Red is capable of accurately measuring a known amount of H<sub>2</sub>O<sub>2</sub>, 120  $\mu$ L of 125 mM (pH 7.4) phosphate buffer were placed in each well of a 96-well micro-well plate. Twenty  $\mu$ L of 50  $\mu$ M H<sub>2</sub>O<sub>2</sub>, 20  $\mu$ L of 500  $\mu$ M of Amplex Red solution, 20  $\mu$ L of nanoparticle suspension at various concentrations and 20  $\mu$ L of 1 U/mL HRP solution were added mixtures incubated for 30 min at at 37 °C during which the resorufin fluorescence measured as before. The measured fluorescence intensity was corrected for light scattering/absorbance attenuation of measured nanoparticle emission at 590 nm as already described.

The concentration of H<sub>2</sub>O<sub>2</sub> in each well was obtained by comparison with the fluorescence emission intensity from a calibration curve obtained using final mixture concentrations of 50  $\mu$ M of Amplex Red and 0.1 U/mL of HRP in 125 mM pH 7.4 phosphate buffer over the same concentrations of H<sub>2</sub>O<sub>2</sub> used in the experiment. An R<sup>2</sup> value of 0.9904 was obtained for the calibration, confirming the linear relationship between hydrogen peroxide concentration and emission at the range below 1  $\mu$ M concentration of hydrogen peroxide.

### 4.4. Results and discussion

#### 4.4.1. Physical characterization

The physical properties of the nanoparticles used in this study are listed in Table 4.1. Except for gold nanoparticles whose size were characterized directly by TEM, the size of the other oxide nanoparticles was calculated from surface area using liquid nitrogen adsorption isotherm surface area measurement (BET measurement, AxisUltraDLD, Kratos, Manchester, UK) and XRD measurements (Rigaku, AFC diffractometer, Japan)

**Table 4.1.** Physical properties of nanoparticles used in this study (\*This measurement is obtained from TEM images.).

<b>Powder</b>	<b>Phase</b>	<b>Average Crystallite size (from XRD*)</b>	<b>Surface Area (from BET)</b>	<b>Particle Size (From surface Area)</b>
Cerium Oxide (CeO <sub>2</sub> )	-	3 nm	140 m <sup>2</sup> /g	9 nm
Iron Oxide (Fe <sub>2</sub> O <sub>3</sub> )	Maghemite	4 nm	180 m <sup>2</sup> /g	6 nm
Tin Dioxide (SnO <sub>2</sub> )	Cassiterite	3 nm	200 m <sup>2</sup> /g	4 nm
Titanium Dioxide (TiO <sub>2</sub> )	Anatase	5 nm	170 m <sup>2</sup> /g	10 nm
Gold nanoparticles (AuNP)	-	2.2 nm*	-	-

#### 4.4.2. Oxide nanoparticles

Figure 4.2 shows the amount of resorufin fluorescence produced after 30 min of incubation in the presence of varying amounts of oxide nanoparticles, without the addition of H<sub>2</sub>O<sub>2</sub> and HRP.

Even in the absence of nanoparticles there is a small amount of resorufin produced after time, presumably as a result of photooxidative processes. In the presence of nanoparticles a significant increase in the amount of resorufin was noted, which increased with higher nanoparticle concentrations. SnO<sub>2</sub> nanoparticles produced significantly more resorufin with increasing particle concentration over that of other nanoparticles.

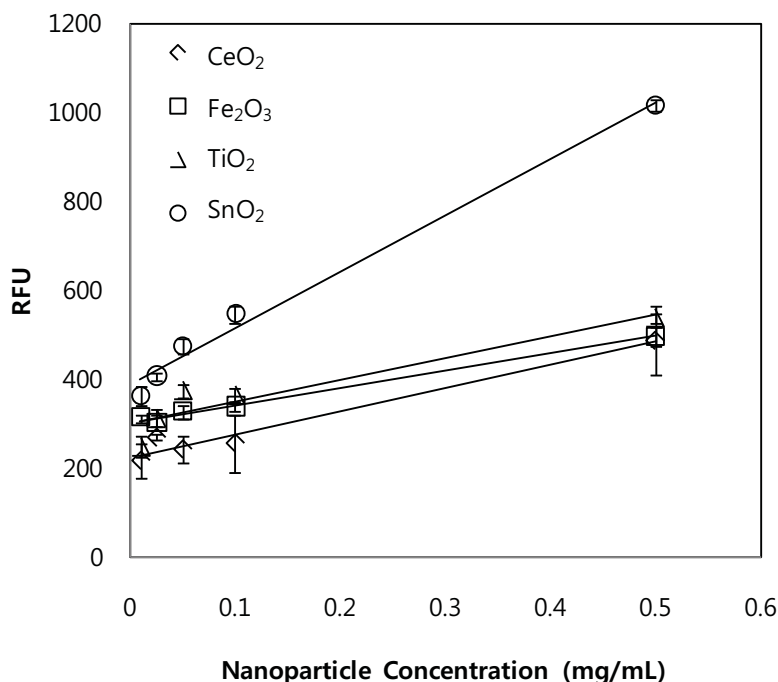


**Figure 4.2.** Resorufin fluorescence emission intensity after 30 min of incubation with various concentrations of nanoparticles. Each sample contained 50  $\mu\text{M}$  Amplex Red, but no  $\text{H}_2\text{O}_2$  and HRP. The measurement was performed at 37  $^\circ\text{C}$ .

Amplex Red assay was used to measure 0.5  $\mu\text{M}$  of  $\text{H}_2\text{O}_2$  in the presence of each nanoparticle at a concentration of 0.5 mg/mL in buffer and in mammalian cell culture media containing 0.1 U/mL HRP and 50  $\mu\text{M}$  Amplex Red (Figure 4.3). Except for the case of  $\text{SnO}_2$ , less than 0.5  $\mu\text{M}$   $\text{H}_2\text{O}_2$  was detected. A similar trend was observed in media, except that in addition,  $\text{TiO}_2$  nanoparticles did not seem to affect  $\text{H}_2\text{O}_2$  measurements. No nanoparticles showed a clear reduction in the overall amount of detectable  $\text{H}_2\text{O}_2$  in medium compared with water solution. The plotted data reflect measurements taken at the 30 minute time point of the reaction, well after the reaction had reached completion with a finite amount of  $\text{H}_2\text{O}_2$ .

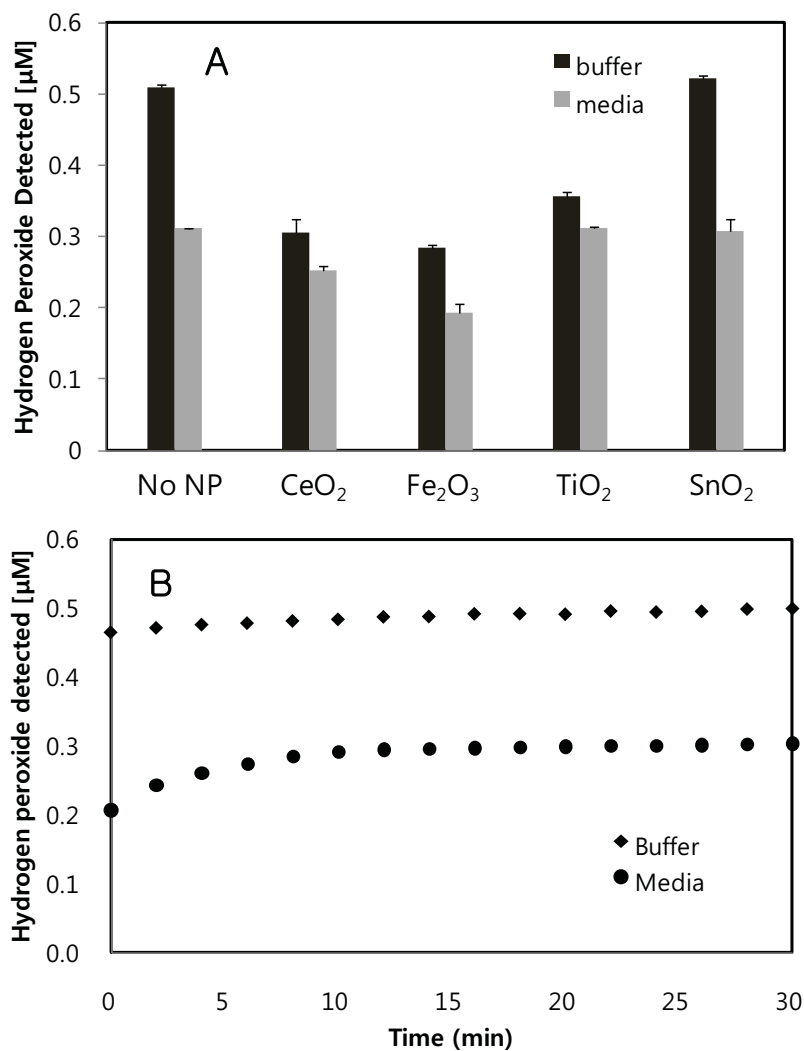


**Figure 4.3.** Detection of H<sub>2</sub>O<sub>2</sub>, (A) Detection of H<sub>2</sub>O<sub>2</sub> in the presence of nanoparticles in buffer (black bars) and in EBM media (grey bars): Resorufin signal intensity was taken after 30 min of incubation at 37 °C and converted to an apparent H<sub>2</sub>O<sub>2</sub> concentration using a calibration curve obtained in buffer. Each solution contained 50 µM of Amplex Red, 0.5 mg/mL of nanoparticles, 0.5 µM of H<sub>2</sub>O<sub>2</sub>, and 0.1 U/mL HRP. (B) Kinetics of the hydrogen peroxide detection without the presence of nanoparticles: Resorufin intensity was taken every 2 min during the test at 37 °C and converted to an apparent H<sub>2</sub>O<sub>2</sub> concentration using a calibration curve obtained in buffer. Each solution contained 50 µM of Amplex Red, 0.5 µM of H<sub>2</sub>O<sub>2</sub>, and 0.1 U/mL HRP.

Figure 4.4 shows the time course of data taken for these two cases. Because of the limitations of the microarray device the earliest time point recorded was 2 min. Clearly the reaction reached completion after 10 min, so the reported  $\text{H}_2\text{O}_2$  detectability result is not related to gross alteration in the kinetics of the reaction. The ability of Amplex Red assay to measure  $\text{H}_2\text{O}_2$  in the presence of nanoparticles as a function of HRP concentration was also evaluated (Figure 4.4). If adsorption and denaturation of HRP were a significant factor in the detection of  $\text{H}_2\text{O}_2$ , this would

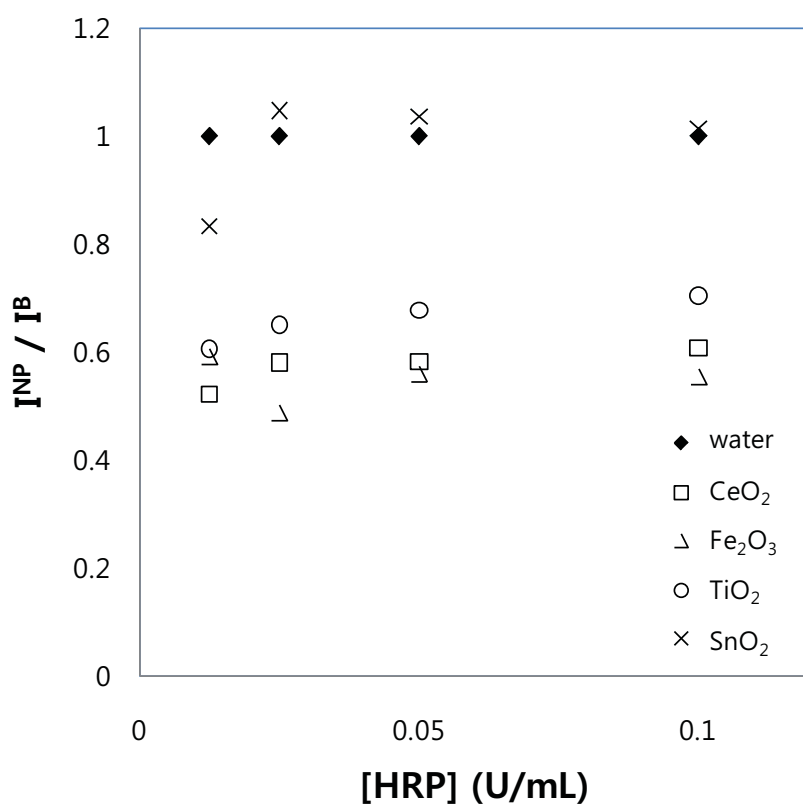


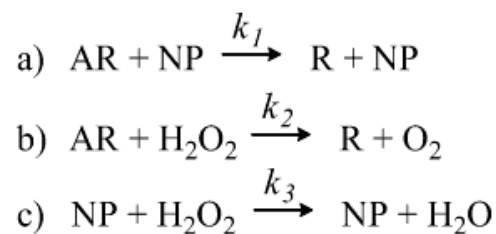
**Figure 4.4.** Ratio of resorufin fluorescence signal intensity measured in the presence of nanoparticles ( $I^{\text{NP}}$ ) divided by resorufin signal intensity detected in buffer ( $I^{\text{B}}$ ) plotted as a function of HRP concentration: Resorufin fluorescence intensity was measured after 30 min of incubation at 37 °C. Each solution contained 50  $\mu\text{M}$  of Amplex Red, 0.5 mg/mL of nanoparticles and 0.5  $\mu\text{M}$  of  $\text{H}_2\text{O}_2$ .

show up as poorer detectability at lower HRP concentrations than at higher concentrations. For each HRP concentration, the results are plotted as a ratio of resorufin fluorescence signal intensity measured in the presence of nanoparticles,  $I^{NP}$ , divided by signal intensity detected in buffer in the absence of nanoparticles  $I^B$ . A fixed concentration of 0.5  $\mu\text{M}$   $\text{H}_2\text{O}_2$  was used. For each nanoparticle, no difference was observed in the detectability of  $\text{H}_2\text{O}_2$  over the range of HRP concentration surveyed.

From Figure 4.4, we cannot exclude that some binding of HRP to the various particles used in this study is taking place. A drop-off in enzyme activity at the lowest HRP concentrations (0.0125 U/mL) in case of  $\text{SnO}_2$  suggests the possibility. The point is to show that using reasonable HRP concentrations for the Amplex Red protocol (i.e. not catalyst limiting conditions) the measurement of  $\text{H}_2\text{O}_2$  is not affected by gross denaturation of the catalyst. We can estimate the amount of HRP that could bind to the surface of 4 nm diameter nanoparticles. At higher concentrations of HRP this amount is largely insignificant. What may be most significant is that it may be possible for nanoparticles to competitively bind and deactivate small amounts of endogenous enzymes from the specimen. This may become another important complication in the interpretation of  $\text{H}_2\text{O}_2$  measurement results using this system, and may also play a role in other bio-sensing reactions that involve enzyme catalysts.

There are three different mechanisms which occur simultaneously during the measurement of  $\text{H}_2\text{O}_2$  using Amplex Red in the presence of nanoparticles: 1) A direct reaction between nanoparticles (NP) and Amplex Red (AR), which produces resorufin (R) via mechanism a); 2) The HRP-assisted reaction of Amplex Red with  $\text{H}_2\text{O}_2$  via mechanism b); and 3) The reaction of  $\text{H}_2\text{O}_2$  with oxide nanoparticles via mechanism c). Neglected in this scheme is simple surface adsorption of  $\text{H}_2\text{O}_2$  on nanoparticle

surfaces that does not lead to breakdown of  $\text{H}_2\text{O}_2$  but still prevents  $\text{H}_2\text{O}_2$  from being detected.



The three mechanisms listed in equations a), b) and c), seem to be the most important processes, so we have only analyzed and discussed these major effects. Other factors such as  $\text{H}_2\text{O}_2$  or enzyme binding to nanoparticles were not considered for the calculation. As shown by the calculation based on change in enzyme activity, the amount of HRP lost to binding is expected to be a small fraction of the total HRP present for the other experiments where high HRP concentrations were used.

For mechanisms a) and b), the reaction rates were estimated from the time dependent development of resorufin fluorescence in the first 30 min in the presence of 0.5 mg/mL nanoparticles. The end points of these linear curves were used to obtain Figure 4.2. For mechanism a, assuming the reaction is not limited by nanoparticle concentration or active surface area, the consumption of Amplex Red during the 30 minute incubation period can be expressed mathematically:

$$-\frac{d[\text{AR}]}{dt} = k_1[\text{AR}][\text{NP}] = k_1[\text{AR}][\text{NP}]_0 \quad (\text{eq. 4.1})$$

$$-\frac{d[\text{AR}]}{[\text{AR}]} = k_1[\text{NP}]_0 dt \quad (\text{eq. 4.2})$$

$$[\text{AR}](t) = [\text{AR}]_0 e^{-k_1[\text{NP}]_0 t} \quad (\text{eq. 4.3})$$

and the rate constant,  $k_1$  obtained:

$$k_1 = -\frac{1}{[NP]_0 t} \log \frac{[AR](t)}{[AR]_0} \left( \frac{mL}{mg \cdot sec} \right) \quad (\text{eq. 4.4})$$

Using the measured rate of appearance of resorufin emission to estimate the consumption of AR, we obtained for each nanoparticle:

The rate  $k_2$  was determined from the time dependence of HRP catalyzed conversion of Amplex Red in the presence of known concentrations of  $H_2O_2$ , but no nanoparticles (Mechanism b). The rate constant  $k_2$  can be expressed and solved from:

$$-\frac{d[AR]}{dt} = k_2 [AR] [H_2O_2] \quad (\text{eq. 4.5})$$

where  $d(t) = [H_2O_2]_0 - ([AR]_0 - [AR](t))$  since the Amplex Red is consumed in a 1:1 reaction of with hydrogen peroxide. Rearranging this equation gives:

$$-\frac{d[AR]}{[AR]^2 - ([AR]_0 - [H_2O_2]_0)[AR]} = k_2 dt \quad (\text{eq. 4.6})$$

from which  $k_2$  can be extracted as:

$$k_2 = -\frac{1}{([AR]_0 - [H_2O_2]_0)t} \log \left( \left( \frac{[AR]_0 - [H_2O_2]_0}{[AR]_0} \right) \left( \frac{[AR] - ([AR]_0 - [H_2O_2]_0)}{[AR]} \right) \right) \left( \frac{1}{\mu M \cdot sec} \right) \quad (\text{eq. 4.7})$$

For example, when  $[H_2O_2]_0 = 0.5 \mu M$ ,  $k_2 = 0.000266 \left( \frac{1}{\mu M \cdot sec} \right)$ . This was obtained using the early time dependence of measured resorufin production shown in Figure 4.5.

The rate of reaction between nanoparticles and  $H_2O_2$ ,  $k_3$ , can be obtained by solving the two equations for the rate of change in Amplex Red and  $H_2O_2$  concentrations expressed as:

$$-\frac{d[AR]}{dt} = k_1 [AR] [NP] + k_2 [AR] [H_2O_2] \quad (\text{eq. 4.8})$$

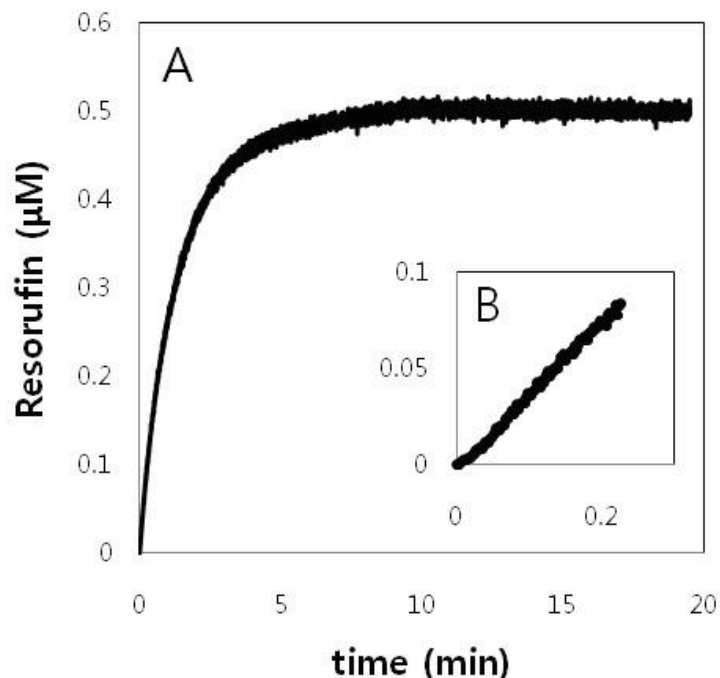


**Figure 4.5.** The measurement of the resorufin formation after the mixing with  $H_2O_2$ . (A) Overall range of the measurement, (B) Linear region of the graph where  $k_2$  value has been calculated. The reaction contained  $0.5 \mu\text{M}$  hydrogen peroxide,  $50 \mu\text{M}$  of Amplex Red and  $0.1 \text{ U/mL}$  HRP in  $\text{pH } 7.4$   $125 \text{ mM}$  PBS at  $37^\circ\text{C}$ .

$$-\frac{d[H_2O_2]}{dt} = k_2[AR][H_2O_2] + k_3[NP][H_2O_2] \quad (\text{eq. 4.9})$$

where the first term in equation 4.8 represents the direct conversion of Amplex Red to resorufin by Mechanism a) and the second term the enzyme catalyzed conversion by Mechanism b). The change in  $H_2O_2$  level (eq. 4.9) is a combination of enzyme catalyzed conversion of Mechanism b) and direct loss of  $H_2O_2$ . Using the values for  $k_1$  and  $k_2$  concentrations obtained earlier, and the overall measured concentrations of resorufin, from which the residual Amplex Red concentration was estimated,  $k_3$  values for each nanoparticle mixture were numerically solved (Table 4.2).

**Table 4.2.**  $k_1$  and  $k_3$  values for each nanoparticle at the concentration of 0.5 mg/mL ( $\frac{mL}{mg \cdot sec}$ )

	<b>CeO<sub>2</sub></b>	<b>Fe<sub>2</sub>O<sub>3</sub></b>	<b>SnO<sub>2</sub></b>	<b>TiO<sub>2</sub></b>
$k_1$	1.2x10 <sup>-6</sup>	1.3 x10 <sup>-6</sup>	2.6 x10 <sup>-6</sup>	1.4 x10 <sup>-6</sup>
$k_3$	0.0262	0.0316	0.0060	0.0184

The rate constants are higher than the previously reported values [177; 184; 185] determined for the catalytic decomposition of hydrogen peroxide by oxide particles. For example, if the unit of  $k_3$  is converted to  $M^{-1}sec^{-1}$ , the Fe<sub>2</sub>O<sub>3</sub> nanoparticle has the reaction constant of 3.53  $M^{-1}sec^{-1}$  with molar concentration based on the number of Fe atoms present in the powders. The reference values of the iron oxide rate constant on hydrogen peroxide decomposition were shown in Table 4.3.

There are at least two reasons why our  $k_3$  values are higher. First in the simplified mechanism presented earlier we have treated each nanoparticle as an independent reagent. However, it is the concentration of nanoparticle active surface sites that is relevant for this analysis, since each nanoparticle has the potential to react with more than one H<sub>2</sub>O<sub>2</sub> molecule simultaneously. These results imply there are about 100 active surface sites per particle functioning independently.

**Table 4.3.** Rate constants for iron oxide catalyzed hydrogen peroxide decomposition [177]

<b>Rate Constant (<math>M^{-1}sec^{-1}</math>)</b>	<b>Type of iron oxide</b>	<b>Reference</b>
<b>0.019-0.067</b>	Goethite	[177]
<b>0.013-0.031</b>	Fe <sub>2</sub> O <sub>3</sub> -Al <sub>2</sub> O <sub>3</sub>	[184]
<b>0.037</b>	Fe <sub>2</sub> O <sub>3</sub> coated on Al <sub>2</sub> O <sub>3</sub> core	[185]

For 6 nm Fe<sub>2</sub>O<sub>3</sub> particles used in this work, the surface area per particle is about 113 nm<sup>2</sup> which is consistent with this idea, if we assume that each H<sub>2</sub>O<sub>2</sub> footprint is about 1 nm<sup>2</sup>. According to Deng et al.[186] the distance between the O atoms in the lattice of Fe<sub>2</sub>O<sub>3</sub> is 0.229 nm. In a 1 nm<sup>2</sup> region, there are around 25 oxygen atoms available. If there is one oxygen vacancy created in every 25 oxygen site (~4% vacancy density), it creates about 1 reactive site per 1nm<sup>2</sup> area and be consistent with ~ 100 H<sub>2</sub>O<sub>2</sub> per particle.

Also, according to Roh et al.[187], the percentage of oxygen vacancies in some metal oxide materials can range from 0~50%. Our assumed 4% vacancy density is a conservative estimate for the number of vacancies/potential active sites present. The fact that only this small number of binding sites are needed to explain the experimental results further suggest that the process of H<sub>2</sub>O<sub>2</sub> binding without reaction is not a particularly important factor in for our analyses.

The calculated  $k_1$  and  $k_3$  values are inversely correlated with each other with a correlation coefficient of 0.994. This result suggests a competitive relation between the process (a) and (c). This suggests that a closely related or possibly the same active site is involved in both cases. A significantly weaker correlation between surface area and  $k_1$  of 0.789 and surface area and  $1/k_3$  rate of 0.725 was observed. Recall, we have omitted the reaction of HRP with NP in this model, based on the results shown in Figure 4.3. However this omission may be responsible for the weaker correlations with surface area if a third species is capable of occupying the nanoparticle surface.

In order to utilize the Amplex Red assay to obtain an accurate estimate of H<sub>2</sub>O<sub>2</sub> concentration, it is necessary to account for consumption processes described by mechanism a and c. This is most easily done using a simulation approach to estimate

the unaccounted for  $\text{H}_2\text{O}_2$  given specific concentrations of Amplex Red, HRP, temperature, etc. Here we illustrate a procedure for the case studied in this work.

Using the reaction constants,  $k_1$ ,  $k_2$  and  $k_3$ , obtained in the above analysis the expected resorufin formation as a function of time can be simulated when: 1) when there is no interaction between the nanoparticles and Amplex Red (ie,  $k_1 = 0$ ) (Figure 4.6A), 2) when there is no interaction between the nanoparticles and hydrogen peroxide (i.e.,  $k_3 = 0$ ) (Figure 4.6B), and 3) when both  $k_1 = 0$  and  $k_3 = 0$  (Figure 4.6C). When  $k_3 = 0$ , there is no direct consumption of  $\text{H}_2\text{O}_2$  molecules by the interactions with nanoparticles which results in a higher measured resorufin concentration. As can be seen from Figure 4.5B the nanoparticle-dependent differences in measure  $\text{H}_2\text{O}_2$  are eliminated, except in the case of  $\text{SnO}_2$ . The final amount of resorufin present after 30 min is determined by the initial input amount of hydrogen peroxide (which reacted very quickly, hence the steep increase in the first few seconds) plus slow, but spontaneous conversion of Amplex Red to resorufin by the nanoparticles, as described by Mechanism a. When only  $k_1 = 0$  then the measured resorufin concentration is that produced by Mechanism b attenuated by the competition of Mechanism c for  $\text{H}_2\text{O}_2$  (Figure 4.6A). When both processes are turned off the time dependent resorufin production should look like Figure 4.6C, and the actual total  $\text{H}_2\text{O}_2$  concentration estimated accordingly.

Of course when all three mechanisms are included, the resorufin production over 30 min of reaction duration can be plotted as in Figure 4.7. As expected, the simulated result showed that the concentration change of resorufin proceeds in two stages. At early times there is a steep rise in resorufin production dominated by mechanism b followed by a plateauing region dominated by Mechanism a.

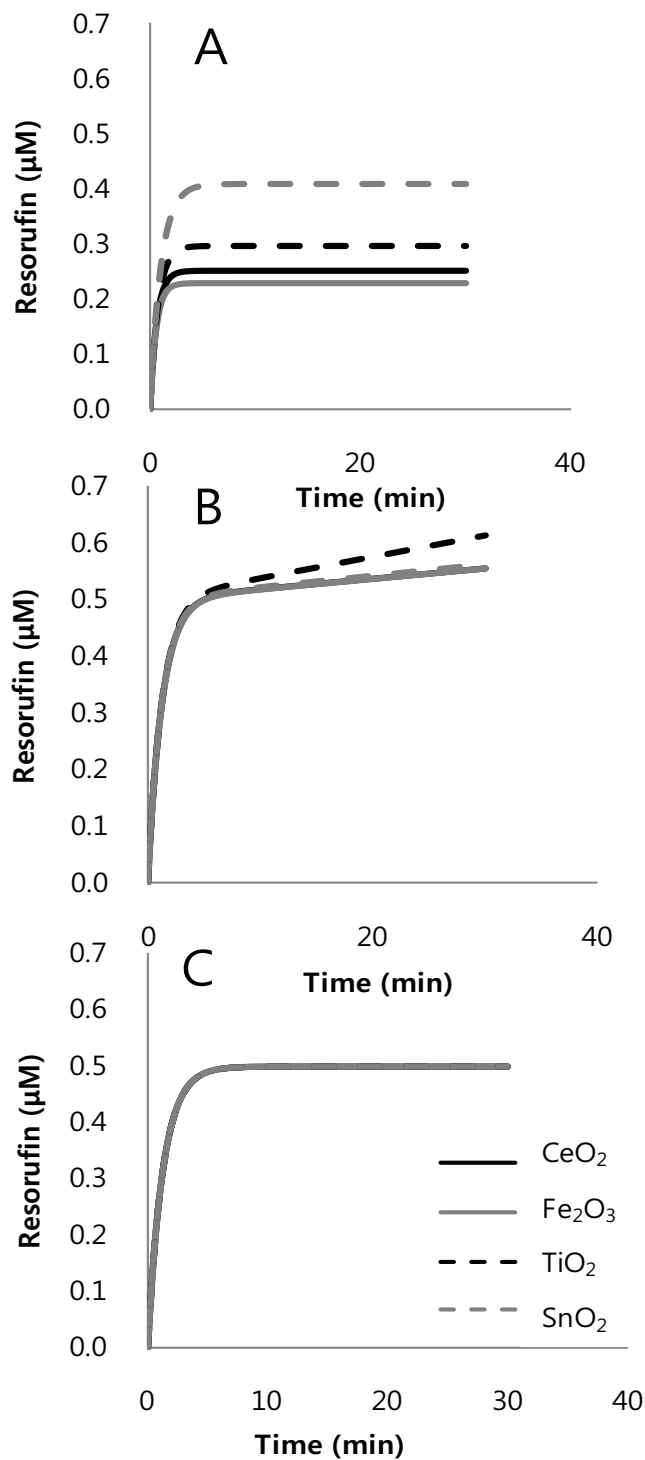


**Figure 4.6.** Computer simulation on resorufin concentration profile with assumptions: Simulated result of resorufin production with assumption of  $k_1=0$  (A),  $k_3=0$  (B) and  $k_1=0$  and  $k_3=0$  (C).

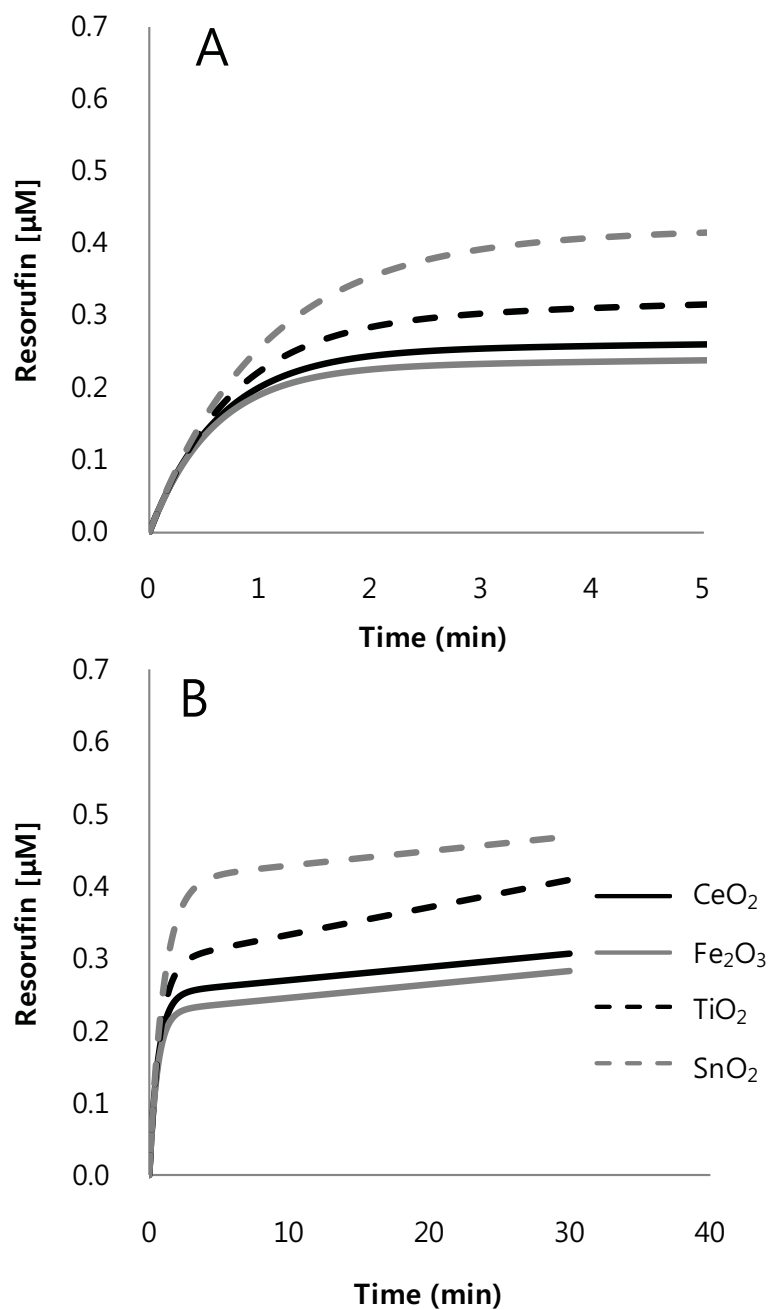
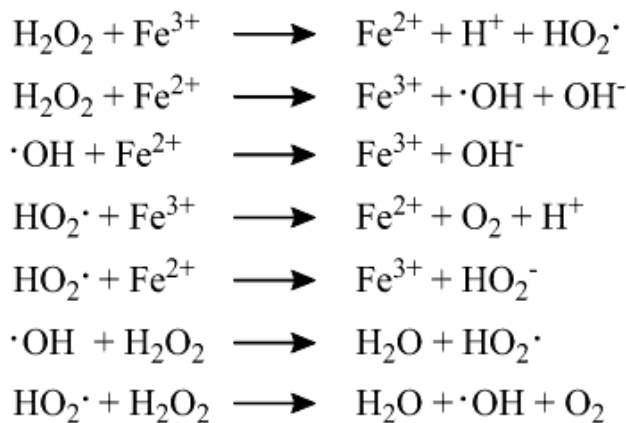


**Figure 4.7.** Computer simulation of the concentration profile is shown over time: Simulated concentration profile of resorufin production is shown at early time (5 min) (A) and over the entire 30 min time course (B) assuming all reactions are occurring simultaneously.

The inability of the Amplex Red assay to correctly measure the 0.5 M H<sub>2</sub>O<sub>2</sub> concentration in the presence of CeO<sub>2</sub>, TiO<sub>2</sub> and Fe<sub>2</sub>O<sub>3</sub> nanoparticles is consistent with the reported antioxidant activity of such nanoparticles [176; 177; 178; 188]. According to these studies, the anti-oxidant effect of metal oxide nanoparticles like TiO<sub>2</sub>, may occur at the site of oxygen vacancies (O-vac) of the metal-oxide nanoparticles [180; 189; 190; 191; 192].

O-vac sites in some of metal oxide crystals can induce dissociation of small molecules such as water or possibly peroxide molecules to form hydroxyl groups or water, respectively. Thus, these nanoparticles may be capable of the reduction of hydrogen peroxide molecules to water, reducing the detectable amount of H<sub>2</sub>O<sub>2</sub>. In the case of Fe<sub>2</sub>O<sub>3</sub>, it is thought that Fe<sup>2+</sup> and Fe<sup>3+</sup> directly interacts with hydrogen peroxide to decompose and form radicals and the radicals also react with hydrogen peroxide to decompose the molecule[177].



In contrast, SnO<sub>2</sub> had little effect of the ability of Amplex Red to detect H<sub>2</sub>O<sub>2</sub>. One major difference between SnO<sub>2</sub> and the other three (CeO<sub>2</sub>, Fe<sub>2</sub>O<sub>3</sub> and TiO<sub>2</sub>) is that SnO<sub>2</sub> does not readily exhibit multiple valence states in a single particle, but CeO<sub>2</sub>, Fe<sub>2</sub>O<sub>3</sub>, and TiO<sub>2</sub> do (e.g. Fe<sup>2+</sup>/Fe<sup>3+</sup>, Ti<sup>2+</sup>/Ti<sup>3+</sup>/Ti<sup>4+</sup> and Ce<sup>3+</sup>/Ce<sup>4+</sup>) [193]. These different types of valences may facilitate decomposition of hydrogen peroxide

through redox processes. In fact, this is used to explain the good catalytic performance of  $\text{CeO}_2$  and  $\text{Fe}_2\text{O}_3$ .

Finally, the fact that the above described trends are also observed when the reactions are carried out in EMB media underscores the difficulty in obtaining accurate measurement of biochemical markers in the presence of nanoparticles in cell culture assays. The ability for the nanoparticles to compete for  $\text{H}_2\text{O}_2$  via Mechanism c, is reduced in media, as seen by the smaller difference in measured  $\text{H}_2\text{O}_2$  with and without nanoparticles in media compared to just buffer. The loss in competitiveness is not the same for all materials. For example, the ability for  $\text{TiO}_2$  nanoparticles to consume additional  $\text{H}_2\text{O}_2$  appears to have been eliminated, partly eliminated for  $\text{CeO}_2$ , and unchanged for  $\text{Fe}_2\text{O}_3$ . While  $\text{TiO}_2$  is a photoactive nanoparticle capable of  $\text{H}_2\text{O}_2$  production of water when illuminated by UV light, this is unlikely to have made a significant impact in our experiments, since exposure to room light was minimal. The fact that the amount of  $\text{H}_2\text{O}_2$  measured did not exceed the expected amount as measured without nanoparticles in either buffer or media supports this. Probably the  $\text{TiO}_2$  nanoparticle surface is simply occupied with media components which prevent the usual nanoparticle-induced process of  $\text{H}_2\text{O}_2$  consumption. Why this does not occur for the other nanoparticles is not certain from this work, but may also be related to the multivalency of  $\text{TiO}_2$  as discussed earlier. At this point it is difficult to say whether the effect is caused by strong binding of organic molecules from the media, or the presence of reducing agents that interfere with the redox processes involving nanoparticle-induced  $\text{H}_2\text{O}_2$  decomposition. In any event, these results show that not only the surface area of the nanoparticles but also their specific chemical composition affects the outcome of the Amplex Red  $\text{H}_2\text{O}_2$  assay in complex media, and suggest

that similar effects may occur for other ROS and biochemical marker assays. These must be accounted for in order to obtain accurate measurements.

#### 4.4.3. Gold nanoparticles

Following the calibration scheme described in the previous section, the effect of gold nanoparticles for ROS generation was determined. For this, two control samples, a positive control containing no nanoparticles but 5  $\mu\text{M}$   $\text{H}_2\text{O}_2$ , and a negative control containing no nanoparticles and no  $\text{H}_2\text{O}_2$ . One U/mg of HRP was present added to both samples. One unit of HRP is defined to form 1.0 mg of purpurogallin from pyrogallol in 20 sec at pH 6.0 at 20°C by the manufacturer.

As expected the Amplex Red assay reported the correct of  $\text{H}_2\text{O}_2$  concentration within 10 min of incubation for the positive control sample. The negative control showed a typical baseline formation of resorufin as was shown earlier, even though no substrate is present. This has been attributed to photo-initiated resorufin formation.

Two experimental samples were prepared, one with 0.04  $\mu\text{M}$  of gold nanoparticles and the other 0.2  $\mu\text{M}$  gold nanoparticles. One U/mg of HRP was present added to both samples and no  $\text{H}_2\text{O}_2$  was added (Figure 4.8).

#### 4.5. Conclusion

Four different types of oxide nanoparticles,  $\text{CeO}_2$ ,  $\text{Fe}_2\text{O}_3$ ,  $\text{TiO}_2$  and  $\text{SnO}_2$  were evaluated for their ability to interfere with the Amplex Red assay to detect  $\text{H}_2\text{O}_2$ .  $\text{CeO}_2$ ,  $\text{Fe}_2\text{O}_3$  and  $\text{TiO}_2$  nanoparticles under-reported the actual  $\text{H}_2\text{O}_2$ , meanwhile  $\text{SnO}_2$  nanoparticle had no such effect. All types of nanoparticles showed an intrinsic capability for converting Amplex Red molecules to fluorescent resorufin in the

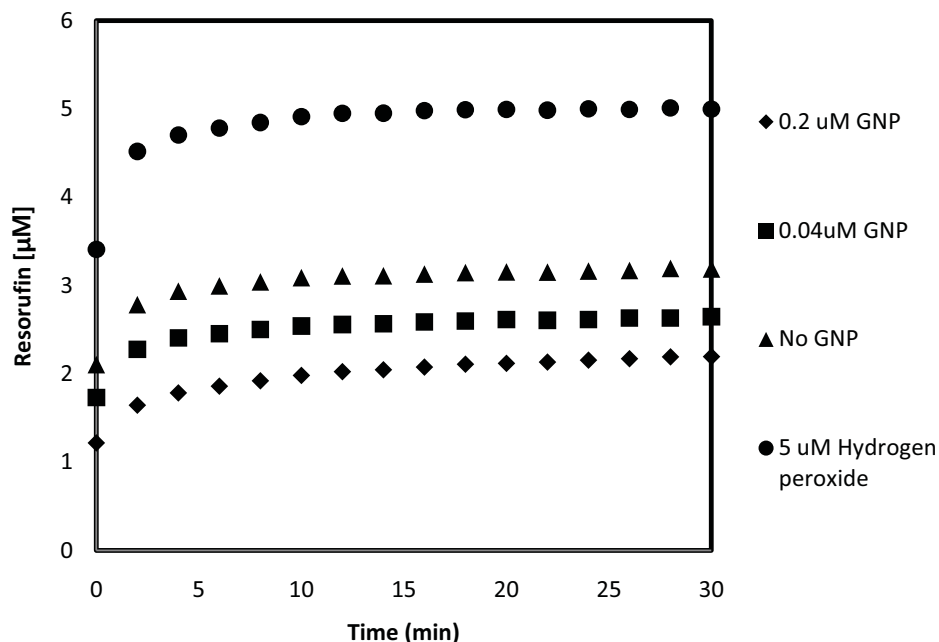


**Figure 4.8.** The effect of gold nanoparticle presence in Amplex Red assay with positive control (No GNP, 5  $\mu\text{M}$   $\text{H}_2\text{O}_2$ ) and negative control (No GNP and no  $\text{H}_2\text{O}_2$ ). The experimental samples containing gold nanoparticles at varying concentration have no  $\text{H}_2\text{O}_2$ . Each sample contains 1 U/mg of HRP.

absence of  $\text{H}_2\text{O}_2$  and HRP.  $\text{SnO}_2$  nanoparticle showed the highest conversion rate for this process. A similar trend is seen when these reactions are carried out in EMB media, a typical base medium used in cell culture. As might be expected, the amount of measurable  $\text{H}_2\text{O}_2$  is further reduced due to additional  $\text{H}_2\text{O}_2$  consuming reactions with molecules in the medium. The significance of this work is that care needs to be taken in interpreting the outcome of seemingly robust biochemical assays such as that of Amplex Red when they take place in the presence of nanoparticles, regardless whether in buffer or in cellular milieu. The extent of discrepancy between expected and measured  $\text{H}_2\text{O}_2$  in both cases was found to be a function of surface area and type of particle. The described approach for obtaining the actual concentration of  $\text{H}_2\text{O}_2$  in

the presence of metal oxide nanoparticles in spite of competing side reactions can be extended to other types of nanomaterials.

In the case of gold nanoparticles, Amplex Red assay appeared to protect the Amplex Red from non-H<sub>2</sub>O<sub>2</sub> driven resorufin formation that is usually seen in all samples even in the absence of H<sub>2</sub>O<sub>2</sub>. Further study is needed to determine if this is an effect of Amplex Red protection or HRP damage.

## CHAPTER 5

### CONCLUSION

In this thesis, we explored the synthesis of water-soluble and photoluminescence behavior red emitting (610 nm) gold nanoparticles terminated by mercaptoalkanoic acid and possessing UV range (200~350 nm) excitation. The samples were followed as a function of reaction condition including different gold and ligand concentrations, types of ligands, solvents and pH. Under the reaction

conditions, gold-thiol (LMMCT)  $\begin{matrix} \text{Au} \\ \uparrow \\ \text{Au} \end{matrix} \text{SR}$  complexes formed and developed into nanoparticle-supported complexes. Analyses of the excitation spectra suggests the origin of the photoluminescence to be transitions from the triplet energy state of LMMCT with the electrons transferred from excited orbitals of Au/Au(I) sites of the gold surface. It is also the reason for the enhanced photostability compared with those produced as free molecules via other synthesis methods. The stabilizing agent, mercaptoalkanoic acid, has one thiol and one carboxylic acid group at each end of a chemically inert octane backbone. The presence of the carboxylic acid groups of the gold nanoparticle provides us a possibility for further conjugation chemistry which would allow directing the gold nanoparticle to the specific target of interest as well as providing enough hydrophilicity of the resulting gold nanoparticle products. The salt-induced aggregation formation test showed that hydrophobicity of the surface stabilizing molecules plays an important role on its aggregation property with less

hydrophobic gold nanoparticles showed improved tolerance against aggregation by increased salt concentration possibly by less hydrophobic interaction between the particles.

The pH dependency of the gold nanoparticle's emission intensity and excitation spectra alteration was explored. The emission intensity of the gold nanoparticle showed linear dependency on the pH change in the weak acidic to basic region above the pH 6 with a small peak appearance at pH 4. This trend was accompanied by a distinctive excitation peak wavelength change from 280-290 nm to 250-260 nm at pH 6, near the  $pK_a$  value,  $\sim 5.5$ , of the gold nanoparticle solution. The  $pK_a$  of the carboxylic acid group is usually near pH 4.7~4.8 which is lower than gold nanoparticles. The shift of the isoelectric point of the carboxylic groups on the surface gold nanoparticles may be influenced by the electron-rich metallic surface.

A brush configuration change of the surface ligands was proposed. In the charged and extended form of the carboxylic acid ligands, the accessibility of water to the gold nanoparticles surface is greater than in the uncharged collapsed form. Thus, in the collapsed form, the local hydrophobicity at the gold surface is higher and the CT excitation spectrum shifts to the blue. In addition to this hypothesis, two other hypotheses have been proposed to explain the pH dependency on the emission and excitation spectra. Either of the hypotheses imposed the possibility of the energy level changes by suggesting the increased ground energy level caused by the shift of lower-energy sigma orbital at low pH to higher-energy nonbonding orbital at high pH and a new energy level formed at higher pH region by the bridging between the negatively charged oxygen and Au(I) atoms which eventually shows improved efficiency for the photoluminescent pathway. The Lippert-Mataga analysis was performed with combining the excitation results of different pH, solvent and ligand chain length. The

result showed that the solvent polarity was determined by the dipole moment change of -24 Debye between ground state and excited state with the MOA ligand which indicates the excited state is more polar than the absorbing ground state. The number of surface ligands bound on a particle was calculated by pH titration method and the result was 71 molecules per particle. This value is reasonable amount comparing to the known literature value.

Its biocompatibility, as suggested by the cytotoxicity test and Amplex Red test provides broader opportunities for this product to be utilized in biological systems. The Amplex Red study showed that the gold nanoparticles do not generate any ROS and even showed a possibility of lowering the pre-existing ROS in the control solution, although the mechanism for this is not fully understood.

The possibility that nanoparticles themselves may interact with the reagents and affect the accuracy of the measurement was examined using four different types of oxide nanoparticles, CeO<sub>2</sub>, Fe<sub>2</sub>O<sub>3</sub>, TiO<sub>2</sub> and SnO<sub>2</sub>. In some cases if they generate ROS themselves, a higher ROS content maybe detected. On the other hand if they have an antioxidant effect they may reduce the measurable ROS level. CeO<sub>2</sub>, Fe<sub>2</sub>O<sub>3</sub> and TiO<sub>2</sub> nanoparticles under-reported the actual H<sub>2</sub>O<sub>2</sub>, meanwhile SnO<sub>2</sub> nanoparticle had no such effect. Also, the result showed that all four types of the oxide nanoparticles has an ability to convert the Amplex Red molecule to resorufin for a “false” ROS signal while they underreports the presence of the ROS when they are mixed in the same solution.

In conclusion, from this project, we have developed the protocols to produce water-soluble photo-luminescent gold nanoparticles and the mechanism of the photo-luminescent process was proposed. However, there are some challenges to address for the improved product development. 1) During the synthesis process, overall yield of

the production is around 80% from the input gold chloride, confirmed by the ICP-MS. The loss of 20% could be minimized by reducing the formation of large and dark metallic pellets formed during the initial stirring process. These products are removed by the centrifugation at the beginning step of the purification. Better stirring stability and performance could be achieved by using improved stirring system including stir plates, bars and stable flasks which do not allow irregular stirring movement. This will also allow stabilized higher speed stirring during the synthesis. The current system does not allow stable stirring performance over 1000 rpm. The new test with better stirring system would be worth to try for the product improvement. 2) Our gold nanoparticle system only allows 610 nm emission and we have confirmed that it does not change its emission peak position regardless its size and types of surface ligand. It would further broaden the applicability of the product if the emission light is modifiable. Different dyes can be adsorbed or covalently bound to the surface of the gold nanoparticles to possibly modify the intrinsic 610 nm emission. 3) The DLS size of the gold nanoparticle is around 50~100 nm in diameter despite of the fact that the TEM size of the individual nanoparticle is 2.2 nm. The possible aggregation of the gold nanoparticles could be minimized if the hydrophilic moieties are introduced to the surface ligand. For example, PEG can be conjugated to the end surface ligand groups to reduce the hydrophobic interaction which causes the aggregation.

The developed protocol reproducibly generates pH dependent and photostable photoluminescent gold nanomaterials with low toxicity and water-solubility. To further demonstrate the biocompatibility of the product, the new cell viability test with blood cells such as hemoglobins and leukocytes. Leukocyte would be the first immunogenic system of the bloodstream that gold nanoparticle would actively be encountered when it is injected. Also, for the possible adhesion with the blood

proteins such as albumin, immunoglobulins and fibrinogens, the gold nanoparticles would be needed to be incubated with the blood proteins mentioned at the physiological concentrations and the basic properties and cytotoxicity could be tested for better understanding of the gold nanoparticle behavior in live human body.

This study is important for the use of fluorescence gold materials for bio-imaging, nano-pH sensing, and diagnostics. Potential applications for these widely Stokes shifted materials include two photon imaging and energy conversion. For this product to be used as a nano-pH sensor, it is required to maintain same local concentration of the product at the final destination. The uniform concentration could be achieved by encapsulating the gold nanoparticles into the optically transparent nanoshells. The surface of nanoshells should be conjugated with the targeting signal molecules. For other biomedical applications, the gold nanoparticles would be directly used with a proper surface modification with the targeting ligand would be needed.

## LITERATURE CITED

- [1]J.R. Lakowicz, Principles of Fluorescence Spectroscopy, Plenum Press, New York, 2006.
- [2]J. Sudimack, and R.J. Lee, Targeted Drug Delivery via the Folate Receptor. *Advanced Drug Delivery Reviews* 41 (2000) 147-162.
- [3]R. Novelline, Squire's Fundamentals of Radiology, Harvard University Press, 1997.
- [4]B. Kevles, Naked to the Bone Medical Imaging in the Twentieth Century, Rutgers University Press, Camden, NJ, 1996.
- [5]G. Herman, Fundamentals of Computerized Tomography: Image Reconstruction from Projection, Springer, 2009.
- [6]T. Terai, and T. Nagano, Fluorescent Probes for Bioimaging Applications. *Current Opinion in Chemical Biology* 12 (2008) 515-521.
- [7]N.J. Hangiandreou, AAPM/RSNA Physics Tutorial for Residents: Topics in US. *Radiographics* 23 (2003) 1019-1033.
- [8]U.N.R. Council, Health Risks from Low Levels of Ionizing Radiation, National Academy Press, 2006.
- [9]I.L. Medintz, H.T. Uyeda, E.R. Goldman, and H. Mattoussi, Quantum Dot Bioconjugates for Imaging, Labelling and Sensing. *Nature Materials* 4 (2005) 435-446.
- [10]M. Neumann, and D. Gabel, Simple Method for Reduction of Autofluorescence in Fluorescence Microscopy. *Journal of Histochemistry and Cytochemistry* 50 (2002) 437-439.
- [11]D. Mizrahi, and M. Shemesh, Follicle-Stimulating Hormone Receptor and Its Messenger Ribonucleic Acid Are Present in the Bovine Cervix and Can Regulate Cervical Prostanoid Synthesis. *Biology of Reproduction* 61 (1999) 776-784.
- [12]G.G. Guilbault, Practical Fluorescence, Marcel Dekker, Inc., New York, 1990.
- [13]X. Wu, H. Liu, J. Liu, K.N. Haley, J.A. Treadway, J.P. Larson, N. Ge, F. Peale, and M.P. Bruchez, Immunofluorescent Labeling of Cancer Marker Her2 and

- Other Cellular Targets with Semiconductor Quantum Dots. *Nature Biotechnology* 21 (2003) 41-46.
- [14]R. Gill, M. Zayats, and I. Willner, Semiconductor Quantum Dots for Bioanalysis. *Angewandte Chemie International Edition* 47 (2008) 7602-7625.
- [15]H. Arya, Z. Kaul, R. Wadhwa, K. Taira, T. Hirano, and S.C. Kaul, Quantum Dots in Bio-Imaging: Revolution by the Small. *Biochemical and Biophysical Research Communications* 329 (2005) 1173-1177.
- [16]C.B. Murray, C.R. Kagan, and M.G. Bawendi, Synthesis and Characterization of Monodisperse Nanocrystals and Close-packed Nanocrystal Assemblies. *Annual Review of Materials Science* 30 (2003) 545-610.
- [17]X. Gao, L. Yang, J. Petros, F. Marshall, J. Simons, and S. Nie, In vivo Molecular and Cellular Imaging with Quantum Dots. *Current Opinion in Biotechnology* 16 (2005) 63-72.
- [18]W.C.W. Chan, D.J. Maxwell, X. Gao, R.E. Bailey, M. Han, and S. Nie, Luminescent Quantum Dots for Multiplexed Biological Detection and Imaging. *Current Opinion in Biotechnology* 13 (2002) 40-46.
- [19]E. Tholouli, E. Sweeney, E. Barrow, V. Clay, J. Hoyland, and R. Byers, Quantum Dots Light Up Pathology. *The Journal of Pathology* 216 (2008) 275-285.
- [20]J. Lovric, S.J. Cho, F.M. Winnik, and D. Maysinger, Unmodified Cadmium Telluride Quantum Dots Induce Reactive Oxygen Species Formation Leading to Multiple Organelle Damage and Cell Death. *Chemistry and Biology* 12 (2005) 1227-1234.
- [21]S.J. Cho, D. Maysinger, M. Jain, B. Roder, S. Hackbarth, and F.M. Winnik, Long-Term Exposure to CdTe Quantum Dots Causes Functional Impairments in Live Cells. *Langmuir* 23 (2007) 1974-1980.
- [22]K. Nogawa, E. Kobayashi, Y. Okubo, and Y. Suwazono, Environmental Cadmium Exposure, Adverse Effects and Preventive Measures in Japan. *BioMetals* 17 (2004) 581-587.
- [23]A. Hartwig, Role of DNA Repair Inhibition in Lead- and Cadmium-induced Genotoxicity: A Review. *Environmental Health Perspect* 102 (1994) 45-50.
- [24]U. Lindh, Cell Biology, Trace Elements and Nuclear Microscopy. *Nuclear Instruments and Methods in Physics Research Section B: Beam Interactions with Materials and Atoms* 104 (1995) 285-291.
- [25]J. Carmichael, W.G. DeGraff, A.F. Gazdar, J.D. Minna, and J.B. Mitchell, Evaluation of a Tetrazolium-based Semiautomated Colorimetric Assay: Assessment of Chemosensitivity Testing. *Cancer Research* 47 (1987) 936-942.

- [26]E. Connor, J. Mwamuka, A. Gole, C. Murphy, and M. Wyatt, Gold Nanoparticles Are Taken Up by Human Cells but Do Not Cause Acute Cytotoxicity. *Small* 1 (2005) 325-327.
- [27]M.A. Alaaldin, K.N. Pratik, R.H. Cole, J.S. Timothy, J.M. Catherine, and D.W. Michael, Cellular Uptake and Cytotoxicity of Gold Nanorods: Molecular Origin of Cytotoxicity and Surface Effects. *Small* 5 (2009) 701-708.
- [28]P. Calamai, S. Carotti, A. Guerri, T. Mazzei, L. Messori, E. Mini, P. Orioli, and G. Speroni, Cytotoxic Effects of Gold(III) Complexes on Established Human Tumor Cell Lines Sensitive and Resistant to Cisplatin. *Anticancer Drug Design* 13 (1998) 67-80.
- [29]S. Berciaud, L. Cognet, P. Tamarat, and B. Lounis, Observation of Intrinsic Size Effects in the Optical Response of Individual Gold Nanoparticles. *Nano Letters* 5 (2005) 515-518.
- [30]H. Cui, Z.F. Zhang, and M.J. Shi, Chemiluminescent Reactions Induced by Gold Nanoparticles. *Journal of Physical Chemistry B* 109 (2005) 3099-3103.
- [31]T. Huang, and R.W. Murray, Visible Luminescence of Water-Soluble Monolayer-Protected Gold Clusters. *Journal of Physical Chemistry B* 105 (2001) 12498-12502.
- [32]J. Zheng, P.R. Nicovich, and R.M. Dickson, Highly Fluorescent Noble-Metal Quantum Dots. *Annual Review of Physical Chemistry* 58 (2007) 409-431.
- [33]R.B. Wyrwas, M.M. Alvarez, J.T. Khoury, R.C. Price, T.G. Schaaff, and R.L. Whetten, The colours of nanometric gold. *The European Physical Journal D - Atomic, Molecular and Optical Physics* 43 (2007) 91-95.
- [34]Y.N. Hwang, D.H. Jeong, H.J. Shin, D. Kim, S.C. Jeung, S.H. Han, J.S. Lee, and G. Cho, Femtosecond Emission Studies on Gold Nanoparticles. *Journal of Physical Chemistry B* 106 (2002) 7581-7584.
- [35]J.P. Wilcoxon, and J.E. Martin, Photoluminescence from Nanosize Gold Clusters. *Journal of Chemical Physics* 108 (1998) 9137.
- [36]K. Sokolov, M. Follen, J. Aaron, I. Pavlova, A. Malpica, R. Lotan, and R. Richards-Kortum, Real-Time Vital Optical Imaging of Precancer Using Anti-Epidermal Growth Factor Receptor Antibodies Conjugated to Gold Nanoparticles. *Cancer Research* 63 (2003) 1999-2004.
- [37]R. Bhattacharya, C.R. Patra, A. Earl, S. Wang, A. Katarya, L. Lu, J.N. Kizhakkedathu, M.J. Yaszemski, P.R. Greipp, D. Mukhopadhyay, and P. Mukherjee, Attaching Folic Acid on Gold Nanoparticles Using Noncovalent Interaction Via Different Polyethylene Glycol Backbones and Targeting of Cancer Cells. *Nanomedicine: Nanotechnology, Biology and Medicine* 3 (2007) 224-238.

- [38]G. Yin, S. Wang, M. Xu, and L. Chen, Theoretical Calculation of the Optical Properties of Gold Nanoparticles. *Journal of the Korean Physical Society* 49 (2006) 2108-2111.
- [39]P.K. Jain, I.H. El-Sayed, and M.A. El-Sayed, Au Nanoparticles Target Cancer. *Nano Today* 2 (2007) 18-29.
- [40]J.K. Lim, and S.-W. Joo, Gold Nanoparticle-Based pH Sensor in Highly Alkaline Region at pH 11: Surface-Enhanced Raman Scattering Study. *Applied Spectroscopy* 60 (2006) 847-852.
- [41]J.H. Kim, and T.R. Lee, Thermo- and pH-Responsive Hydrogel-Coated Gold Nanoparticles. *Chemistry of Materials* 16 (2004) 3647-3651.
- [42]G. Mihailescu, L. Olenic, S. Pruneanu, I. RBratu, and I. Kacso, The Effect of pH on Amino Acids Binding to Gold Nanoparticles. *Journal of Optoelectronics and Advanced Materials* 9 (2007) 756-759.
- [43]T. Ahmadi, S. Logunov, and M. El-Sayed, Size-Dependent Electron Dynamics of Gold Nanoparticles, *Nanostructured Materials*, American Chemical Society, Washington, DC, 1997, pp. 125-140.
- [44]P. Sharma, S. Brown, G. Walter, S. Santra, and B. Moudgil, Nanoparticles for bioimaging. *Advances in Colloid and Interface Science* 123-126 (2006) 471-485.
- [45]G. Raschke, S. Kowarik, T. Franzl, C. Sonnichsen, T.A. Klar, J. Feldmann, A. Nichtl, and K. Kurzinger, Biomolecular Recognition Based on Single Gold Nanoparticle Light Scattering. *Nano Letters* 3 (2003) 935-938.
- [46]P. Montcourrier, P.H. Mangeat, C. Valembois, G. Salazar, A. Sahuquet, C. Duperray, and H. Rochefort, Characterization of Very Acidic Phagosomes in Breast Cancer Cells and Their Association with Invasion. *Journal of Cellular Science* 107 (1994) 2381-2391.
- [47]V. Yam, E. Cheng, and K. Cheung, A Novel High-Nuclearity Luminescent Gold(I)-Sulfido Complex. *Angewandte Chemie International Edition* 38 (1999) 197-199.
- [48]S.-H. Cha, J.-U. Kim, K.-H. Kim, and J.-C. Lee, Preparation and Photoluminescent Properties of Gold(I)-Alkanethiolate Complexes Having Highly Ordered Supramolecular Structures. *Chemistry of Materials* 19 (2007) 6297-6303.
- [49]R.L. White-Morris, M.M. Olmstead, A.L. Balch, O. Elbjeirami, and M.A. Omary, Orange Luminescence and Structural Properties of Three Isostructural Halocyclohexylisonitrilegold(I) Complexes. *Inorganic Chemistry* 42 (2003) 6741-6748.

- [50]V. Yam, E. Cheng, and Z. Zhou, A Highly Soluble Luminescent Decanuclear Gold(I) Complex with a Propeller-Shaped Structure. *Angewandte Chemie International Edition* 39 (2000) 1683-1685.
- [51]H. Kunkely, and A. Vogler, Contrasting Photochemical Behavior of  $[\text{Au}(\text{SH})_2]$ - and  $\text{Au}(\text{SMe}_2)\text{Cl}$ . *Journal of Photochemistry and Photobiology A: Chemistry* 105 (1997) 7-10.
- [52]A. Vogler, and H. Kunkely, Photoreactivity of Gold Complexes. *Coordination Chemistry Reviews* 219-221 (2001) 489-507.
- [53]A.S. Susha, M. Ringler, A. Ohlinger, M. Paderi, N. LiPira, G. Carotenuto, A.L. Rogach, and J. Feldmann, Strongly Luminescent Films Fabricated by Thermolysis of Gold-Thiolate Complexes in a Polymer Matrix. *Chemistry of Materials* 20 (2008) 6169-6175.
- [54]M. Bardaji, M.J. Calhorda, P.J. Costa, P.G. Jones, A. Laguna, M. Reyes Perez, and M.D. Villacampa, Synthesis, Structural Characterization, and Theoretical Studies of Gold(I) and Gold(I)-Gold(III) Thiolate Complexes: Quenching of Gold(I) Thiolate Luminescence. *Inorganic Chemistry* 45 (2006) 1059-1068.
- [55]W.B. Jones, B.J. Yuan, R. Narayanaswamy, M.A. Young, R.C. Elder, A.E. Bruce, and M.R.M. Bruce, Solid State EXAFS and Luminescence Studies of Neutral, Dinuclear Gold(I) Complexes. *Gold(I)-Gold(I) Interactions in the Solid State. Inorganic Chemistry* 34 (1995) 1996-2001.
- [56]B. Tzeng, C. Chan, K. Cheung, C. Che, and S. Peng, Dramatic Solvent Effect on the Luminescence of a Dinuclear Gold(I) Complex of Quinoline-8-thiolate. *Chemistry Communications* (1997) 135-136.
- [57]W. Harbich, Optical Spectroscopy on Size Selected Gold Clusters Deposited in Rare Gas Matrixes. *Zeitschrift für Physik. D, Atoms, Molecules, and Clusters* 19 (1991) 157.
- [58]S. Link, A. Beeby, S. FitzGerald, M.A. El-Sayed, T.G. Schaaff, and R.L. Whetten, Visible to Infrared Luminescence from a 28-Atom Gold Cluster. *Journal of Physical Chemistry B* 106 (2002) 3410-3415.
- [59]S. Fedrigo, W. Harbich, and J. Buttet, Optical Response of  $\text{Ag}_2$ ,  $\text{Ag}_3$ ,  $\text{Au}_2$ , and  $\text{Au}_3$  in Argon Matrices. *Journal of Chemical Physics* 99 (1993) 5712.
- [60]J. Zheng, C. Zhang, and R.M. Dickson, Highly Fluorescent, Water-Soluble, Size-Tunable Gold Quantum Dots. *Physical Review Letters* 93 (2004) 077402.
- [61]Y. Bao, C. Zhong, D.M. Vu, J.P. Temirov, R.B. Dyer, and J.S. Martinez, Nanoparticle-Free Synthesis of Fluorescent Gold Nanoclusters at Physiological Temperature. *The Journal of Physical Chemistry C* 111 (2007) 12194-12198.

- [62]C. Huang, Z. Yang, K. Lee, and H. Chang, Synthesis of Highly Fluorescent Gold Nanoparticles for Sensing Mercury(II). *Angewandte Chemie International Edition* 46 (2007) 6824-6828.
- [63]J. Xie, Y. Zheng, and J.Y. Ying, Protein-Directed Synthesis of Highly Fluorescent Gold Nanoclusters. *Journal of the American Chemical Society* 131 (2009) 888-889.
- [64]Y. Negishi, K. Nobusada, and T. Tsukuda, Glutathione-Protected Gold Clusters Revisited: Bridging the Gap between Gold(I)-Thiolate Complexes and Thiolate-Protected Gold Nanocrystals. *Journal of the American Chemical Society* 127 (2005) 5261-5270.
- [65]B. Tzeng, C. Chan, K. Cheung, C. Che, and S. Peng, Dramatic Solvent Effect on the Luminescence of a Dinuclear Gold(I) Complex of Quinoline-8-thiolate. *Chemistry Communications* (1997) 135-136.
- [66]R.E. Bachman, S.A. Bodolosky-Bettis, S.C. Glennon, and S.A. Sirchio, Formation of a Novel Luminescent Form of Gold(I) Phenylthiolate via Self-Assembly and Decomposition of Isonitrilegold(I) Phenylthiolate Complexes. *Journal of the American Chemical Society* 122 (2000) 7146-7147.
- [67]P. Pekka, Theoretical Chemistry of Gold. *Angewandte Chemie International Edition* 43 (2004) 4412-4456.
- [68]J. Zhang, J.K. Whitesell, and M.A. Fox, Photophysical Behavior of Various Sized Colloidal Gold Clusters Capped with Monolayers of an Alkylstilbenethiolate. *The Journal of Physical Chemistry B* 107 (2003) 6051-6055.
- [69]Y. Negishi, Y. Takasugi, S. Sato, H. Yao, K. Kimura, and T. Tsukuda, Magic-Numbered Au Clusters Protected by Glutathione Monolayers ( $n = 18, 21, 25, 28, 32, 39$ ): Isolation and Spectroscopic Characterization. *Journal of the American Chemical Society* 126 (2004) 6518-6519.
- [70]Y. Negishi, and T. Tsukuda, One-Pot Preparation of Subnanometer-Sized Gold Clusters via Reduction and Stabilization by meso-2,3-Dimercaptosuccinic Acid. *Journal of the American Chemical Society* 125 (2003) 4046-4047.
- [71]A. Longo, G.P. Pepe, G. Carotenuto, A. Ruotolo, S.D. Nicola, V.I. Belotelov, and A.K. Zvezdin, Optical Emission Studies in Au/Ag Nanoparticles. *Nanotechnology* 18 (2007) 365701.
- [72]J. Zheng, Fluorescent Noble Metal Nanoclusters. Ph.D. Thesis, Georgia Institute of Technology (2005).
- [73]P. Hawkes, *The beginnings of Electron Microscopy*, Academic Press, 1985.
- [74]B. Frisken, Revisiting the Method of Cumulants for the Analysis of Dynamic Light Scattering Data. *Applied Optics* 40 (2001) 4087-4091.

- [75]R. Hunter, Foundations of Colloid Science, Oxford University Press, 1989.
- [76]S.S. Kannamkumarath, K. Wrobel, K. Wrobel, C. B'Hymer, and J.A. Caruso, Capillary Electrophoresis-Inductively Coupled Plasma-Mass Spectrometry: An Attractive Complementary Technique for Elemental Speciation Analysis. *Journal of Chromatography A* 975 (2002) 245-266.
- [77]J. Pople, Publisher's note: Sir John A. Pople, 1925-2004. *Journal of Computational Chemistry* 25 (2004) fmv-viii.
- [78]C. Maurizio, R. Nadia, S. Giovanni, and B. Vincenzo, Energies, Structures, and Electronic Properties of Molecules in Solution with the C-PCM Solvation Model. *Journal of Computational Chemistry* 24 (2003) 669-681.
- [79]J. Kimling, M. Maier, B. Okenve, V. Kotaidis, H. Ballot, and A. Plech, Turkevich Method for Gold Nanoparticle Synthesis Revisited. *The Journal of Physical Chemistry B* 110 (2006) 15700-15707.
- [80]J.D.S. Newman, and G.J. Blanchard, Formation of Gold Nanoparticles Using Amine Reducing Agents. *Langmuir* 22 (2006) 5882-5887.
- [81]J.M. Veranth, C.A. Reilly, M.M. Veranth, T.A. Moss, C.R. Langelier, D.L. Lanza, and G.S. Yost, Inflammatory Cytokines and Cell Death in BEAS-2B Lung Cells Treated with Soil Dust, Lipopolysaccharide, and Surface-Modified Particles. *Toxicological Science* 82 (2004) 88-96.
- [82]C.J. Mathias, S. Wang, R.J. Lee, D.J. Waters, P.S. Low, and M.A. Green, Tumor-Selective Radiopharmaceutical Targeting via Receptor-Mediated Endocytosis of Gallium-67-Deferoxamine-Folate. *Journal of Nuclear Medicine* 37 (1996) 1003-1008.
- [83]I.G. Campbell, T.A. Jones, W.D. Foulkes, and J. Trowsdale, Folate-binding Protein Is a Marker for Ovarian Cancer. *Cancer Research* 51 (1991) 5329-5338.
- [84]L.R. Coney, A. Tomassetti, L. Carayannopoulos, V. Frasca, B.A. Kamen, M.I. Colnaghi, and V.R. Zurawski, Jr., Cloning of a Tumor-associated Antigen: MOv18 and MOv19 Antibodies Recognize a Folate-binding Protein. *Cancer Research* 51 (1991) 6125-6132.
- [85]T. Akita, M. Okumura, K. Tanaka, M. Kohyama, and M. Haruta, TEM Observation of Gold Nanoparticles Deposited on Cerium Oxide. *Journal of Materials Science* 40 (2005) 3101-3106.
- [86]I. Hussain, S. Graham, Z. Wang, B. Tan, D.C. Sherrington, S.P. Rannard, A.I. Cooper, and M. Brust, Size-Controlled Synthesis of Near-Monodisperse Gold Nanoparticles in the 1-4 nm Range Using Polymeric Stabilizers. *Journal of the American Chemical Society* 127 (2005) 16398-16399.

- [87]D. Lee, R.L. Donkers, G. Wang, A.S. Harper, and R.W. Murray, Electrochemistry and Optical Absorbance and Luminescence of Molecule-like Au<sub>38</sub> Nanoparticles. *Journal of the American Chemical Society* 126 (2004) 6193-6199.
- [88]J.C. Ehrhardt, and S.P. Davis, Precision Wavelengths and Energy Levels in Gold. *Journal of Optical Society of America* 61 (1971) 1342-1349.
- [89]D.C. Morton, Atomic Data for Resonance Absorption Lines. II. Wavelengths Longward of the Lyman Limit for Heavy Elements. *The Astrophysical Journal Supplement Series* 130 (2000) 403-436.
- [90]M. Rosberg, and J.-F. Wyart, The Spectrum of Singly Ionized Gold, Au II. *Physica Scripta* 55 (1997) 690-706.
- [91]Q.-J. Pan, and H.-X. Zhang, Ab Initio Studies on Metal-Metal Interaction and 3[σ\*(d)σ(s)] Excited State of the Binuclear Au(I) Complexes Formed by Phosphine and/or Thioether Ligands. *The Journal of Physical Chemistry A* 108 (2004) 3650-3661.
- [92]Y. Chi, F. Li-Min, W. Yuan, Z. Jian-Ping, W. Wing-Tak, A. Xi-Cheng, Q. Yi-Fang, Z. Bing-Suo, and G. Lin-Lin, A Highly Luminescent Europium Complex Showing Visible-Light-Sensitized Red Emission: Direct Observation of the Singlet Pathway<sup>13</sup>. *Angewandte Chemie* 116 (2004) 5120-5123.
- [93]T. Cheng, Y. Zhao, X. Li, F. Lin, Y. Xu, X. Zhang, Y. Li, R. Wang, and L. Lai, Computation of Octanol-Water Partition Coefficients by Guiding an Additive Model with Knowledge. *Journal of Chemical Information and Modeling* 47 (2007) 2140-2148.
- [94]N. Ise, and I. Sogami, *Structure Formation in Solution: Ionic Polymers and Colloidal Particles*, Springer Berlin Heidelberg, New York, 2005.
- [95]A. Gole, C. Ganpule, R. Pasrichal, and M. Sastry, Quasi-linear Assemblies of Silver Nanoparticles by Highly Localized Anodic Dissolution of Copper in Hydrosol. *Journal of Nanoscience and Nanotechnology* 2 (2002) 147-150.
- [96]I.R. Hong, and Y.J. Kim, Self-aggregated Nanoparticles of Lipoic Acid Conjugated Hyaluronic Acid. *Polymer* 32 (2008) 561-565.
- [97]C. Goncalves, and F.M. Gama, Characterization of the Self-assembly Process of Hydrophobically Modified Dextrin. *European Polymer Journal* 44 (2008) 3529-3534.
- [98]K. Culha, M. Kahraman, N. Tokman, and G. Turkoglu, Surface-Enhanced Raman Scattering on Aggregates of Silver Nanoparticles with Definite Size. *The Journal of Physical Chemistry C* 112 (2008) 10338-10343.

- [99]X. Ji, X. Song, J. Li, Y. Bai, W. Yang, and X. Peng, Size Control of Gold Nanocrystals in Citrate Reduction: The Third Role of Citrate. *Journal of the American Chemical Society* 129 (2007) 13939-13948.
- [100]S. Kumar, K.S. Gandhi, and R. Kumar, Modeling of Formation of Gold Nanoparticles by Citrate Method. *Industrial & Engineering Chemistry Research* 46 (2006) 3128-3136.
- [101]J. Turkevich, P. Stevenson, and J. Hillier, A Study of the Nucleation and Growth Processes in the Synthesis of Colloidal Gold. *Discuss. Faraday Society* 11 (1951) 55-75.
- [102]C.-t.F. Lo, K. Karan, and B.R. Davis, Kinetic Studies of Reaction between Sodium Borohydride and Methanol, Water, and Their Mixtures. *Industrial & Engineering Chemistry Research* 46 (2007) 5478-5484.
- [103]H.I. Schlesinger, H.C. Brown, A.E. Finholt, J.R. Gilbreath, H.R. Hoekstra, and E.K. Hyde, Sodium Borohydride, Its Hydrolysis and its Use as a Reducing Agent and in the Generation of Hydrogen<sup>1</sup>. *Journal of the American Chemical Society* 75 (1953) 215-219.
- [104]P. Westerhoff, Reduction of Nitrate, Bromate, and Chlorate by Zero Valent Iron (Fe<sup>0</sup>). *Journal of Environmental Engineering* 129 (2003) 10-16.
- [105]M.J. Hostetler, J.E. Wingate, C.-J. Zhong, J.E. Harris, R.W. Vachet, M.R. Clark, J.D. Londono, S.J. Green, J.J. Stokes, G.D. Wignall, G.L. Glish, M.D. Porter, N.D. Evans, and R.W. Murray, Alkanethiolate Gold Cluster Molecules with Core Diameters from 1.5 to 5.2 nm:Core and Monolayer Properties as a Function of Core Size. *Langmuir* 14 (1998) 17-30.
- [106]M. Brust, J. Fink, D. Bethell, D. Schiffrin, and C. Kiely, Synthesis and Reactions of Functionalised Gold Nanoparticles. *Journal of Chemical Society, Chemical Communications* (1995) 1655-1656.
- [107]M. Brust, M. Walker, D. Bethell, D. Schiffrin, and R. Whyman, Synthesis of Thiol-derivatised Gold Nanoparticles in a Two-phase Liquid-liquid System. *Chemical Communications* (1994) 801-802.
- [108]S.G. Schulman, *Fluorescence and Phosphorescence Spectroscopy: Physico-chemical Principles and Practice*, Pergamon Press, Oxford, 1977.
- [109]A. Eychmuller, A. Hasselbarth, L. Katsikas, and H. Weller, Photochemistry of Semiconductor Colloids .36. Fluorescence Investigations on the Nature of Electron and Hole Traps in Q-sized Colloidal Cds Particles. *Berichte Der Bunsen-Gesellschaft-Physical Chemistry Chemical Physics* 95 (1991) 79-84.
- [110]M. Kaschke, N.P. Ernsting, U. Moller, and H. Weller, Ultrafast Electron Ejection and Trapping in Semiconductor Colloids After Multiple Photon Absorption. *Chemical Physics Letters* 168 (1990) 543-550.

- [111]T.-C. Liu, Z.-L. Huang, H.-Q. Wang, J.-H. Wang, X.-Q. Li, Y.-D. Zhao, and Q.-M. Luo, Temperature-dependent Photoluminescence of Water-soluble Quantum Dots for a Bioprobe. *Analytica Chimica Acta* 559 (2006) 120-123.
- [112]T.C.M. Graham, B. Urbaszek, X. Tang, C. Bradford, K.A. Prior, B.C. Cavenett, and R.J. Warburton, Temperature dependent photoluminescence of CdSe quantum dots grown in MgS and ZnSe. *Physica Status Solidi (c)* 1 (2004) 755-758.
- [113]W.J. Parak, T. Pellegrino, and C. Plank, Labelling of Cells with Quantum Dots. *Nanotechnology* 16 (2005) R9-R25.
- [114]E. Demann, P. Stein, and J. Haubenrich, Gold as an Implant in Medicine and Dentistry. *Journal of Long-Term Effects of Medical Implants* 15 (2005) 687-698.
- [115]C.M. Goodman, C.D. McCusker, T. Yilmaz, and V.M. Rotello, Toxicity of Gold Nanoparticles Functionalized with Cationic and Anionic Side Chains. *Bioconjugate Chemistry* 15 (2004) 897-900.
- [116]S. Harper, C. Usenko, J.E. Hutchison, B.L.S. Maddux, and R.L. Tanguay, In vivo Biodistribution and Toxicity Depends on Nanomaterial Composition, Size, Surface Functionalisation and Route of Exposure. *Journal of Experimental Nanoscience* 3 (2008) 195 - 206.
- [117]J. Zhou, J. Ralston, R. Sedev, and D.A. Beattie, Functionalized gold Nanoparticles: Synthesis, Structure and Colloid Stability. *Journal of Colloid and Interface Science* 331 (2009) 251-262.
- [118]D. Shalom, R.C.R. Wootton, R.F. Winkle, B.F. Cottam, R. Vilar, A.J. deMello, and C.P. Wilde, Synthesis of Thiol Functionalized Gold Nanoparticles Using a Continuous Flow Microfluidic Reactor. *Materials Letters* 61 (2007) 1146-1150.
- [119]M. Ozkan, Quantum Dots and Other Nanoparticles: What Can They Offer to Drug Discovery? *Drug Discovery Today* 9 (2004) 1065-1071.
- [120]C.J. Murphy, T.K. Sau, A.M. Gole, C.J. Orendorff, J. Gao, L. Gou, S.E. Hunyadi, and T. Li, Anisotropic Metal Nanoparticles: Synthesis, Assembly, and Optical Applications. *The Journal of Physical Chemistry B* 109 (2005) 13857-13870.
- [121]A. Lu, E. Salabas, and S. Ferdi, Magnetic Nanoparticles: Synthesis, Protection, Functionalization, and Application. *Angewandte Chemie International Edition* 46 (2007) 1222-1244.
- [122]Y. Shen, M. Kuang, Z. Shen, J. Nieberle, H. Duan, and H. Frey, Gold Nanoparticles Coated with a Thermosensitive Hyperbranched Polyelectrolyte: Towards Smart Temperature and pH Nanosensors. *Angewandte Chemie International Edition* 47 (2008) 2227-2230.

- [123]I. Tokareva, S. Minko, J.H. Fendler, and E. Hutter, Nanosensors Based on Responsive Polymer Brushes and Gold Nanoparticle Enhanced Transmission Surface Plasmon Resonance Spectroscopy. *Journal of the American Chemical Society* 126 (2004) 15950-15951.
- [124]F. Gao, L. Wang, L. Tang, and C. Zhu, A Novel Nano-Sensor Based on Rhodamine- $\beta$ -Isothiocyanate – Doped Silica Nanoparticle for pH Measurement. *Microchimica Acta* 152 (2005) 131-135.
- [125]J. Peng, X. He, K. Wang, W. Tan, Y. Wang, and Y. Liu, Noninvasive Monitoring of Intracellular pH Change Induced by Drug Stimulation Using Silica Nanoparticle Sensors. *Analytical and Bioanalytical Chemistry* 388 (2007) 645-654.
- [126]M. Kneen, J. Farinas, Y. Li, and A.S. Verkman, Green Fluorescent Protein as a Noninvasive Intracellular pH Indicator. *Biophysics J.* 74 (1998) 1591-1599.
- [127]R.A. Cardullo, and S. Dandala, Correcting for Artifacts in Complex Aqueous Solutions When Using the pH-Sensitive Dye 2',7'-Bis-(2-carboxyethyl)-5-(and -6)carboxyfluorescein. *Analytical Biochemistry* 267 (1999) 351-356.
- [128]N. Boens, W. Qin, N. Basaric, A. Orte, E.M. Talavera, and J.M. Alvarez-Pez, Photophysics of the Fluorescent pH Indicator BCECF. *The Journal of Physical Chemistry A* 110 (2006) 9334-9343.
- [129]R.C. Hunter, and T.J. Beveridge, Application of a pH-Sensitive Fluoroprobe (C-SNARF-4) for pH Microenvironment Analysis in *Pseudomonas aeruginosa* Biofilms. *Applications in Environmental Microbiology* 71 (2005) 2501-2510.
- [130]J.E. Whitaker, R.P. Haugland, and F.G. Prendergast, Spectral and Photophysical Studies of Benzo[c]xanthene Dyes: Dual Emission pH Sensors. *Analytical Biochemistry* 194 (1991) 330-344.
- [131]G.T. Hanson, T.B. McAnaney, E.S. Park, M.E.P. Rendell, D.K. Yarbrough, S. Chu, L. Xi, S.G. Boxer, M.H. Montrose, and S.J. Remington, Green Fluorescent Protein Variants as Ratiometric Dual Emission pH Sensors. 1. Structural Characterization and Preliminary Application. *Biochemistry* 41 (2002) 15477-15488.
- [132]G. Nishimura, Y. Shiraishi, and T. Hirai, A Fluorescent Chemosensor for Wide-range pH Detection. *Chemical Communications* (2005) 5313-5315.
- [133]N.i. Saleh, Y.A. Al-Soud, and W.M. Nau, Novel Fluorescent pH Sensor Based on Coumarin with Piperazine and Imidazole Substituents. *Spectrochimica Acta Part A: Molecular and Biomolecular Spectroscopy* 71 (2008) 818-822.
- [134]B.H. McNaughton, J.N. Anker, and R. Kopelman, Magnetic Microdrill as a Modulated Fluorescent pH Sensor. *Journal of Magnetism and Magnetic Materials* 293 (2005) 696-701.

- [135]E.U. Akkaya, M.E. Huston, and A.W. Czarnik, Chelation-enhanced Fluorescence of Anthrylazamacrocycle Conjugate Probes in Aqueous Solution. *Journal of the American Chemical Society* 112 (1990) 3590-3593.
- [136]Y. Xu, Y. Liu, and X. Qian, Novel Cyanine Dyes as Fluorescent pH Sensors: PET, ICT Mechanism or Resonance Effect? *Journal of Photochemistry and Photobiology A: Chemistry* 190 (2007) 1-8.
- [137]M. Tomasulo, I. Yildiz, and F.M. Raymo, pH-Sensitive Quantum Dots. *The Journal of Physical Chemistry B* 110 (2006) 3853-3855.
- [138]R. Shukla, V. Bansal, M. Chaudhary, A. Basu, R.R. Bhonde, and M. Sastry, Biocompatibility of Gold Nanoparticles and Their Endocytotic Fate Inside the Cellular Compartment: A Microscopic Overview. *Langmuir* 21 (2005) 10644-10654.
- [139]J.L. West, and N.J. Halas, Engineered Nanomaterials for Biophotonics for Biophotonics Applications: Improving Sensing, Imaging, and Therapeutics. *Annual Review of Biomedical Engineering* 5 (2003) 285-292.
- [140]S.A. Maier, and H.A. Atwater, Plasmonics: Localization and Guiding of Electromagnetic Energy in Metal/Dielectric Structures. *Journal of Applied Physics* 98 (2005) 011101.
- [141]O. Kwon, A. Kikuchi, M. Yamato, Y. Sakurai, and T. Okano, Rapid Cell Sheet Detachment from Poly(N-isopropylacrylamide)-grafted Porous Cell Culture Membranes. *Journal of Biomedical Materials Research* 50 (2000) 82-89.
- [142]T. Okamoto, and I. Yamaguchi, Optical Absorption Study of the Surface Plasmon Resonance in Gold Nanoparticles Immobilized onto a Gold Substrate by Self-Assembly Technique. *The Journal of Physical Chemistry B* 107 (2003) 10321-10324.
- [143]V. Kozlovskaya, E. Kharlampieva, B.P. Khanal, P. Manna, E.R. Zubarev, and V.V. Tsukruk, Ultrathin Layer-by-Layer Hydrogels with Incorporated Gold Nanorods as pH-Sensitive Optical Materials. *Chemistry of Materials* 20 (2008) 7474-7485.
- [144]I. Tokarev, I. Tokareva, and S. Minko, Gold-Nanoparticle-Enhanced Plasmonic Effects in a Responsive Polymer Gel. *Advanced Materials* 20 (2008) 2730-2734.
- [145]J. Homola, Surface Plasmon Resonance Sensors for Detection of Chemical and Biological Species. *Chemical Reviews* 108 (2008) 462-493.
- [146]C. Campbell, and G. Kim, SPR Microscopy and Its Applications to High-throughput Analyses of Biomolecular Binding Events and Their Kinetics. *Biomaterials* 28 (2007) 2380-2392.

- [147]Y. Shiraishi, D. Arakawa, and N. Toshima, pH-dependent Color Change of Colloidal Dispersions of Gold Nanoclusters: Effect of Stabilizer. *The European Physical Journal E: Soft Matter and Biological Physics* 8 (2002) 377-383.
- [148]W. Patungwasa, and J. Hodak, pH Tunable Morphology of the Gold Nanoparticles Produced by Citrate Reduction. *Materials Chemistry and Physics* 108 (2007) 45-54.
- [149]X. Liu, F. Cheng, W. Liu, W. Li, Y. Chen, H. Pan, and H. Liu, Thermoresponsive Gold Nanoparticles with Adjustable Lower Critical Solution Temperature as Colorimetric Sensors for Temperature, pH and Salt Concentration. *Journal of Material Chemistry* 20 (2010) 278-284.
- [150]B. Panda, and A. Chattopadhyay, A Water-soluble Polythiophene–Au Nanoparticle Composite for pH Sensing. *Journal of Colloid and Interface Science* 316 (2007) 962-967.
- [151]U. Petra, M. Holger, S. Jens-Uwe, and S. Manfred, Polymer Brushes for Surface Tuning. *Macromolecular Rapid Communications* 30 (2009) 732-740.
- [152]H.N. Po, and N.M. Senozan, The Henderson-Hasselbalch Equation: Its History and Limitations. *Journal of Chemical Education* 78 (2001) 1499.
- [153]K. Kimura, S. Takashima, and H. Ohshima, Molecular Approach to the Surface Potential Estimate of Thiolate-Modified Gold Nanoparticles. *The Journal of Physical Chemistry B* 106 (2002) 7260-7266.
- [154]H. Sellers, A. Ulman, Y. Shnidman, and J.E. Eilers, Structure and Binding of Alkanethiolates on Gold and Silver Surfaces: Implications for Self-assembled Monolayers. *Journal of the American Chemical Society* 115 (1993) 9389-9401.
- [155]V.K. Khlestkin, J.F. Polienko, M.A. Voinov, A.I. Smirnov, and V. Chechik, Interfacial Surface Properties of Thiol-Protected Gold Nanoparticles: A Molecular Probe EPR Approach. *Langmuir* 24 (2008) 609-612.
- [156]G. Li, T. Wang, S. Bhosale, Y. Zhang, and J.-H. Fuhrhop, Completely Reversible Aggregation of Nanoparticles by Varying the pH. *Colloid and Polymer Science* 281 (2003) 1099-1103.
- [157]R. Weast, *CRC Handbook of Chemistry and Physics*, CRC Press, 1984.
- [158]M. Tenopoulou, P.-T. Doulias, and D. Galaris, Molecular Mechanisms of H<sub>2</sub>O<sub>2</sub>-Induced DNA Damage: the Action of Desferrioxamine. *Chemistry and Molecular Aspects of Drug Design and Action* (2008) 227-238.
- [159]H. Sakurai, H. Yasui, Y. Yamada, H. Nichimura, and M. Shigemoto, Detection of Reactive Oxygen Species in the Skin of Live Mice and Rats Exposed to

UVA Light: A Research Review on Chemiluminescence and Trials for UVA Protection. *Photochemical and Photobiological Science* 4 (2005) 715-720.

- [160]M. Zhou, Z. Diwu, N. Panchuk-Voloshina, and R.P. Haugland, A Stable Nonfluorescent Derivative of Resorufin for the Fluorometric Determination of Trace Hydrogen Peroxide: Applications in Detecting the Activity of Phagocyte NADPH Oxidase and Other Oxidases. *Analytical Biochemistry* 253 (1997) 162-168.
- [161]J.G. Mohanty, J.S. Jaffe, E.S. Schulman, and D.G. Raible, A Highly Sensitive Fluorescent Micro-assay of H<sub>2</sub>O<sub>2</sub> Release from Activated Human Leukocytes Using a Dihydroxyphenoxazine Derivative. *Journal of Immunological Methods* 202 (1997) 133-141.
- [162]J. Ali, Bhavna, M. Ali, and S. Baboota, Patents on Nanoparticulate Drug Delivery Systems - A Review. *Recent Patents on Drug Delivery. Formulation* 2 (2008) 83-89.
- [163]R.H. Moller, R.D. Petersen, A. Hommoss, and J. Pardeike, Nanostructured Lipid Carriers (NLC) in Cosmetic Dermal Products. *Advanced Drug Delivery Reviews* 59 (2007) 522-530.
- [164]E. Cengiz, S.A. Wissing, R.H. Muller, and Y. Yazan, Sunblocking Efficiency of Various TiO<sub>2</sub>-loaded Solid Lipid Nanoparticle Formulations<sup>1</sup>. *International Journal of Cosmetic Science* 28 (2006) 371-378.
- [165]A.M. Knaapen, T. Shi, P.J.A. Borm, and R.P.F. Schins, Soluble Metals as Well as the Insoluble Particle Fraction Are Involved in Cellular DNA Damage Induced by Particulate Matter. *Molecular and Cellular Biochemistry* 234-235 (2002) 317-326.
- [166]L. Foucaud, M.R. Wilson, D.M. Brown, and V. Stone, Measurement of Reactive Species Production by Nanoparticles Prepared in Biologically Relevant Media. *Toxicology Letters* 174 (2007) 1-9.
- [167]V.C.R.D. Nastassja Lewinski, Cytotoxicity of Nanoparticles. *Small* 4 (2008) 26-49.
- [168]T. Xia, M. Kovoichich, J. Brant, M. Hotze, J. Sempf, T. Oberley, C. Sioutas, J.I. Yeh, M.R. Wiesner, and A.E. Nel, Comparison of the Abilities of Ambient and Manufactured Nanoparticles To Induce Cellular Toxicity According to an Oxidative Stress Paradigm. *Nano Letters* 6 (2006) 1794-1807.
- [169]S.Y. Shaw, E.C. Westly, M.J. Pittet, A. Subramanian, S.L. Schreiber, and R. Weissleder, Perturbational Profiling of Nanomaterial Biologic Activity. *Proceedings of the National Academy of Sciences* 105 (2008) 7387-7392.
- [170]E.-J. Park, J. Choi, Y.-K. Park, and K. Park, Oxidative Stress Induced by Cerium Oxide Nanoparticles in Cultured BEAS-2B Cells. *Toxicology* 245 (2008) 90-100.

- [171]J.F. Reeves, S.J. Davies, N.J.F. Dodd, and A.N. Jha, Hydroxyl Radicals (OH) Are Associated with Titanium Dioxide (TiO<sub>2</sub>) Nanoparticle-induced Cytotoxicity and Oxidative DNA Damage in Fish Cells. *Mutation Research/Fundamental and Molecular Mechanisms of Mutagenesis* 640 (2008) 113-122.
- [172]S. Patil, A. Sandberg, E. Heckert, W. Self, and S. Seal, Protein Adsorption and Cellular Uptake of Cerium Oxide Nanoparticles as a Function of Zeta Potential. *Biomaterials* 28 (2007) 4600-4607.
- [173]L.K. Limbach, Y. Li, R.N. Grass, T.J. Brunner, M.A. Hintermann, M. Muller, D. Gunther, and W.J. Stark, Oxide Nanoparticle Uptake in Human Lung Fibroblasts: Effects of Particle Size, Agglomeration, and Diffusion at Low Concentrations. *Environmental Science and Technology* 39 (2005) 9370-9376.
- [174]D. Dong, D. Zheng, F.Q. Wang, X.Q. Yang, N. Wang, Y.G. Li, L.H. Guo, and J. Cheng, Quantitative Photoelectrochemical Detection of Biological Affinity Reaction: Biotin-Avidin Interaction. *Analytical Chemistry* 76 (2004) 499-501.
- [175]S. Park, Y.K. Lee, M. Jung, K.H. Kim, N. Chung, E.-K. Ahn, Y. Lim, and K.-H. Lee, Cellular Toxicity of Various Inhalable Metal Nanoparticles on Human Alveolar Epithelial Cells. *Inhalation Toxicology* 19 (2007) 59 - 65.
- [176]C.A. Cohen, J.A. Karfakis, M.D. Kurnick, and B. Rzigalinski, Cerium Oxide Nanoparticles Reduce Free Radical-Mediated Toxicity in *Drosophila melanogaster*. *FASEB J.* 22 (2008) 624.1-.
- [177]S.S. Lin, and M.D. Gurol, Catalytic Decomposition of Hydrogen Peroxide on Iron Oxide: Kinetics, Mechanism, and Implications. *Environmental Science and Technology* 32 (1998) 1417-1423.
- [178]F. Haber, and J. Weiss, The Catalytic Decomposition of Hydrogen Peroxide by Iron Salts. *Proceedings of the Royal Society of London* 147 (1934) 332-351.
- [179]D. Schubert, R. Dargusch, J. Raitano, and S.-W. Chan, Cerium and Yttrium Oxide Nanoparticles Are Neuroprotective. *Biochemical and Biophysical Research Communications* 342 (2006) 86-91.
- [180]O. Bikondoa, C.L. Pang, R. Ithnin, C.A. Muryn, H. Onishi, and G. Thornton, Direct Visualization of Defect-mediated Dissociation of Water on TiO<sub>2</sub>(110). *Nature Materials* 5 (2006) 189-192.
- [181]J.M. Peralta-Hernandez, J. Manriquez, Y. Meas-Vong, F.J. Rodriuez, T.W. Chapman, M.I. Maldonado, and L.A. Goduez, Photocatalytic Properties of Nano-structured TiO<sub>2</sub>-carbon Films Obtained by Means of Electrophoretic Deposition. *Journal of Hazardous Materials* 147 (2007) 588-593.

- [182]K. Esumi, N. Takei, and T. Yoshimura, Antioxidant-potentiality of Gold-Chitosan Nanocomposites. *Colloids and Surfaces B: Biointerfaces* 32 (2003) 117-123.
- [183]N. Yakimovich, A. Ezhevskii, D. Guseinov, L. Smirnova, T. Gracheva, and K. Klychkov, Antioxidant Properties of Gold Nanoparticles Studied by ESR Spectroscopy. *Russian Chemical Bulletin* 57 (2008) 520-523.
- [184]J. Abbot, and D.G. Brown, Kinetics of Iron-catalyzed Decomposition of Hydrogen Peroxide in Alkaline Solution. *International Journal of Chemical Kinetics* 22 (1990) 963-974.
- [185]N. Kitajima, S. Fukuzumi, and Y. Ono, Formation of Superoxide Ion During the Decomposition of Hydrogen Peroxide on Supported Metal Oxides. *Journal of Physical Chemistry* 82 (1978) 1505-1509.
- [186]X. Deng, and C. Matranga, Selective Growth of Fe<sub>2</sub>O<sub>3</sub> Nanoparticles and Islands on Au(111). *The Journal of Physical Chemistry C* 113 (2009) 11104-11109.
- [187]B. Roh, and D. Macdonald, Evidence for the Involvement of Oxygen Vacancies in the Oxygen Electrode Reaction on Passive Titanium, 207th ECS Meeting: Symposium on Electrocatalysis, Quebec, Canada, 2005.
- [188]J.-H. Kim, A. Ishihara, S. Mitsushima, N. Kamiya, and K.-I. Ota, Catalytic Activity of Titanium Oxide for Oxygen Reduction Reaction as a Non-platinum Catalyst for PEFC. *Electrochimica Acta* 52 (2007) 2492-2497.
- [189]S. Wendt, R. Schaub, J. Matthiesen, E.K. Vestergaard, E. Wahlstr, M.D. Rasmussen, P. Thostrup, L.M. Molina, E. Lasgaard, I. Stensgaard, B. Hammer, and F. Besenbacher, Oxygen Vacancies on TiO<sub>2</sub> and Their Interaction with H<sub>2</sub>O and O<sub>2</sub>: A Combined High-resolution STM and DFT Study. *Surface Science* 598 (2005) 226-245.
- [190]S. Wendt, J. Matthiesen, R. Schaub, E.K. Vestergaard, E. Laegsgaard, F. Besenbacher, and B. Hammer, Formation and Splitting of Paired Hydroxyl Groups on Reduced TiO<sub>2</sub>(110). *Physical Review Letters* 96 (2006) 066107-4.
- [191]Z. Zhang, O. Bondarchuk, J.M. White, B.D. Kay, and Z. Dohnalek, Imaging Adsorbate O-H Bond Cleavage: Methanol on TiO<sub>2</sub>(110). *Journal of Americal Chemical Society* 128 (2006) 4198-4199.
- [192]C.L. Pang, O. Bikondoa, D.S. Humphrey, A.C. Papageorgiou, G. Cabailh, R. Ithnin, Q. Chen, C.A. Muryn, H. Onishi, and G. Thornton, Tailored TiO<sub>2</sub>(110) Surfaces and Their Reactivity. *Nanotechnology* 17 (2006) 5397-5405.
- [193]O.V. Krylov, and B.R. Shub, *Nonequilibrium Porcesses in Catalysis*, CRC, Boca Raton, FL, 1994.